X-ray optics in new instruments for astro- and astroparticle physics

Jakobsen, Anders Clemen

Publication date:
2015

Document Version
Publisher's PDF, also known as Version of record

X-ray optics in new instruments for astro- and astroparticle physics

PhD thesis of

Anders Clemen Jakobsen

Kongens Lyngby, 2015

DTU Space
National Space Institute

DTU Space
National Space Institute

Technical University of Denmark
Building 327, DK-2800 Kongens Lyngby, Denmark
Phone +45 45253351, Fax +45 45882673
www.space.dtu.dk

Compiled: marts 15, 2016 at 10:53
ISBN 978-87-91694-28-8

'Progress isn't made by early risers.
It's made by lazy men
trying to find easier ways to do something.'
- *R.A. Heinlein*

Summary

Discovering new phenomena in physics require ever larger and more advanced instruments in order to detect either fundamental particles or energetic events in the universe. This thesis describes the work done on three separate X-ray telescopes, one for astrophysics and two for astroparticle physics; all of which makes use of grazing incidence reflecting X-ray optics.

Reflective coatings using various materials on Silicon Pore Optic (SPO) substrates were investigated for the European Athena large X-ray telescope mission. Ir/B_4C single bilayer and multilayer coatings were characterised and qualified for long term stability and reflectivity performance. A Cr sublayer under an Ir/B_4C coating was seen to mitigate the film stress; additionally, Ir coatings were found to show a smoothening effect when deposited onto a rough Cr surface. The coating production upscaling to 210,000 SPO substrates coated over a two year period is discussed and a multi chamber solution is described.

An X-ray telescope for the CAST helioscope at CERN was designed, optimised, produced and installed in order to improve the sensitivity of the helioscope. The installed telescope focuses X-rays, converted from axions through the Primakoff effect, into a detector area 400 times smaller than before. Measurements using an X-ray source shows the telescope behaving as calculated through ray tracing.

A successor to the CAST helioscope named the International AXion Observatory (IAXO) is in the definition phase and X-ray telescopes to the much larger instrument was designed. Software was developed to calculate the optimal focal length based on estimated telescope figure error and angular size of the sun.

A new software solution for the coating facility at DTU Space was developed using the SPEC software package, improving the flexibility and capability of the setup. The instruments connected to the coating chamber were all implemented. Coatings for the CAST X-ray telescope and Athena coating qualifications were done using the new software.

Resumé

Til at opdage nye fænomener i fysikken kræves evigt større og mere avancerede instrumenter for at detektere enten fundamentale partikler eller energirige begivenheder i universet. Denne afhandling beskriver arbejdet på tre separate Röntgenteleskop, én til astrofysik og to til astropartikelfysik. Alle gør de brug af lavvinkelreflektioner på Röntgenspejle med specielle belægninger.

Reflekterende belægninger der gør brug af forskellige materialekombinationer på Silicon Pore Optic (SPO) substrater blev undersøgt til den store europæiske Athena Röntgenteleskopsmission. Belægninger med Ir/B_4C enkeltlag eller multilag blev karakteriseret og kvalificeret for stabilitet over længere tid samt reflektionseffektivitet. Et Cr underlag under Ir/B_4C belægninger viste sig at begrænse tyndfilmsstress og derudover viste Ir belægningen at have en glattende effekt når deponeret ovenpå en ru Cr overflade. Opskalering af produktionen af reflekterende belægninger på 210,000 SPO substrater over en to års periode er diskuteret og en multikammersløsning er beskrevet.

Et Röntgenteleskop til CAST helioskopet på CERN blev designet, optimiseret, produceret og installeret for at forbedre følsomheden af helioskopet. Det installerede teleskop fokuserer Röntgenstråler, konverteret fra axioner ved Primakoff-effekten, i et detektorareal 400 gange mindre end før. Målinger med en Röntgenkilde viste at teleskopet opfører sig som udregnet med raytracing.

En efterfølger til CAST helioskopet kaldet International AXion Observatory (IAXO) er i defineringsfasen og Röntgenteleskoper til det meget større instrument blev designet. Software blev udviklet til at udregne den optimale fokallænge baseret på den estimerede figurfejl i teleskopet og den angulære størrelse på solen.

En ny softwareløsning til coatingfaciliterne på DTU Space blev udviklet ved brug af SPEC software pakken for at forbedre fleksibiliteten og mulighederne af opstillingen. Instrumenterne forbundet coatingkammeret blev alle implementeret. Multilagsbelægninger til CAST Röntgenteleskopet samt Athena kvalificeringerne blev foretaget ved brug af det nye software.

Preface

This thesis was prepared at DTU Space, the Technical University of Denmark in partial fulfilment of the requirements for acquiring the Ph.D. degree.

The thesis deals with characterising and qualifying reflective X-ray coatings for the European Athena large X-ray telescope; the design, optimisation, production and installation of an X-ray telescope on the CAST helioscope at CERN; and the design and optimisation of X-ray telescopes for the International AXion Observatory.

The thesis consists of four chapters describing each of the projects worked on in the period 2011–2014. In the appendix is found three SPIE proceeding papers and a journal paper that describes the Athena, CAST and IAXO projects.

Chapter 2 describes the coating facility at DTU Space and the work done to replace the control software with a more flexible and capable solution.

Lyngby, October 2015

Anders Clemen Jakobsen

Acknowledgements

First of all I would like to thank my wife and family for their patience and support during my PhD work. I promise to return to the living now.

A lot of people have been extremely helpful during my PhD work. First of all I would like to thank my office mate and colleague Desiree D. M. Ferreira for great project management, emotional support and friendship during the past four years.

Many problems in the lab could not have been solved without the help from Joan Momberg, Michael H. Avngaard and Kim E. Madsen from the electronics department at DTU Space. Joan has been an expert repository of knowledge and experience in the coating facility.

I am very thankful for the support from Birte E. Hede and Lene Bettenhaus from DTU Space for whenever I needed administrative help.

A great thanks goes to Michael J. Pivovaroff from Lawrence Livermore Natl. Lab. for giving me the opportunity to have my external stay there and inviting our group into the CAST collaboration. The CAST XRT would not have happened without him and the people from his group, in particular Todd Decker, Jaime Ruz and Julia Vogel. Also thanks to Regina Soufli and Chris Walton for nice discussions.

I would also like to thank Igor Irastorza, Juanan Garcia, Javier G. Garza and Juan Castel from University de Saragoza for their great support in making the CAST telescope installation happen and designing detectors and X-ray source.

Also a big thanks to Igor and Mike for coming to Denmark and talking at the small axion symposium I arranged.

A good number of measurements were done at the BESSY II synchrotron at PTB in Berlin. I would like to thank Stefanie Marggraf, Levent Cibik and Michael Krumrey for the work and patience they put into the measurement campaigns.

New people in the X-ray optics group at DTU Space will be taking over my responsibilities in the coating facility and I would like to thank Sonny Masahi and David Girou for doing this and at the same time wish them good luck. David Girou also performed the ISO qualification tests for the Athena coatings, which has been a huge help.

Lastly, I would like to thank my supervisor Finn E. Christensen for letting me pursue all the

projects I wanted. The PhD work has been exciting and challenging, primarily as a result of Finn's long experience in the field which constantly opened up to new opportunities.

Papers included in the thesis

[A] Anders C. Jakobsen, Desiree Della Monica Ferreira, Finn E. Christensen, Brian Shortt, Max Collon, Marcelo D. Ackermann;
Preliminary coating design and coating developments for Athena. *Proc. SPIE, Optics for EUV, X-Ray and Gamma-Ray Astronomy V*, 8147 (2011);

[B] Desiree D. M. Ferreira, Anders C. Jakobsen, Finn E. Christensen, Brian J. Shortt, Michael Krumrey, Jørgen Garnæs, Ronni B. Simonsen;
Development and characterization of coatings on silicon pore optics substrates for the Athena Mission. *Proc. SPIE, Space Telescopes and Instrumentation 2012: Ultraviolet to Gamma Ray*, 8443 (2012);

[C] Anders C. Jakobsen, Michael J. Pivovaroff, Finn E. Christensen;
X-ray optics for axion helioscopes. *Proc. SPIE, Optics for EUV, X-Ray and Gamma-Ray Astronomy VI*, 8861 (2013)

[D] E Armengaud, F T Avignone, M Betz, P Brax, P Brun, G Cantatore, J M Carmona, G P Carosi, F Caspers, S Caspi, S A Cetin, D Chelouche, F E Christensen, A Dael, T Dafni, M Davenport, A V Derbin, K Desch, A Diago, B Döbrich, I Dratchnev, A Dudarev, C Eleftheriadis, G Fanourakis, E Ferrer-Ribas, J Galán, J A García, J G Garza, T Geralip, B Gimeno, I Giomataris, S Gninenko, H Gómez, D González-Díaz, E Guendelman, C J Hailey, T Hiramatsu, D H H Hoffmann, D Horns, F J Iguaz, I G Irastorza, J Isern, K Imai, A C Jakobsen, J Jaeckel, K Jakovčića, J Kaminski, M Kawasaki, M Karuza, M Krčmara, K Kousouris, C Krieger, B Lakića, O Limousin, A Lindner, A Liolios, G Luzón, S Matsuki, V N Muratova, C Nones, I Ortega, T Papaevangelou, M J Pivovaroff, G Raffelt, J Redondo, A Ringwald, S Russenschuck, J Ruz, K Saikawa, I Savvidis, T Sekiguchi, Y K Semertzidis, I Shilon, P Sikivie, H Silva, H ten Kate, A Tomas, S Troitsky, T Vafeiadis, K van Bibbera, P Vedrine, J A Villar, J K Vogel, L Walckiers, A Weltman, W Wester, S C Yildiz and K Zioutas.
Conceptual design of the International Axion Observatory (IAXO). *J. Inst.* 9 (2014).

Additional publications co-authored during the PhD study

- Nicolai F. Brejnholt, Regina Soufli, Marie-Anne Descalle, Mónica Fernández-Perea, Finn E. Christensen, Anders C. Jakobsen, Veijo Honkimäki, and Michael J. Pivovaroff.

Demonstration of multilayer reflective optics at photon energies above 0.6 mev. *Opt. Express*, 22(13):15364–15369, Jun 2014.

- Marcos Bavdaz, Eric Wille, Kotska Wallace, Brian Shortt, Sebastiaan Fransen, Maximilien Collon, Marcelo Ackermann, Giuseppe Vacanti, Ramses Guenther, Jeroen Haneveld, Mark Olde Riekerink, Coen van Baren, Dirk Kampf, Karl-Heinz Zuknik, Finn Christensen, Desiree Della Monica Ferreira, Anders Clemen Jakobsen, Michael Krumrey, Peter Müller, Vadim Burwitz, Giovanni Pareschi, and Mauro Ghigo. Preparing the optics technology to observe the hot universe. *Proc. SPIE*, 9144:91442F–91442F–8, 2014.

- R. Willingale, G. Pareschi, F. Christensen, J.-W. den Herder, D. Ferreira, A. Jakobsen, M. Ackermann, M. Collon, and M. Bavdaz. Science requirements and optimization of the silicon pore optics design for the Athena mirror. *Proc. SPIE*, 9144:91442E–91442E–9, 2014.

- I G Irastorza, F T Avignone, G Cantatore, J M Carmona, S Caspi, S A Cetin, F. E. Christensen, A Dael, T Dafni, M Davenport, A V Derbin, K Desch, A Diago, B Döbrich, A Dudarev, C Eleftheriadis, G Fanourakis, E Ferrer-Ribas, J Galan, J A Garcia, J G Garza, T Geralis, B Gimeno, I Giomataris, S Gninenko, H Gomez, E Guendelman, C J Hailey, T Hiramatsu, D H H Hoffmann, D Horns, F J Iguaz, J Isern, A. C. Jakobsen, J Jaeckel, K Jakovcic, J Kaminski, M Kawasaki, M Krcmar, C Krieger, B Lakic, A Lindner, A Liolios, G Luzon, I Ortega, T Papaevangelou, M J Pivovaroff, G Raffelt, J Redondo, A Ringwald, S Russenschuck, J Ruz, K Saikawa, I Savvidis, T Sekiguchi, I Shilon, P Sikivie, H Silva, H Ten Kate, A Tomas, S Troitsky, T Vafeiadis, K van Bibber, P Vedrine, J A Villar, J K Vogel, L Walckiers, W Wester, S C Yildiz, and K Zioutas. Future axion searches with the International Axion Observatory (IAXO). *Journal of Physics: Conference Series*, 460(1):012002, October 2013.

- Marcos Bavdaz, Eric Wille, Kotska Wallace, Brian Shortt, Sebastiaan Fransen, Nicola Rando, Maximilien Collon, Marcelo Ackermann, Giuseppe Vacanti, Ramses Günther, Jeroen Haneveld, Mark Olde Riekerink, Arenda Koelewijn, Coen van Baren, Dirk Kampf, Karl-Heintz Zuknik, Arnd Reutlinger, Finn Christensen, Desiree Della Monica Ferreira, Anders C Jakobsen, Michael Krumrey, Peter Müller, Vadim Burwitz, Giovanni Pareschi, Mauro Ghigo, Marta Civitani, Laura Proserpio, Daniele Spiga, Stefano Basso, Bianca Salmaso, Daniele Gallieni, Matteo Tintori, Pierluigi Fumi, Francesco Martelli, Giancarlo Parodi, Ivan Ferrario, and Ian Povey. X-ray optics developments at ESA. In *SPIE Optical Engineering + Applications*, pages 88610L–88610L–12. International Society for Optics and Photonics, September 2013.

- Monica Fernandez-Perea, Marie-Anne Descalle, Regina Soufli, Klaus P Ziock, Jennifer Alameda, Sherry L Baker, Tom J McCarville, Veijo Honkimäki, Eric Ziegler, Anders C Jakobsen, Finn E Christensen, and Michael J Pivovaroff. Physics of Reflective Optics for the Soft Gamma-Ray Photon Energy Range. *Physical Review Letters*, 111(2):027404, July 2013.

- Desiree Della Monica Ferreira, Finn E Christensen, Michael J Pivovaroff, Nicolai Brejnholt, Monica Fernandez-Perea, Niels Jørgen S Westergaard, Anders C Jakobsen,

Marie-Anne Descalle, Regina Soufli, and Julia K Vogel. Hard x-ray/soft gamma ray telescope designs for future astrophysics missions. In *SPIE Optical Engineering+ Applications*, pages 886116–886116. International Society for Optics and Photonics, 2013.

- Desiree DM Ferreira, Finn E Christensen, Anders C Jakobsen, Niels J Westergaard, and Brian Shortt. Coating optimization for the Athena+ mission. In *SPIE Optical Engineering+ Applications*, pages 886112–886112. International Society for Optics and Photonics, 2013.

- Monica Fernandez-Perea, Mike J Pivovaroff, Regina Soufli, Jennifer Alameda, Paul Mirkarimi, Marie-Anne Descalle, Sherry L Baker, Tom McCarville, Klaus Ziock, Donald Hornback, Suzanne Romaine, Ric Bruni, Zhong Zhong, Veijo Honkimäki, Eric Ziegler, Finn E Christensen, and Anders C Jakobsen. Ultra-short-period WC/SiC multilayer coatings for x-ray applications. *Nuclear Instruments & Methods In Physics Research Section A-Accelerators Spectrometers Detectors And Associated Equipment*, October 2012.

- Desiree DM Ferreira, Finn E Christensen, Anders C Jakobsen, Niels J Westergaard, and Brian Shortt. Athena optimized coating design. In *SPIE Astronomical Telescopes+ Instrumentation*, pages 84435L–84435L. International Society for Optics and Photonics, 2012.

- Finn E Christensen, Anders C Jakobsen, Nicolai F Brejnholt, Kristin K Madsen, Allan Hornstrup, Niels J Westergaard, Joan Momberg, Jason Koglin, Anne M Fabricant, Marcela Stern, William W Craig, Michael J Pivovaroff, and David Windt. Coatings for the NuSTAR mission. In *SPIE Optical Engineering+ Applications*, pages 81470U–81470U–19, September 2011.

- Jason E Koglin, Hongjun An, Nicolas Barriere, Nicolai F Brejnholt, Finn E Christensen, William W Craig, Charles J Hailey, Anders Clemen Jakobsen, Kristin K Madsen, Kaya Mori, Melania Nynka, Monica Fernandez-Perea, Michael J Pivovaroff, Andrew Ptak, Clio Sleator, Doug Thornhill, Julia K Vogel, Daniel R Wik, and William W Zhang. First results from the ground calibration of the NuSTAR flight optics. *SPIE Optical Engineering + Applications*, 8147:81470J–81470J–16, September 2011.

- Nicolai Brejnholt, Finn Erland Christensen, Charles J Hailey, Nicolas M Barrière, William W Craig, Brian Grefenstette, Jason Koglin, Kristin Kruse Madsen, Julia K Vogel, Hongjun An, Kenneth Blaedel, Josh Brown, Todd Decker, Zeshan Haider, Anders Clemen Jakobsen, Carsten P Cooper-Jensen, Kaya Mori, Melania Nynka, Michael J Pivovaroff, Clio Sleator, Dennis Stefanik, Marcela Stern, Gordon Tajiri, Douglas Thornhill, and Jeremy S Cushman. The Rainwater Memorial Calibration Facility for X-Ray Optics. *X-Ray Optics and Instrumentation*, 2011:285079, 2011.

- Nicolai Brejnholt, Finn Erland Christensen, Anders Clemen Jakobsen, Charles J Hailey, Jason E Koglin, Kenneth L Blaedel, Marcela Stern, Doug Thornhill, Clio Sleator, Shuo Zhang, William W Craig, Kristin K Madsen, Todd Decker, Michael J Pivovaroff, and Julia K Vogel. NuSTAR ground calibration: The Rainwater Memorial Calibration Facility (RaMCaF). In *SPIE Optical Engineering + Applications*, pages 81470I–9, 2011.

- Maximilien J Collon, Ramses Günther, Marcelo Ackermann, Rakesh Partapsing, Giuseppe Vacanti, Marco W Beijersbergen, Marcos Bavdaz, Kotska Wallace, Erik Wille, Mark Olde Riekerink, Jeroen Haneveld, Arenda Koelewijn, Coen van Baren, Peter Müller, Michael Krumrey, Michael Freyberg, Anders Clemen Jakobsen, and Finn Erland Christensen. Design, fabrication, and characterization of silicon pore optics for athena/IXO. In *SPIE Optical Engineering + Applications*, pages 81470D–1, 2011.

Contents

Chapter 1

Introduction

For the past 50 years, the quest for discovering the cosmos has led to a large array of advances in optics based technology. To overcome the challenges of imaging objects far away and at wavelengths way beyond the capabilities of the human eye, scientists and engineers have come up with ingenious solutions. Specifically, when it comes to imaging and detection in the X-ray range (photon energies of ∼0.1-500 keV), whole new obstacles had to be overcome.

The first problem was the inability of X-rays to penetrate Earth's atmosphere, which necessitated detectors to be placed on balloons, sounding rockets or in orbit around earth. That gave rise to a drive for weight saving, miniaturisation and power conservation.

The next problem that became apparent was the inability of X-rays to be reflected in a mirror in contrast to ground based or orbiting optical telescopes such as Hubble. The high energy of X-rays means that the refractory index of a material become less than unity, so instead of being reflected, the photons are absorbed. However, there is a workaround: The X-ray photons can be reflected at very small grazing angles, e.g. a 10 keV photon can be reflected at up to ∼0.3 degrees from a gold surface with almost 100% intensity. Luckily, the gold is not strictly necessary as any high electron density material will do (anything with a high Z number in the periodic table). Then how can we make an optic that reflects at such low grazing angles, but still has a big collecting area, and preferably also focuses like a parabolic mirror? The answer came from nested shells of concentric mirrors all angled[1] to reflect incoming X-rays to the same spot. Using two sets of mirrors, the first with a parabolic shape and the second with a hyperbolic shape will make it possible to fit the optic in a spacecraft that will fit on a rocket. The design is called a Wolter I type optic[1, 2] (named after the inventor) and fulfils the requirements for a grazing angle focusing telescope.

Then a new problem comes to light: As the energy of the X-ray photon increases, the grazing angle at which we see reflection from a gold surface decreases dramatically. That leaves us with two options, either increase the length of the optic with extendable masts (costly and technically difficult), or somehow improve the reflecting surface. Looking at

[1] It is important to consider that in astrophysical observations, the photons coming from a distant object are described as completely collimated or in other words: Their trajectories are parallel so all arrive at the optic with the exact same normal angle.

the properties of X-rays it was seen that it is possible for an X-ray photon to reflect from the lattice plane of a crystal. Specifically, the photon saw the change in electron density from between the lattice planes to a lattice plane like a surface.[2] Additionally, the photons achieve constructive interference at certain angles related to the photon wavelength and lattice spacing known as the Bragg condition[3]. So how to take advantage of those X-ray properties? Using lattices means using perfect crystals and shaping them into a Wolter I type optic, both of which creates all new problems[4]. Instead the attention was turned to thin film coatings. Advances in technology made it possible to deposit extremely thin and very uniform coatings with a wide variety of materials. By applying a multilayer coating of interchanging materials with low electron density and high electron density, a pseudo crystal can be created. The thickness of each layer can be determined precisely, so in accordance with the Bragg condition the thickness can be designed to reflect at a given angle and photon energy. The constructive interference of the Bragg condition is however a drawback when it comes to astrophysical observations, as only a small bandwidth of photons will be reflected. To overcome that problem, a multilayer with hundreds of layers, and film thicknesses that varied from top to bottom was developed. These coatings are called graded-d multilayers and were used for the first time in an astrophysical observatory in the balloon mission HEFT[6, 7, 8]. The successor of HEFT was NuSTAR[9, 10, 11] that also used power-law graded multilayer coatings on slumped glass substrates[12, 13] and was launched in 2012. NuSTAR has from 2012 to 2014 been the NASA mission with the second most published papers from the observations. A short description of NuSTAR can be found in section 1.1.2.

In this thesis is described work done from 2011 to 2014 on coating developments for the European Athena mission, the design, production, and installation of an X-ray telescope for the CAST experiment at CERN, and the design of an X-ray telescope for IAXO, the proposed successor to CAST. All of these instruments are Wolter I style X-ray telescopes that function at grazing angles and in an energy band in the very low end compared to NuSTAR, right in the region where there is only a limited benefit from using multilayers compared to single or double layer coatings.

Chapter 2 is a description of the coating facility and X-ray measurement setup at DTU Space.

For the coating developments for Athena found in chapter 3, the main goal was to find coatings that are stable and well-performing. Coatings that will behave well even after being launched by a rocket and drifting around a Lagrange point for 10+ years. At the same time the coatings should be able to reflect well enough to give Athena the largest effective area of any X-ray telescope. A new optics technology was developed by ESA leveraged by advances in the semiconductor industry, but require specific processes that would ruin pure carbon coatings, an element used in the NuSTAR coatings. The final problem was to find a way to coat the 210,000 mirrors required for the mission, in the 2

[2]The reverse argument is more correct. Photons reacting to a surface are just photons reacting to a change in electron density.

[3]$n\lambda = 2d\sin(\theta)$ with λ being the wavelength, d the lattice spacing and θ the angle

[4]Using perfect crystals for X-ray and Gamma-ray instrumentation are being investigated and are called Laue lenses[3, 4, 5].

years allocated by ESA for mirror production and coating.

The development of an X-ray optic for the CERN Axion Solar Telescope (CAST) helioscope can be found described in chapter 4. The CAST helioscope looks for the hypothetical axion particle, a possible solution to the CP violation problem in particle physics and a candidate for Dark Matter. Using a strong magnetic field to convert axion particles to X-ray photons, CAST is the most comprehensive experiment for detecting axions to date. In order to improve the sensitivity of the helioscope, an X-ray telescope was needed to focus photons converted from axions into a small detector.

A proposed successor to the CAST experiment is the International AXion Observatory (IAXO), which is described in chapter 5, the paper *X-ray optics for axion helioscopes* in appendix C, and the paper *Conceptual design of the International Axion Observatory (IAXO)* of which a relevant part is found in appendix D. IAXO is based on the same principle of the CAST helioscope, a superconducting magnet applies a magnetic field to convert axions into X-ray photons. The photons are collected by X-ray telescopes and focused into detectors. Numerous improvements of IAXO over CAST makes the sensitivity more than five orders of magnitude better, making it possible to reach the axion-photon coupling range at which most axion models predict the hypothetical particle will be found.

1.1 Coatings for X-ray telescopes

To focus X-rays in space- or balloon-based telescopes, an array of mirrors with specific coatings is required. When focusing photons in the UV spectrum and longer wavelengths up beyond radio waves, the mirror can be a parabola since the refractive index deviates considerably from unity at longer wavelengths. In the X-ray case however, the refractive index deviation from unity is in the order of -10^{-5}, which means that from ambient (vacuum/air, $n = 1$) to matter, the direction of the photon is changed very little. In a single lens, the focal length is in the range of 100 m. Using a regular lens to focus would require a material with as high a deviation from unity as possible, which means denser materials that results in more absorption. So, normal incidence parabolic focusing and regular refractive focusing are not feasible solutions for focusing X-rays. Instead, grazing incidence reflection is used, since below a very low critical angle θ_c, X-rays will experience total external reflection on a surface[14]. θ_c is connected to the density of the surface material by

$$\theta_c = \sqrt{2\delta} \tag{1.1}$$

with

$$\delta = \frac{2\pi\rho_A f^0(0) r_0}{k^2} \tag{1.2}$$

where $\rho_A f^0(0) = \rho$ is the electron density of the material. The critical angle can therefore be changed by using a heavier material as a mirror. Recent X-ray missions such as Chandra

from NASA and XMM from ESA utilizes mirrors coated with gold to increase θ_c and decrease the focal length.

The mirrors coated with a single high density material have the drawback that they cannot effectively provide reflectivity for X-ray photons with energies outside the 0.1 to 5 keV range. When the X-ray photon energy increases, the critical angle of the material decreases, the result for a iridium film can be seen in figure 1.1 at a reflectivity angle of 0.5°. The angle of 0.5° is the reflectivity angle for a mirror in a mirror array distanced ∼35 cm from the focal plane and with a focal length of 10 m.

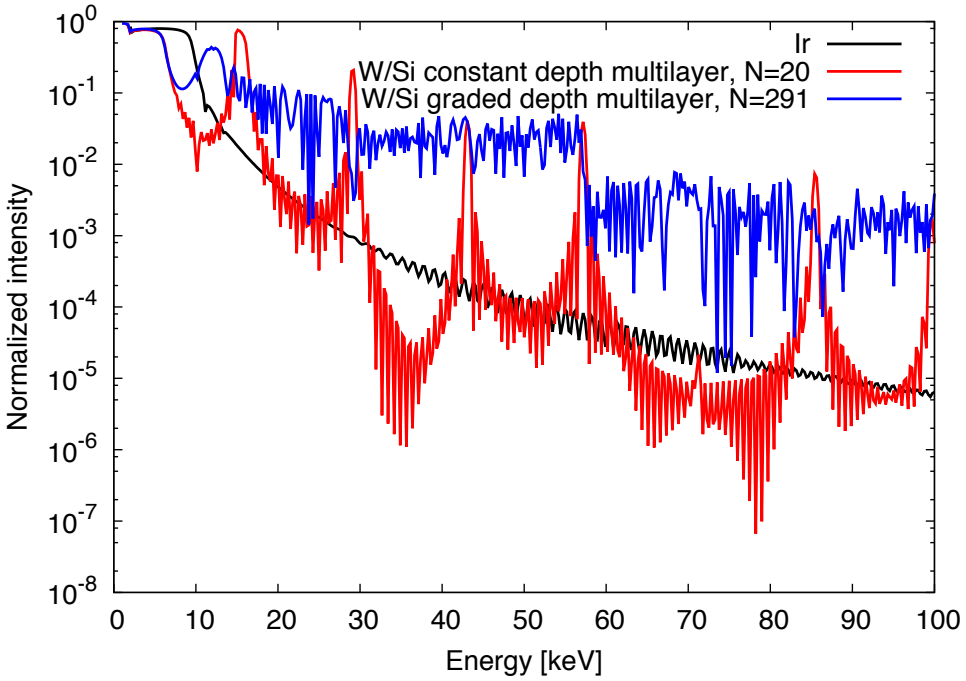

Figure 1.1: Simulations of X-ray reflectivity from an iridium singlelayer, from a W/Si constant depth multilayer and from a W/Si graded depth multilayer as a function of energy and at a grazing incidence angle of 0.5°. The Ir singlelayer loses reflectance steadily as energy increases. The constant depth multilayer gives much higher reflectivity, but only at energies where the Bragg condition is fulfilled. The depth graded multilayer reflectivity is consistently higher than the singlelayer by at least an order of magnitude from 10 keV and up.

To focus higher energies, it is necessary to use multilayers with bilayers of two different materials. These improve the performance significantly at higher energies as can be seen in figure 1.1 (red line). The two materials have to be one of high electron density (high Z) and one of low electron density (low Z), since it is the interfaces between two materials with high difference in refractive index that reflects the X-ray photons. The mathematical description of X-ray reflectivity from a thin film is described in appendix E. The basic parameters that define a multilayer is:

- N, the number of bilayers in the multilayer
- d, the thickness of the bilayers, also called the d-spacing
- Γ, the thickness ratio of low Z versus high Z materials

The multilayer can have a constant d-spacing through the entire stack and will then exhibit Bragg reflections as the interfaces will act like periodic lattice planes in a crystal. The Bragg condition ensures that only a certain energy can be reflected at a certain angle because of constructive interference. Other energies will not experience constructive interference, so the reflected intensity becomes negligible for those energies. When focusing non-monochromatic X-ray photons, but rather photons with a range of energies, it is necessary to have a mirror with a smooth energy response. To achieve that, the d-spacing can be changed through the stack according to a linear grading or a power-law grading[15], $d_i = a/(b+i)^c$, where d_i is the d-spacing for the i'th layer, see figure 1.2. The constants are determined for values of c, d_{min}, d_{max}. The resulting so-called *depth graded* multilayer have a smoother response curve, so are more suitable for astronomical telescopes. The reflectivity curve of a depth graded multilayer can be seen in figure 1.1 (blue line).

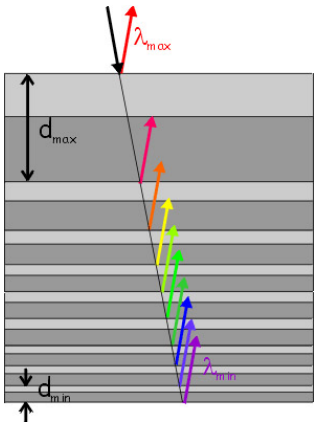

Figure 1.2: Diagram describing the reflections from a graded multilayer. Each bilayer reflects at a specific energy, with thin bilayers reflecting high energy photons and thick bilayers reflecting low energy photons. The absorption is also minimised as the high energy photons can easier penetrate the stack.

The material chosen as low Z and high Z materials will perform best if the difference in electron density is as large as possible. Another factor to consider is the ability of the combination of two materials in a multilayer (e.g. W and Si) to achieve low roughness in the interfaces between each layer. The interface between two layers can be described by an interface profile developed by Stearns et al[16]. The profile width is $\sigma_{\text{rms}} = (\sigma_r^2/2 + \sigma_f^2/2)^{1/2}$, where σ_r is the roughness and σ_f is the diffuseness of the two materials in the interface. A general rule of thumb is to keep $\sigma_{rms} \leq d/6$, with d being the thickness of a single bilayer. That means that a bilayer which is 3 nm thick can only have an average roughness of 0.5 nm, which is only the height of a few atomic monolayers. A roughness higher than that will cause loss of definition in the multilayer resulting in less defined Bragg peaks given by loss of reflectivity at the interfaces.

1.1.1 Effective area

An important benchmark for telescopes of all parts of the spectrum (optical, UV, X-ray, etc.) is the effective area. It is a metric of the telescope's collecting area at each wavelength

or energy. By taking the reflecting area of a telescope and multiplying it by the normalized reflectivity spectrum, the result is the effective area. However, the process becomes a little more complicated considering that the reflectivity is dependent on incident angle on the reflecting surface. In an X-ray telescope consisting of concentric mirror shells, each mirror shell will reflect incoming photons at a different angle that each result in a certain reflectivity spectrum. Also to consider is the fact that Wolter I telescopes requires a double reflection, so the reflectivity spectrum should be squared. The effective area of a single mirror shell with double reflection in a Wolter I optic is

$$A_{\text{eff}} = R^2(\text{E})A \tag{1.3}$$

where R is the reflectivity of a photon on the surface at the angle specified by the focal length and mirror shell distance to the optic focal axis. A is the cross-sectional area of the first mirror as viewed from the front of the optic.

In an example of five mirror shells, the effective area of each shell is added up, resulting in the effective area of the full telescope

$$A_{\text{eff}} \;=\; \sum_{i=0}^{n} A_{\text{eff,i}} \tag{1.4}$$

In order to get as sensitive a telescope as possible, and in order to catch the relatively sparse amount of soft X-ray photons from far away sources, an effective area as large as possible is needed. For this reason it is important to design and optimize the telescope optics so that this is accomplished. After the design and geometry of the optics module is decided, it is lastly the reflective surface of the individual mirrors which should be optimised in order to achieve the best effective area. This means that both the material combinations, the thickness of the coating, the number of bilayers, and the use of different recipes throughout the optics design will have an influence of the telescope throughput.

In this thesis I will investigate different combinations of the above and present the results with the purpose of identifying the best possible coating that will help us achieve the described objectives.

1.1.2 NuSTAR

This thesis has a number of references to the NuSTAR mission, so a short overview is given here.

The NuSTAR telescope was the first mission to carry a hard X-ray (5-80 keV) focusing telescope to orbit, and the first in-orbit X-ray telescope to use graded-d multilayer coatings.

It is a NASA mission made in collaboration between mainly Caltech, Columbia University, Lawrence Livermore National Lab., and DTU Space and was launched in 2012. Using an extendable mast (see figure 1.3), the focal length reaches 10 m when deployed in orbit. It carries two Wolter I type telescopes that are made by rectangular pieces of 0.21 mm thick glass, slumped to the curvature of each radius in the telescope[17, 18] (see figure 1.4). The glass has a 0.4–0.5 nm r.m.s. roughness.

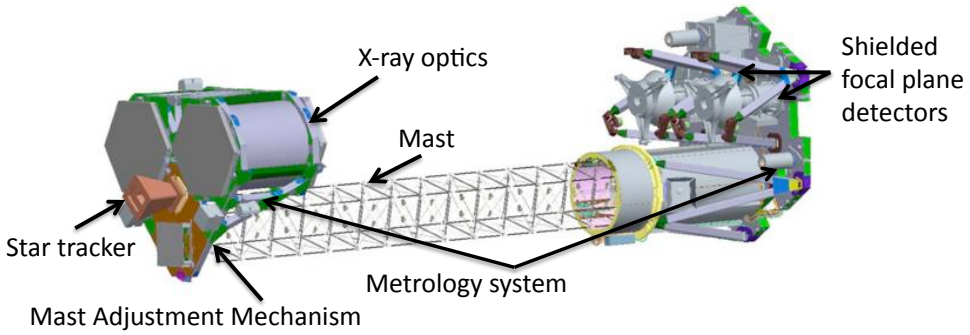

Figure 1.3: Illustration of the NuSTAR telescope with the extendable mast partially collapsed. The two optics are placed on the left side and is in the shown configuration with covers to protect the optic before deployment. Each optic focuses X-rays into the two focal plane detectors on the right side. From [10].

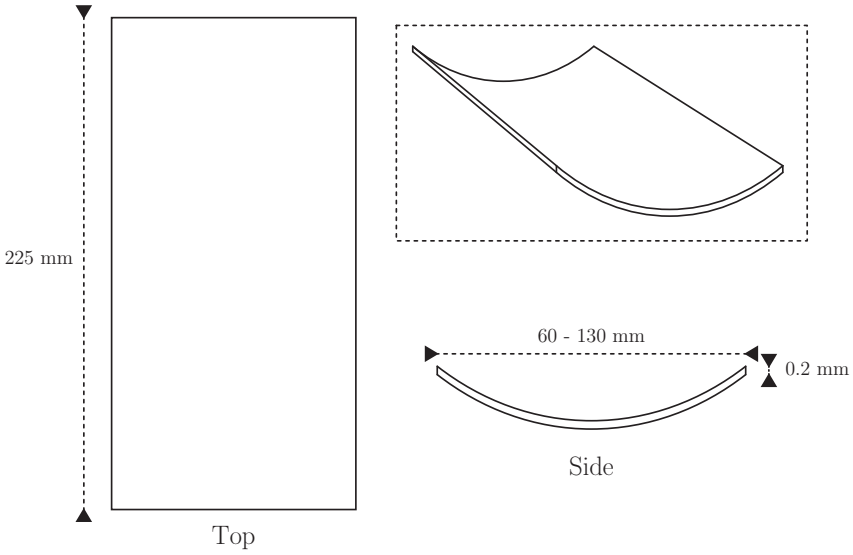

Figure 1.4: Illustration of a NuSTAR glass substrate. All pieces are 225 mm long and 0.2 mm thick, but varies in width from ∼60–∼140 mm.

Each telescope consists of 133 concentric mirror shells of glass, with each glass substrate being 225 mm long. Two stacks of 133 shell layers fit together to make the first and second reflection of the Wolter I principle. The innermost and outermost shells have radii of 54.4 mm and 191 mm, respectively, making the total diameter of each telescope ∼400 mm. Glass substrates were mounted using graphite spacers that were machined to ∼2.5 μm precision. An illustration of an assembled optic can be seen in figure 1.5.

All glass substrates for NuSTAR were coated at DTU Space using multilayer material

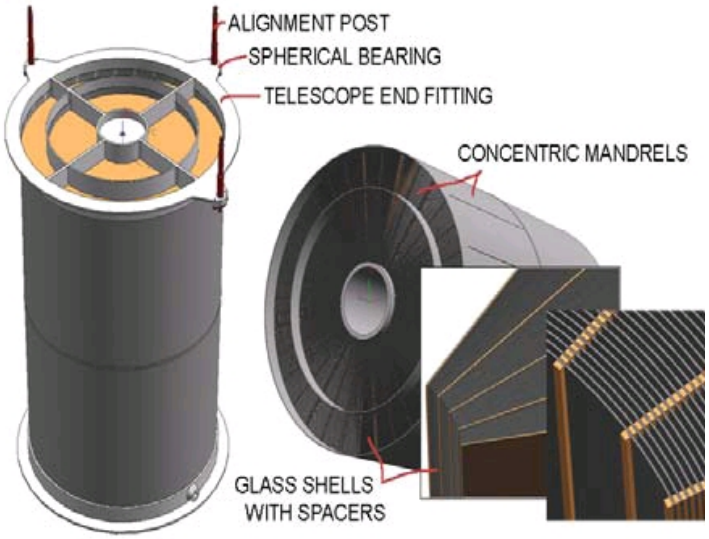

Figure 1.5: Illustration of an assembled NuSTAR optic. A central mandrel made from SiC is used as a base on which the firat glass layer is attached to graphite spacers with epoxy. Each subsequent layer is attached using graphite spacers, resulting in a rigid construction. From [6]

combinations of either W/Si or Pt/C. Multilayers of W/Si were 291 bilayers and multilayers of Pt/C were 145 bilayers. The multilayers were graded according to a power-law[19].

Chapter 2

DTU Space coating facility

The multilayer coating facility consists of a vacuum chamber placed in the laboratory known as the Multilab. It started out as a vapor deposition chamber for the SODART mission[20, 21]. Capable of vaporising a gold wire with a W rod in the center of the chamber, it would deposit a layer of gold on any mirror facing the center. The chamber was later upgraded with magnetron cathodes, each with independent shutters.

The currently used cathodes are attached to powerful DC power supplies that can deposit films atom-by-atom instead of the larger gold particles that would come from vaporisation. The upgrade made it possible to coat multilayers with d-spacings thinner than 3 nm and eventually became the coating method used for the NuSTAR mission.

The entire lab was moved from Rockefeller Institute near Rigshospitalet in Copenhagen during the summer of 2012. It was up and running again around the summer of 2013 in the newly constructed building 328, the new home for DTU Space on DTU campus. In the new location, the lab is 50% larger, has a double airlock (earlier just a single airlock), laminar airflow from ceiling mounted HEPA filters and various other improvements. The result is a considerably cleaner facility, which is important to avoid contaminants on optical substrates.

The vacuum chamber is the dominant piece of the laboratory and most of the computers, electronics and cooling in the lab is in some way connected to the chamber. Apart from the chamber, the lab consists of a downflow module, two fume hoods, a profilometer, a large clean room oven and various tables and cupboards (see figure 2.1). Next to the lab is the Multilab Auxiliary Room, which houses the cooling heat exchangers and pumps, the rotary vane roughing pump, DC power supplies, and a large part of the extra storage needed for the lab. Additionally, there is a room in the basement that houses a ceramic oven that has a built in vacuum chamber, the room also serves to store hundreds of spare pieces of NuSTAR optic glass.

Figure 2.1: Panoramic view of the Multilab coating facility at DTU Space. Top right can be seen the bell-shaped coating chamber.

2.1 Coating chamber

The coating facility at DTU Space is arranged with vertical sputtering cathodes pointing outwards in a circular vacuum chamber, see figure 2.2. Substrates are mounted on vertical mounting plates that are placed on a rotating ring in the sputtering chamber and the substrates pass in front of each cathode at a speed determined by the desired layer thickness.

After chamber is closed, a roughing pump and a turbo molecular pumps evacuates the chamber to a pressure of $\leq 2 \cdot 10^{-6}$ Torr before pure Ar gas is let into the chamber at a constant flow rate to ensure the fraction of other gases to be <0.1%. The desired total pressure with Ar gas is $2.8 \cdot 10^{-3}$ Torr, which is as low as possible while maintaining plasma stability (see sec. 2.1.1).

The chamber fits four cathodes at a time and the Multilab has six in total, so two can be serviced while the other four are in use. For most coatings, only two or three cathodes at a time are necessary for the same number of materials.

In the earlier software solution, all cathodes were switched on at the same time during deposition of a bilayer. That necessitated two cathodes running with the low-Z material while one cathode ran with the high-Z material in order to achieve the correct Γ value and to have each cathode running in a possible power regime. A typical Pt/C multilayer for NuSTAR required $\Gamma = 0.6$, which meant that 60% of a material in a bilayer had to be carbon. Platinum and carbon has vastly different coating rates, so one cathode with platinum running at 150 W required two cathodes of carbon running at 900 W in order to achieve $\Gamma = 0.6$. With the new software only one cathode with each kind of material is necessary, but at the expense of a longer coating time.

A new software solution was created for the coating facility based on the SPEC software package, described in detail in appendix F.

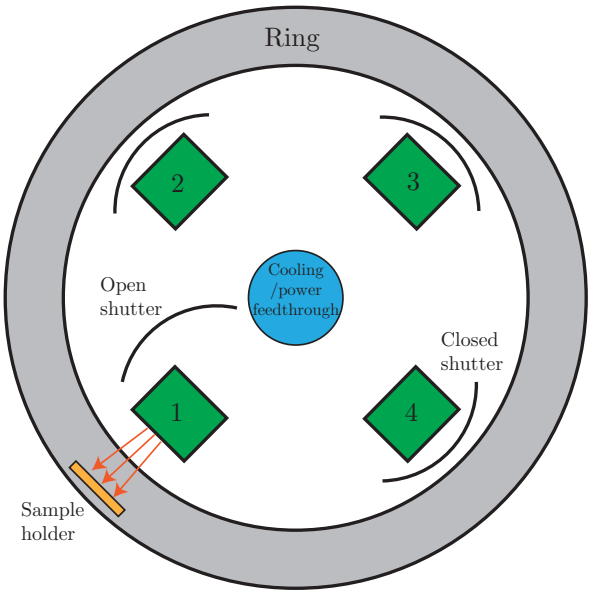

Figure 2.2: Diagram of the coating chamber at DTU Space, showing the principle of the rotating sample ring stage. Cathodes 1–4 (green) points outwards and can be covered with a shutter. Water cooling and power lines for the cathodes comes from the floor in the center of the chamber (blue) and connects to the top of each cathode with vacuum flex tubes. The sample (orange) is placed on a vertical plate that is mounted on the ring (grey). The ring rotates, so the samples move past the cathodes and gets coated with a film thickness related to the ring speed.

2.1.1 Magnetron cathodes

The cathodes are the most important part of the chamber. They are 20 inches long and 1/2 inch wide planar magnetron cathodes made by Angstrom Sciences Inc. A diagram of the cathode can be seen in figure 2.3. A copper block acts as the cathode with a stainless steel shield around it, separated by teflon spacers. Inside the copper block, three permanent magnets with alternating field directions supplies a magnetic field in front of the cathode. Water cooling and power lines are connected from the cathode through a flexible vacuum tube to water cooling and power supplies outside the chamber. The anode shield is grounded along with the rest of the chamber.

Materials for sputtering, called targets, are fastened to the copper block using a stainless steel clamp. It is important for the target to have a uniform contact with the cathode, so the copper block should be cleaned before fastening using cleanroom wipes and ethanol. For tougher blemishes, a micro-fine sanding sponge can be used to clean the surface followed by ethanol and cleanroom wipes.

Applying a voltage of -400 V to the cathode creates an electric field in front of the target. The argon gas present in the chamber will be ionised in front of the cathode by the electric field, stripping an electron from the argon atoms resulting in a plasma. The positive Ar^+ ions are accelerated towards the target, whereby the collision with the target create a sputtering of target atoms in a cone directed normal to the target surface, see figure 2.4. A substrate placed opposite the cathode will be coated with the sputtered atoms at a rate

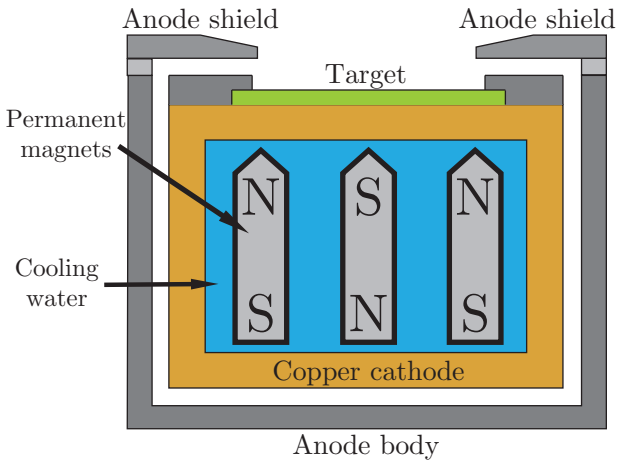

Figure 2.3: Cross-sectional diagram of a magnetron cathode used in the Multilab at DTU Space. A water cooled copper block has a negative voltage applied, while the anode shield surrounding it is grounded. Inside the copper block are permanent magnets supplying a magnetic field in front of the target.

proportional to the electric current applied to the cathode.

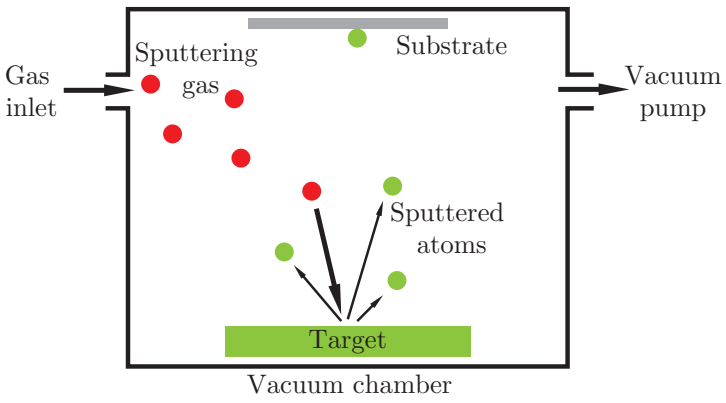

Figure 2.4: Principle of sputtering. Sputter gas led into an evacuated chamber is forced to the surface of a target with a force that rips atoms from the material. The freed target atoms move away from the target and some hit a substrate opposite the target.

Electrons stripped from argon atoms are captured by the magnetic field lines from the permanent magnets in the copper block. The electrons are moved back and forth across the target and occasionally hits neutral argon atoms, which also become ionised and thereby sustain the plasma. The movement of electrons are from the center of the target to the outer edge, and as more argon atoms are ionised in between those two points, the main erosion of the target during coating takes place in a so-called *race track* around the target.

Without the magnetic field trapping electrons to sustain the plasma, a higher electric field strength of -600 to -1000 V would be needed. When initially starting the sputtering process, the specialised power supplies at DTU Space will start with a voltage of -800 V before dropping to -400 V as soon as the plasma is stable. During operation the plasma can become unstable due to a number of factors, such as:

- Charge build-up on target (only non-metallic materials).
- Delamination of material deposited on anode shield, causing shorts.
- Bending of anode shield due to heating and cooling after extensive usage.
- Low argon pressure, thereby limiting the self-sustaining ability of the magnets and electrons.

The charge build-up are localised areas on the target where the conduction is too low. It can be caused either by contact between copper cathode and target not being sufficient or by a build-up of material on the target surface, e.g. nitrogen in reactive sputtering. Non-metallic targets used in magnetron sputtering are usually doped to make them conductive. However, movement of electrons transverse to the electric field in the non-metallic target will still often be met with too high a resistance. The localised charge will often result in an *arc*, which is a sudden discharge from cathode the grounded anode shield. The charge will also locally change the electric field in front of the target and thereby the plasma density, since the plasma is partly dependent on Ar^+ ions and electrons being separated by the electric field. The lower plasma density will also result in a lower coating rate locally, something that becomes problematic during deposition of precise multilayers.

2.2 X-ray lab source at DTU Space

Measurements at DTU Space were done with a reflectivity setup consisting of a rotating copper-anode providing X-ray photons for two beams. One beam is used for reflectivity measurements and the other can be set up for measuring curvature in glass substrates.

After the source, along the z-axis, is placed two slits, a monochromator, an attenuator, on more slit, the sample holder and finally the detector, see figure 2.5. The first two slits ensures that only a narrow beam hits the monochromator, which then reflects only photons around the copper K_{α_1} emission line (8.047 keV) by reflecting the beam on two germanium crystals at an angle where Bragg reflection only allow photons of that energy. The beam continues through the next two slits, thereby minimizing divergence and also filters out a large part of unwanted reflections from the monochromator to ensure a narrow bandwidth. The attenuator ensures that the beam intensity is not too large, thereby saturating the detector.

The sample holder consists of a slab of flat perforated ceramic material, a vacuum chuck, mounted vertically. It is connected to a pump, which allows flat substrates, like pieces of Si-wafer, to stick very firmly to the stone slab. This method of sample mounting makes it possible to change samples very fast and easy between measurements. The sample holder is centered and mounted on a rotating stage, θ, and can also move in and out of the beam along the x-axis.
After the sample holder, 995 mm further along the z-axis is a 10 cm wide 2D methane-gas detector mounted on a rotating stage, 2θ. It is centered on the same axis as θ, allowing the

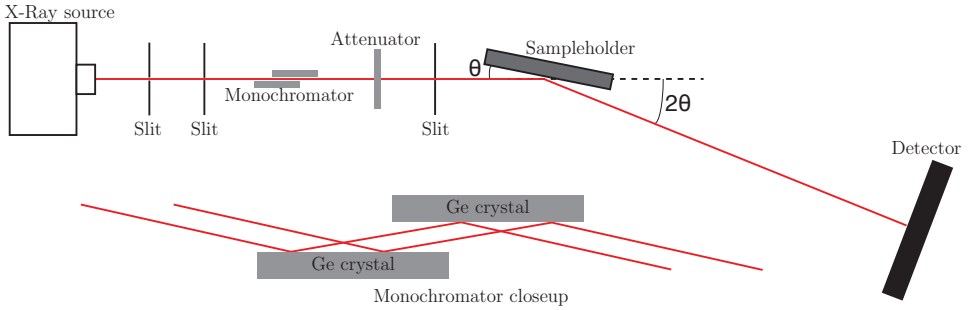

Figure 2.5: Diagram of the X-ray setup at DTU Space. X-ray photons from the source goes through two slits, a monochromator, an attenuator and one more slit before hitting the sample. The reflected photons from the sample travel to the detector which is rotated at a 2θ angle. Below: The monochromator that consists of two germanium crystal that reflect only a given wavelength on the (111) surface using the Bragg principle.

detector to move 90°around the sample while maintaining a focus on the same spot. The detector has 2000 channels along the x-axis of the beam; 100 channels are used during a measurement, giving a horizontal detector aperture of 2 cm.

2.3 Coating calibration

To deposit a coating with the correct film layer thicknesses on a substrate, a calibration of the material combination is required. Four samples of 10 bilayer films are coated using the two materials. Each sample is placed on a separate mounting plate and each coated with a different thickness of both light and heavy materials. The samples are then measured using XRR and compared to an IMD[22] model fit to get bilayer thickness (d-spacing) and light/heavy material fraction (Γ) as seen in figure 2.6.

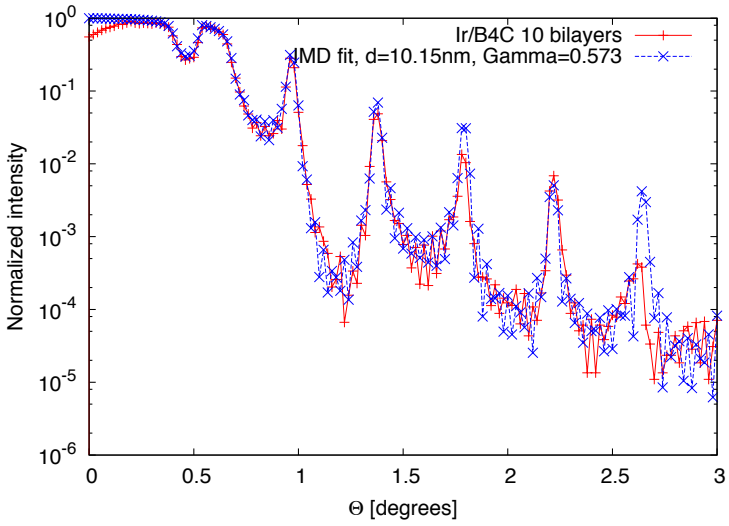

Figure 2.6: XRR measurement of a 10 bilayer Ir/B_4C coating to calibrate for SPO coating. The measurement is fitted with an IMD model to determine d-spacing Γ.

The result for each sample is used to get the specific thickness of a material when coating with a given speed. Each result from the IMD model fitting is put into a table like the following:

Sample	speed (Ir)	speed (B_4C)	d-Ir [nm]	d-B_4C [nm]
si5809	2623	473	2.42	2.54
si5810	1445	338	3.21	3.88
si5811	1011	236	4.33	5.81
si5812	674	158	6.40	8.85
si5813	281	225	14.55	7.49

The d-spacings for a given material are plotted as a function of the inverse speed of the sample ring (v^{-1}) and fitted with a linear regression as seen in figure 2.7. The a and b values of the linear regression are used directly to determine the speed of the sample ring, v_{B_4C}, to coat e.g. boron carbide with a thickness of d_{B_4C} like so:

$$v_{B_4C} = \frac{a}{d_{B_4C} - b}. \tag{2.1}$$

where a is the slope of the fitted line and b is the value of d_{B_4C} at $1/v_{B_4C} = 0$. Using this method can easily yield the needed ring speeds for a complex coating using e.g. Microsoft Excel.

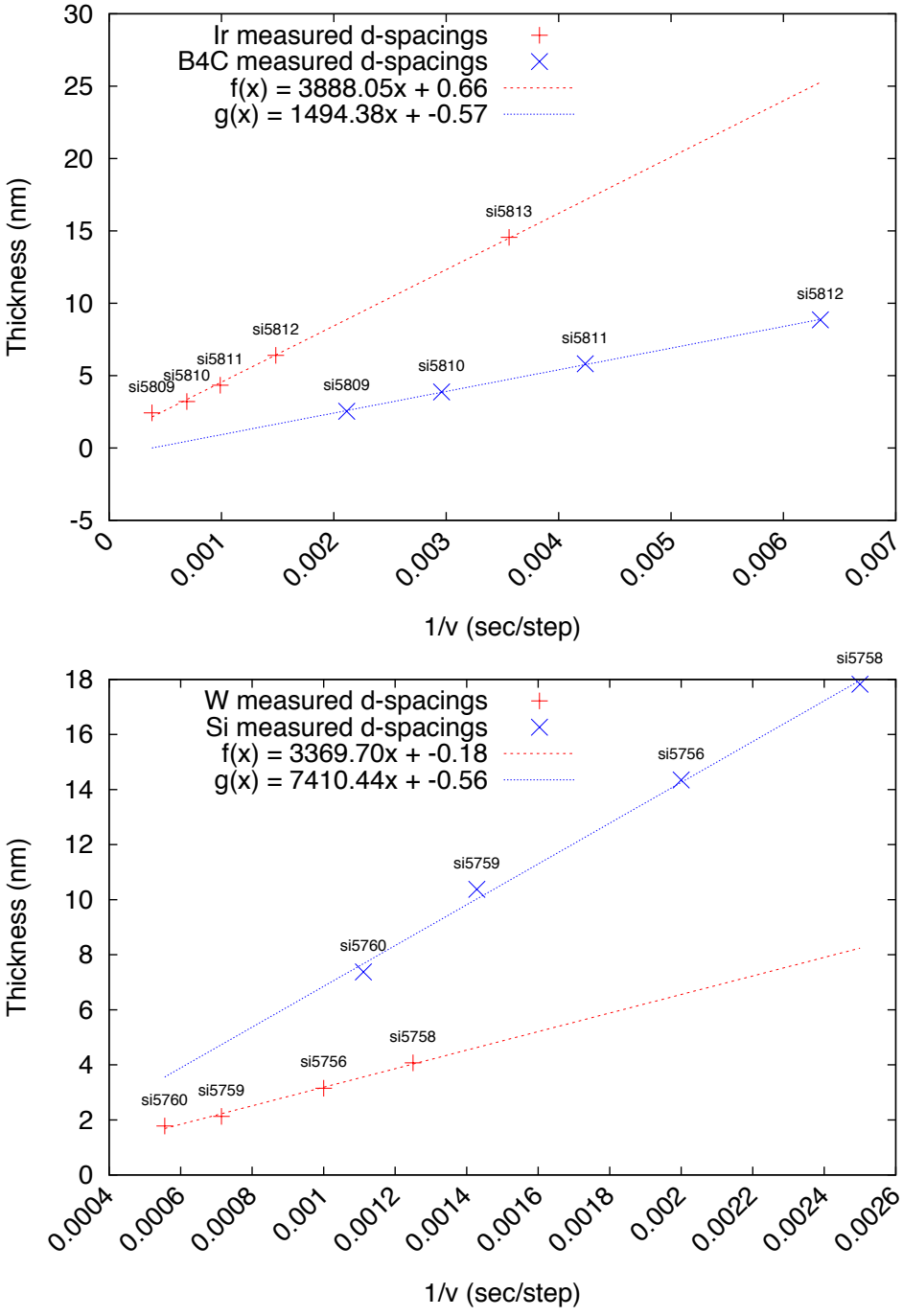

Figure 2.7: Linear regression fits of calibration samples for Ir/B_4C (top) W/Si (bottom). Each datapoint is the XRR measured thickness of one material layer in a sample.

Chapter 3

Coatings for the Athena X-ray observatory

In this chapter are described developments and investigations in the coating technology required for the European Athena mission. The work started in spring 2011 and is still ongoing. It now involves five employees and students at DTU Space.

The first part of the chapter describes the Athena telescope and optics technology. Afterwards is a description of the X-ray reflective coating investigation carried out at DTU Space, starting with the baseline coating and stress investigation in [23]. Proceeding that is the work based on different optimization techniques for multilayer coating deposition, namely reactive sputter deposition and pulsed-DC sputtering. The coating lab acquired a pulsed-DC power supply specifically for the Athena coating investigations, but no improvements were found. Additionally, a number of problems showed up with the new power supply and the causes were not clear. Reactive sputtering investigations revealed major problems with some material combinations that included boron carbide, which became apparent after long term storage investigations. In the end, the baseline material combination that was initially proposed for Athena was found to be the best-performing and most stable solution.

The last part of this chapter (section 3.5) is based on a report written to ESA on the coating production facility requirements for the original Athena mission proposed in 2012. A significant effort will have to be put into mass production for the Athena optic to be realised. The section points out the cost and timetable of such an effort.

3.1 The European Athena mission

Design and development of the Athena mission was started already in the 90's as first a European mission (XEUS) with the intent to make a high resolution X-ray telescope with a large effective area (see section 1.1.1). In 2008 it merged into IXO (International X-ray Observatory), a European/American/Japanese collaboration. In 2012 after some years of global financial crisis, the collaboration fell apart as a result of down-scoping of space-related projects.

The European Space Agency (ESA) continued development of a smaller mission using technology that had already been in development for IXO for almost a decade. The mission was Athena (Advanced Telescope for High-ENergy Astrophysics)[24], but was not selected as the 2022 large (L1) mission by ESA. Development continued under the Athena+ name, and the project was eventually selected for the L2 mission to be launched in 2028. To avoid confusion, Athena+ was after selection renamed to Athena.

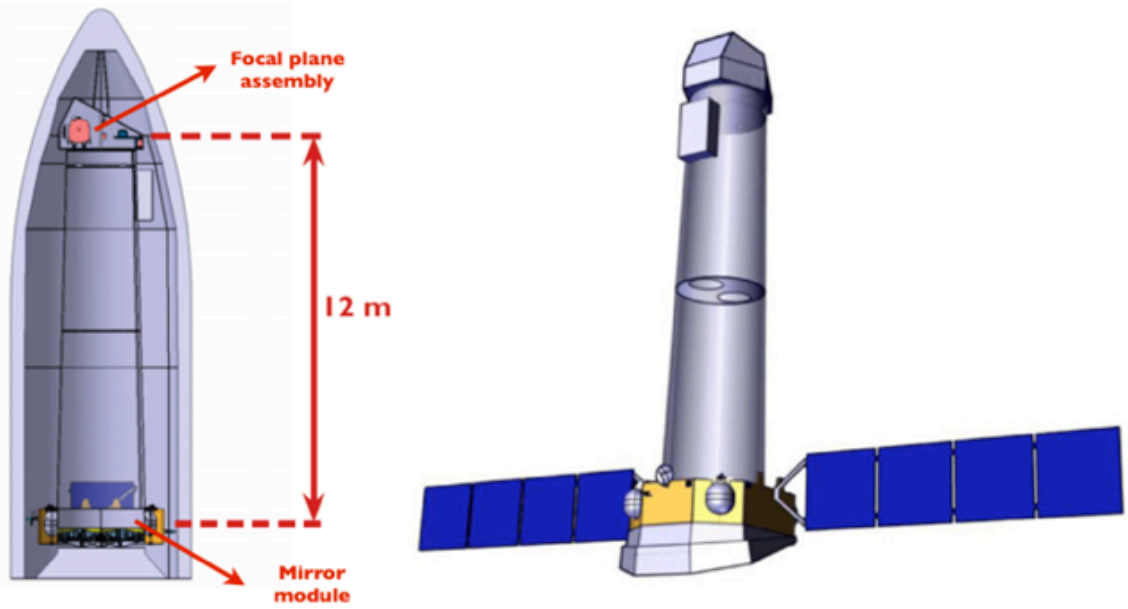

Figure 3.1: Illustrations of the Athena X-ray telescope. **Left:** Inside Ariane V fairing. **Right:** In space with extended solar panels. The optic is in the bottom end. (from `www.the-Athena-x-ray-observatory.eu`).

The theme of the 2028 L2 mission is *The Hot and Energetic Universe*, which aims to answer the questions:

1. How does ordinary matter assemble into the large scale structures that we see today?
2. How do black holes grow and shape the Universe?

The first question might be answered by looking at galaxy clusters from their formation at $z \sim 2$–3 until present day. As the structures grow over time due to accretion of hot gas they eventually become the largest bound structures in the universe. To understand the growth, it is necessary to get information about velocity, thermodynamics and chemical composition of the gas. The high temperature of the gas results in considerable amounts of X-ray emission and the goal is to measure the spectroscopic output of galaxy cluster from $z = 1$ and beyond. In order to study the morphology of such clusters and in order to get spectroscopic information, a telescope with a large collecting area and good spatial resolution is required.

The second question could be answered by looking at the supermassive black holes at the centers of galaxies. By looking at the epoch where the first galaxies were forming at $z =$

6–10, the growth of the black holes can be tracked. However, that will require survey capabilities ∼100 times better than available with current X-ray telescopes. It will require a wide field of view as well as high sensitivity, which depends on large throughput and good spatial resolution.

In conclusion, the mission calls for high energy and spatial resolution spectroscopic observations and deep wide-field X-ray imaging. The performance in these areas should greatly exceed instruments currently in use such as Chandra and XMM-Newton as well as future missions such as Astro-H and eRosita. The improvements are to be realised with an effective area of 2 m^2 at 1 keV, 5" angular resolution and 40'x40' wide field-of-view[25].

3.1.1 The Athena reflective coating baseline

The baseline coating for Athena is an Ir/B_4C single bilayer, an iridium layer of 11 nm topped with an 8 nm boron carbide layer. The iridium will reflect higher energy X-rays in the 0.1–10 keV energy range, and the boron carbide top layer will reflect lower energies. The boron carbide material is able to withstand the C-C bond-breaking chemical solutions applied in the last step of the lithographic process (described in section 3.1.4), while at the same time being a very light material. The low electron density gives boron carbide a very good reflectivity at energies 0.1–∼3 keV. In investigations done by Lumb et al are results of measurements on an Ir/C single bilayer, where the C overlayer results in a doubling of effective area of the former XEUS telescope at 2–4 keV[26]. This effect is due to the lower photoelectric absorption in low density materials such as boron and carbon in total reflection mode[27]. In figure 3.2 can be seen the performance of the Athena X-ray telescope using a single bilayer coating compared to earlier comparable missions.

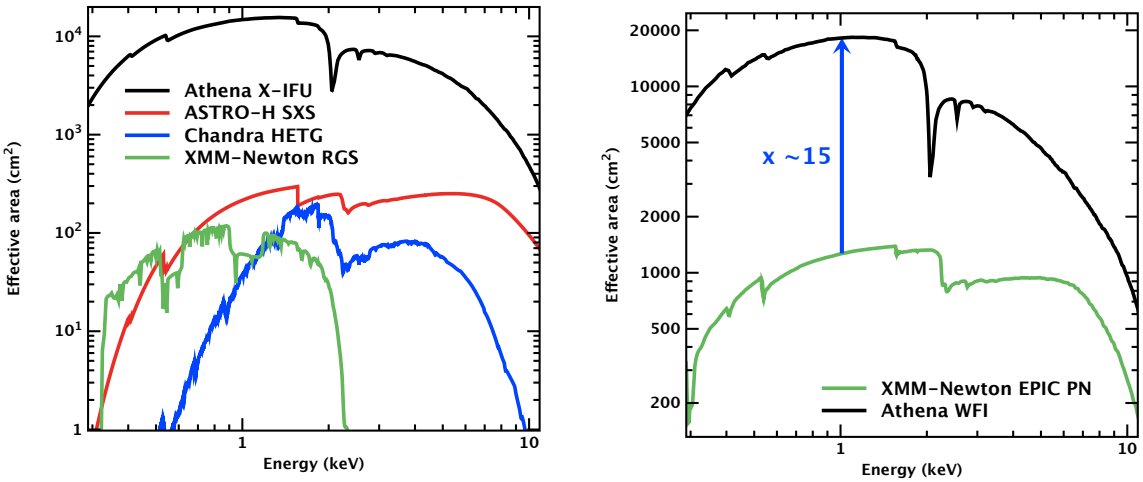

Figure 3.2: Athena performance compared to earlier missions. **Left:** Effective area for high-resolution spectroscopy. **Right:** Effective area for imaging and medium-resolution spectroscopy. From [28]

The Ir/B_4C combination does however have some drawbacks, especially high compressive film stress. Additionally, the Ir/B_4C material combination is not described in the literature,

so the interplay between the two materials in both the short and long term is relatively unknown. In appendix A can be found a paper from 2011 that investigates the baseline Athena coating along with solutions to handle the film stress. In section 3.2.2 is a continuation of the investigation into stress improvements.

3.1.2 Coating optimisations for Athena

To improve on the Athena baseline coating, a range of alternative material combinations were investigated using computer optimisation with Markov chain Monte Carlo methods by Desiree D. M. Ferreira at DTU Space. A number of optimised coating recipes were produced for each material combination and the actual coatings were subsequently produced on SPO substrates in the coating lab at DTU Space. In appendix B (see also [29]) can be found a paper from 2012 on some of the optimizations and investigations done on coatings applied to SPO substrates.

The material combinations investigated in this thesis are:

Ir/B_4C single bilayer (baseline) The baseline material combination that yields the effective area of 2 m^2 at 1 keV for Athena.

Ir/B4C multilayer An improvement on the baseline using the same material combination. A stack of bilayers is designed to improve the reflectivity around 6 keV while still retaining the baseline effective area.

W/B_4C multilayer A combination with lower stress (see sec. 3.2.2) and cheaper materials than the Ir/B_4C multilayer.

Pt/B_4C single bilayer A backup of the baseline material combination if the stress proved to be too high for the SPO substrates.

3.1.3 Athena optics technology

ESA has for the past decade been working on a radically new optics technology for future X-ray missions, the Silicon Pore Optics (SPO)[24, 30, 31, 30, 31, 32]. By using silicon wafers, cut into rectangular shapes (diced) and with grooves cut into the underside, a high collecting area can be achieved with very low mass and at the same time achieve angular resolution better than NuSTAR-like glass.

The silicon wafers are diced, wedged and grooves are cut into the underside, see figure 3.3. The grooves are 0.83 mm wide and spaced only 0.17 mm apart, resulting in narrow ribs in the underside. The grooving has two purposes: First, the wafer becomes so thin that it is bendable transversely to the ribs. Second, the SPO substrates can be stacked directly on top of one another with the ribs bonding to the surface of the substrate underneath. The

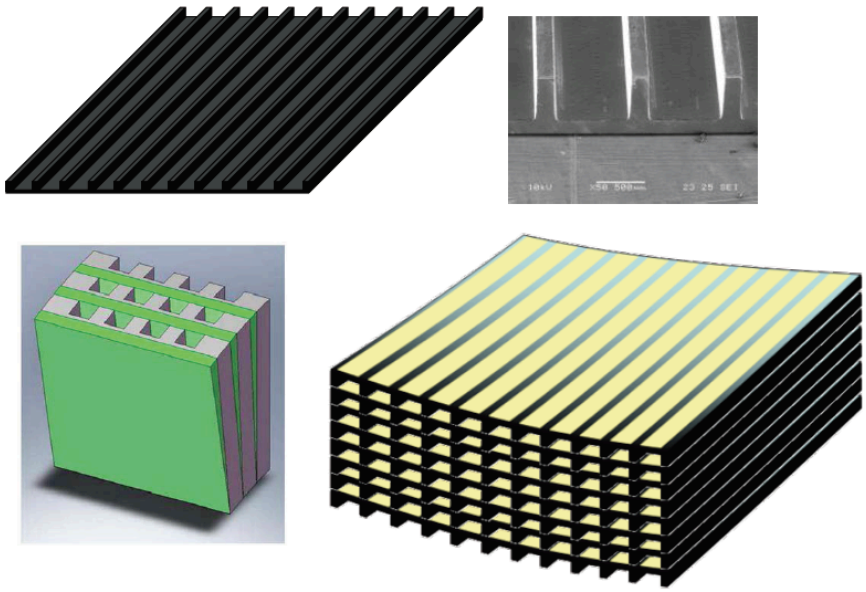

Figure 3.3: Principles of the Silicon Pore Optic (SPO) technology. **Top:** Silicon wafers are diced into rectangular pieces and grooves are cut in the underside. **Bottom left:** The wafers have a wedge applied with SiO_x and are stacked so all SPO substrates reflect to the same point. **Bottom right:** SPO substrates are stacked at a curvature corresponding to the radius at which they are placed in the optic. A reflective coating is applied in stripes on each substrates. (from [25]).

X-rays will the be able to pass between the ribs and reflect on the surface of the bottom substrate. Stacking 68 of the SPO wafer substrates results in a very light, but very rigid block of silicon with micro-pores and a reflecting surface inside each pore. In order to have the SPOs reflect photons to the same spot, a wedge is applied to each reflecting surface corresponding to the angle required, see figure 3.3 bottom left. The wedge is made from SiO_x etched to the correct thickness and slope.

As the SPO substrates can be bend, they are stacked on a mandrel with the exact curvature needed. The high-precision stacking process is done by a dedicated robot in a controlled ultra-clean environment, as single dust specks can offset the stacking precision.

Two stacks of 68 SPO substrates constitutes an SPO module as can be seen in figure 3.4. Each stack will reflect an incoming X-ray photon once, so two stacks acts like a conical approximation to the double-reflection Wolter I optic. However, in order to achieve sub-10" angular resolution as specified by the science-criteria for ESA, the SPO technology will need to achieve a true Wolter I shape. Several initiatives by ESA are underway to achieve this as of 2014.

Each SPO module is self-consistent, making the entire optic technology modular. When a module is ready, it can be slided into a light-weight construction. This is in contrast to the NuSTAR technology (see section 1.1.2) where each layer had to be mounted sequentially. The modularity is also a necessity when it becomes apparent that an effective area of 2 m^2 at 1 keV requires 1.5 mil. pores. As Athena is a large ESA mission, the Ariane V rocket will be used and the telescope is designed with the size limitations of the Ariane V fairing in mind, resulting in a telescope with $\sim$3 m diameter and $\sim$13 m length. To populate an

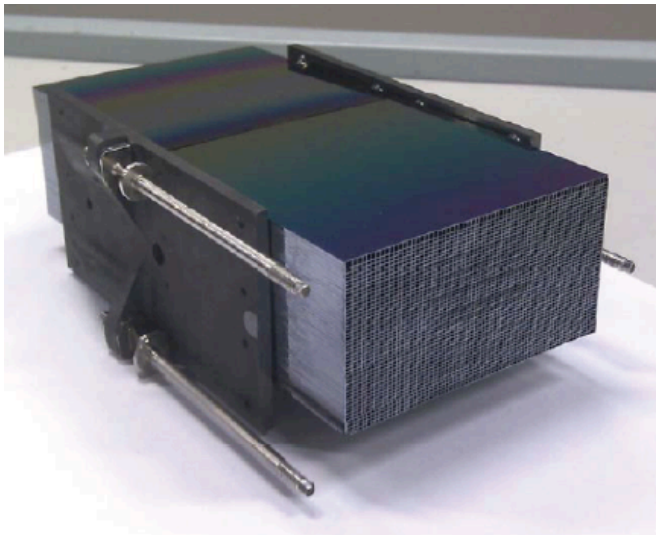

Figure 3.4: A complete SPO mirror module. Two stacks of 68 SPO substrates are glued together with a pair of Cesis plates, making them co-aligned with 1" precision. The complete module reflects an incoming X-ray photon twice and thus acts as both paraboloid and hyperboloid of the Wolter I optic. (from [25]).

optic with a diameter of ∼3 m, the number of SPO modules needed are ∼1,090 as can be seen in figure 3.5.

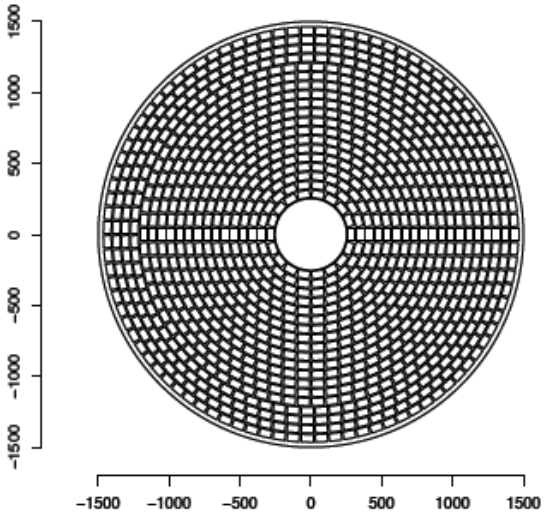

Figure 3.5: The complete Athena optic. SPO mirror modules are arranged in rings to populate the aperture. (from [25]).

As each optic module consist of $2 \cdot 68 = 136$ SPO substrates, a total of $1090 \cdot 136 \approx 140,000$ SPO substrates are needed, not accounting for spares or broken substrates. Considering that the NuSTAR telescope consisted of $2 \cdot 2376$ glass substrates and took two years to produce, it becomes apparent that the Athena mission will require a large-scale production facility. In section 3.5 can be found an investigation in the coating side of the production facility requirements for the Athena mission.

3.1.4 Reflective coatings on SPO substrates

One of the most important principles of the SPO technology is the ability for the SPO substrates to bond when stacked. It is achieved by pressing the surface of one SPO substrate against the ribs of another SPO substrate. Since the SPO substrates are wedged with a SiO_x material, both ribs and surface consist of SiO_x and pressing the two substrates together forms a strong covalent bond, thereby fusing the two.

In order to apply a reflective coating to each of the SPO substrates, the bonding process has to be taken into account. Applying a coating with a physical vapor deposition process such as DC magnetron sputtering will coat the whole surface, but by using a lithographic process from the semiconductor industry it is possible to apply coatings in patterns on a surface. The pattern being the exact position where the ribs will touch the surface when stacking, so these areas are $\sim$0.17 mm wide, covers the entire length of the substrate surface and are spaced $\sim$0.83 mm apart. The lithographic process involves the following (also seen in figure 3.6):

- Applying a resist film on the substrate surface.
- Curing the resist with e.g. a UV light in a striped pattern corresponding to the ribs of the SPO substrate.
- Removing the un-cured resist with a chemical solution (the developer).
- Coating the substrate with a reflective coating.
- Removing the cured resist including the coating applied on top of the resist using acetone or dimethyl sulfoxide (DMSO).

The lithographic process puts requirements on the reflective coatings applied to the SPO substrates since chemical solutions used in the last step are designed to break carbon-carbon bonds. All multilayer coatings with pure C as the low-Z material are excluded as the last step described above will simply break apart the coating.

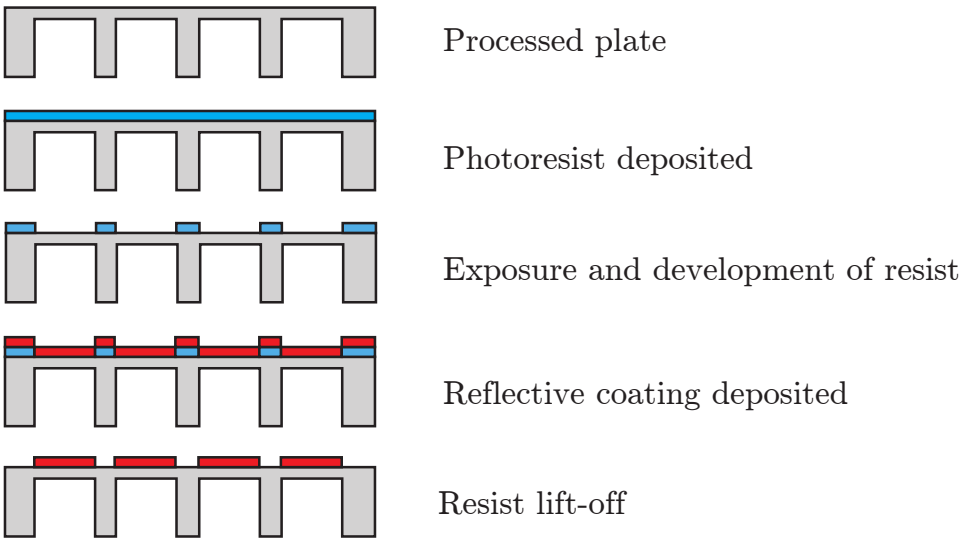

Figure 3.6: . The lithographic process applied to SPO substrates to achieve a striped pattern of reflective coating.

3.2 Investigation of baseline Ir/B_4C material combination

In this section is described the effort to identify the Ir/B_4C material combination performance based on coatings made at DTU Space on SPO substrates.

Production of Ir/B_4C single bilayer and multilayer coatings on SPO substrates were carried out in the Multilab at DTU Space. The optimised recipes can be found described in appendix B, diagrams of the optimised coatings can be seen in figure 3.7. The multilayer coating is basically a five bilayer linearly graded coating underneath a baseline coating. The combination ensures that the baseline effective area requirements for Athena will be met and the five bilayers underneath will increase the effective area around 6–6.5 keV[1].

The SPO substrates were coated with an iridium cathode power of 450 W and a boron carbide cathode power of 900 W at a pressure of 2.9 mTorr with an Ar flow of 88 sccm. The base pressure was $< 2 \cdot 10^{-6}$ Torr.

The SPO substrates are mounted on sample plates in the chamber with ribs horizontally; the horizontal movement of the sample ensures good uniformity in the rib direction. XRR measurements (X-Ray Reflectivity, see sec. 2.2) performed after coating are done in the same direction along the ribs, so the coating is uniform in the footprint of the X-ray beam. In figure 3.8 can be seen an XRR measurement and IMD fit of an SPO substrate coated with a Ir/B_4C multilayer.

[1]The iron K_α line is 6.4 keV and is an extremely useful emission line in astrophysics.

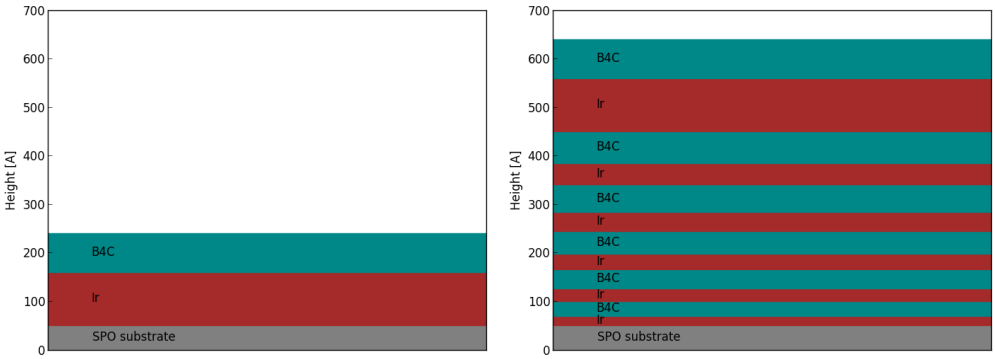

Figure 3.7: Side-view diagrams of Ir/B_4C coatings for Athena. **Left:** The baseline Ir/B_4C single bilayer. $d_{Ir} = 11.0$ nm, $d_{B_4C} = 8.0$ nm. **Right:** The multilayer coating optimised for the middle part of the Athena optic. Consists of five bilayers with $d_{min} = 5.0$ nm, $d_{max} = 11.0$ nm, plus a cap layer of iridium of $d_{Ir} = 11.0$ nm and a top layer of boron carbide of $d_{B_4C} = 8.0$ nm.

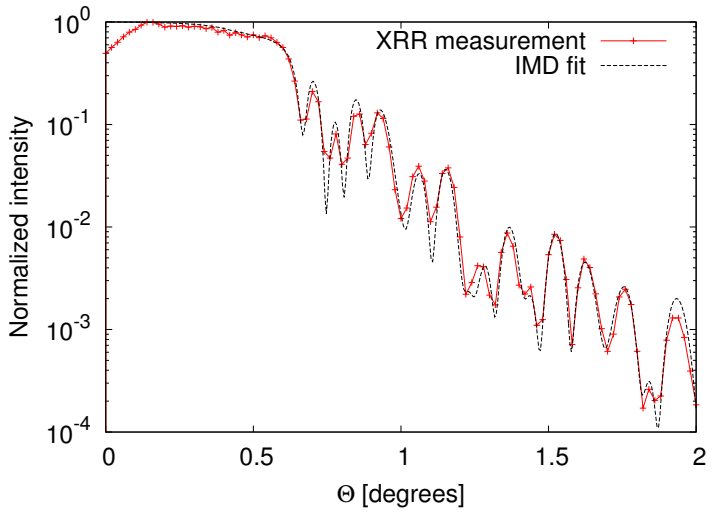

i	d_{aim} [nm]	Γ_{aim}	d_{fit} [nm]	Γ_{fit}	σ_{Ir}[nm]	σ_{B_4C}[nm]
top	8.0	1	7.17	1	-	0.60
cap	11.0	0	11.09	0	0.49	-
1	11.0	0.6	11.43	0.620	0.43	0.42
2	9.5	0.6	9.99	0.617	0.56	0.50
3	8.0	0.6	8.54	0.623	0.37	0.44
4	6.5	0.6	6.95	0.576	0.60	0.51
5	5.0	0.6	5.85	0.567	0.47	0.46

Figure 3.8: XRR measurement of SPO substrate coated with optimised Ir/B_4C multilayer, compared to IMD model fit. Fitted values are shown below.

The IMD fit was done using the differential evolution algorithm[33] included in IMD from version 5.0. The fitting results show that each layer is thicker by up to ∼17% (for the thinnest layer). Γ-values are also off by ∼-5.5% for the thinnest layer and ∼3.3% for the thickest layer. It should be noted that the fit is not perfect and the maxima and minima of the model at lower angles that does not correspond to the data can be caused by the low-Z material not having the correct thickness. Using 8 keV XRR to determine the thickness of a low-Z toplayer in a multilayer is difficult since there is little interaction between the

relatively high energy photons and the light material.

The coated SPO substrates were also measured at the FCM beamline at the BESSY II synchrotron at PTB in Berlin. Energy scans at 1.8–10 keV can be performed there that will give an indication of the coating performance at low energies, although not at 0.1–1.8 keV. A measurement of an SPO substrate with Ir/B_4C multilayer coating can be seen in figure 3.9. Two measurements are performed at different spots spaced 5 mm apart. The reflectivity response at low energies is well-behaving, showing no sudden drops that would indicate contamination from other elements in the coating. There are two small dips at ∼2.1 keV and ∼2.5 keV, corresponding to iridium M_α-edges.

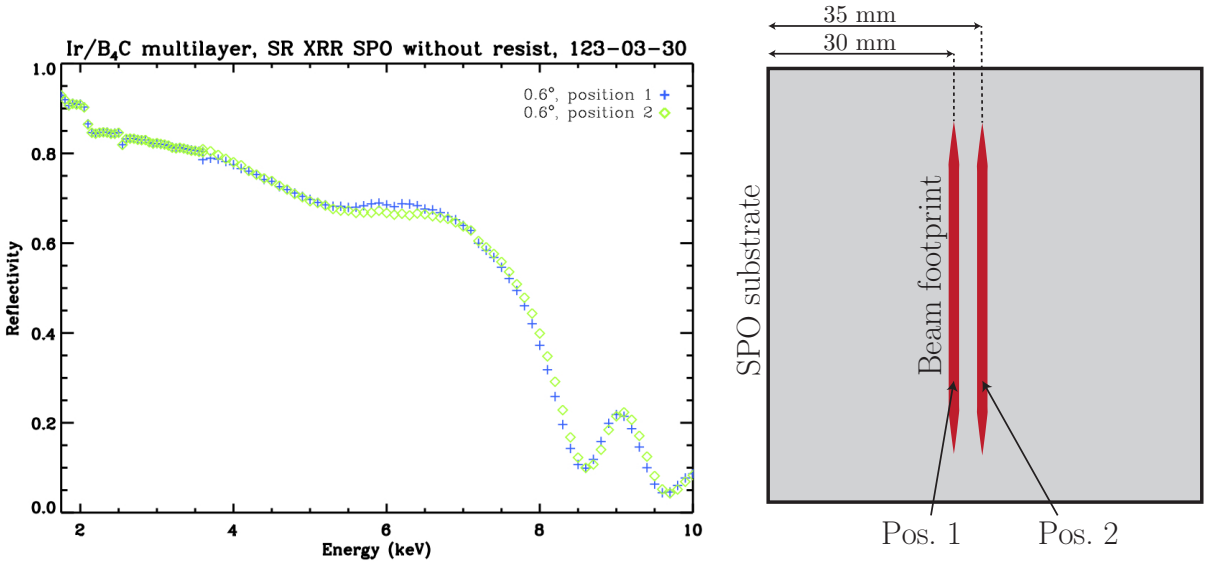

Figure 3.9: XRR measurements at the 1.8–10 keV energy range and a 0.6° angle, performed at the FCM beamline at BESSY II. **Left:** Two measurements of the same sample are shown from different positions to investigate non-uniformity of the coating. **Right:** The two measurement positions marked on the sample.

3.2.1 ISO qualification of Ir/B_4C coatings

The combination of iridium and boron carbide in reflective coatings is not easily found described in the litterature and is overall not well documented. If the coating combination should be launched to space, a significant effort is needed to make sure that the combination is stable. This qualification to ensure stability is part of the overall qualification needed on every piece of equipment to be launched to space.

In order to qualify the Ir/B_4C coatings on SPO substrates for the Athena mission, a range of tests were conducted on coated substrates. Qualification testing is a cornerstone of developing hardware for space based applications, so a number of standardisations have been developed over the years. Each standardisation applies to a specific type of hardware that needs to be qualified. The European Space Agency works with the *International Organization for Standardization* (ISO) for optical devices and optical coatings as well as

the *European Cooperation for Space Standardization* (ECSS). The specific tests that ESA outlines as required to qualify coated optical devices are:

- A **thermal** cycling test according to *ECSS-E-10-03A (AD4) Space engineering, testing.*

  > General purpose: "[...] of the thermal cycling test is to demonstrate the ability of the equipment under test to fulfil all functional and performance requirements over the qualification temperature range at ambient pressure."

- A **humidity** test according to *ISO9022-2 (AD6) Optics and optical instruments, Environmental test methods, Part 2: Cold, heat and humidity.*

  > General purpose: "[...] to investigate to what extent the optical, thermal, mechanical, chemical and electrical performance characteristics of the specimen are affected by temperature and/or humidity."

- An **adhesion** test according to *ISO9211-4 (AD5) Optics and optical instruments, Optical coatings, Part 4: Specific test methods.*

  > General purpose: "[...] of these tests is to evaluate to what extent the mechanical properties of optical coatings on components and substrates are affected when subjected to specific tensile or shear stress conditions at ambient atmospheric conditions."

Each test is described in detail in each of the documents listed above as well as the requirements that has to be met for a device or sample to succeed the test and qualify. The coated samples used in these tests were measured using XRR before and after deposition. A visual inspection was also performed.

Four SPO substrates were coated for qualification testing, two with a single bilayer baseline Ir/B_4C and two with optimised Ir/B_4C multilayer. A baseline and multilayer sample were used for both thermal cycling and humidity tests. The samples from the humidity tests were reused for the adhesion test. All tests were carried out by David Girou from DTU Space.

The thermal cycling test consisted of eight cycles in an oven (no vacuum). One cycle was divided into two hours spent at $T_{max} = 85^{o}$C $\pm 10^{o}$C and two hours spent at $T_{min} = -45^{o}$C $\pm 10^{o}$C. The test was divided into two times four cycles since XRR measurements were performed after every fourth cycle. Inital and final temperature is 22°C. Temperature change rate was $dT/dt = 4^{o}\text{C}\cdot\text{min}^{-1}$ and after the last cycle the temperature was first increased to 40°C and then decreased to 22°C to avoid condensation.

Results of the temperature test can be seen in figure 3.10. No change is apparent apart from a misalignment of the first XRR measurement by 0.02^{o} of both the baseline and multilayer (red lines).

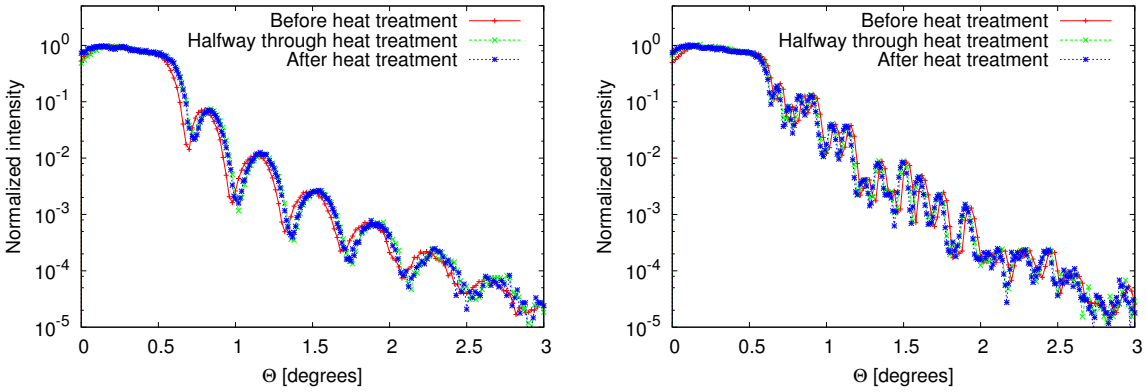

Figure 3.10: XRR measurements of Ir/B_4C coatings on SPO substrates before thermal cycling test, after four cycles, and after eight cycles. **Left:** Baseline Ir/B_4C coating. **Right:** Multilayer Ir/B_4C coating.

The humidity test consists of 48 hours spent at a temperature of 40°C and a relative humidity between 90% and 95%. Samples were measured with XRR before and after the humidity test, results can be seen in figure 3.11. No change in the baseline or multilayer XRR measurements after the humidity test.

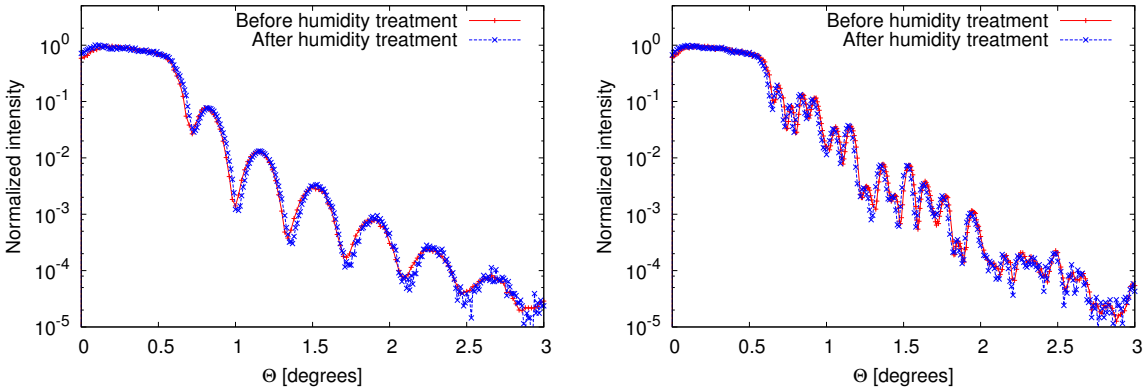

Figure 3.11: XRR measurements of Ir/B_4C coatings on SPO substrates before and after a humidity test. **Left:** Baseline Ir/B_4C coating. **Right:** Multilayer Ir/B_4C coating.

The adhesion test was performed using a 25x19 mm^2 piece of scotch tape applied firmly to the surface of the coating on the SPO substrate. The tape was subsequently snapped rapidly off the surface. A visual inspection of the surface was performed afterwards. The degree of success of the test is measured in how rapidly the tape is pulled off without taking the reflective coating with it. No amount of pulling could remove neither the baseline nor multilayer Ir/B_4C coating. XRR measurements were also done on the samples to ensure that the top boron carbide was not removed. As can be seen in figure 3.12, both multilayer and baseline coating were unharmed in the test.

It is worth noting that the Ir/B_4C coatings applied to the SPO substrates were without a chromium underlayer to decrease the film stress (described in section 3.2.2). With that in mind, the Ir/B_4C baseline and multilayer can be expected to have film stress of ~ -4 GPa and ~ -2 Gpa respectively.

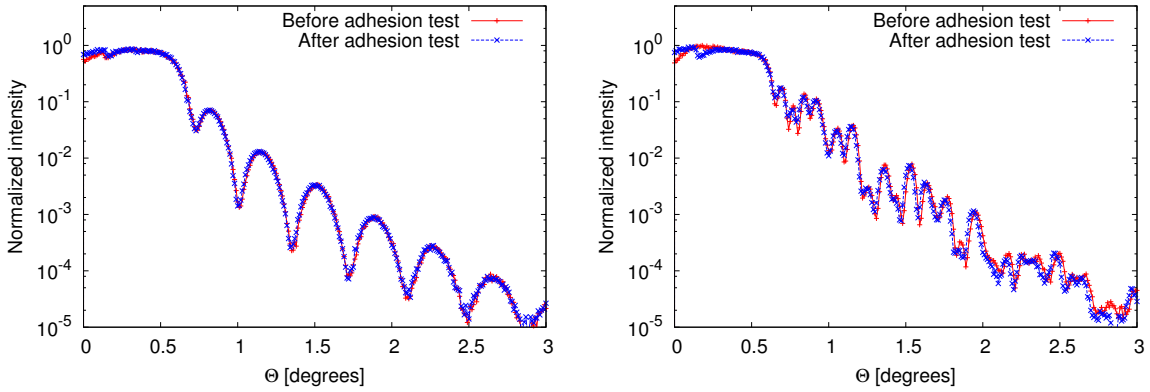

Figure 3.12: XRR measurements of Ir/B_4C coatings on SPO substrates before and after an adhesion test. **Left:** Baseline Ir/B_4C coating. **Right:** Multilayer Ir/B_4C coating.

3.2.2 Film stress in Ir/B_4C coatings

The baseline coating for Athena consists of a bilayer of iridium and boron carbide, both of which shows considerably film stress of up to ∼-4 GPa (compressive). High film stress of more than 1 GPa can in films cause deadhesion and "hillocks" on the surface of films with compressive stress. Some bending of the coated substrate will also result from high stress, the degree depending on substrate thickness.

To alleviate the stress in the film, earlier investigations has shown significant improvements in stress by using a chromium underlayer, which almost eliminates the total film stress (see app. A). The drawback of using chromium films is the high surface roughness, with r.m.s roughness of 0.8–1.0 nm normal for a 10 nm thick film. The following section investigates possible improvements to that roughness.

The following section describes investigations which are a continuation of the results obtained in the paper *Preliminary coating design and coating developments for Athena* found in appendix A. The reader is urged to read the paper first for a better understanding of the work done.

3.2.2.1 Improving roughness in stress-relieving chromium sublayers

We present here the results of two experiments with the purpose of reducing the chromium surface roughness. The first experiment is an attempt to decrease the rate of sputtered chromium atoms reaching the substrate. A lower rate will give an adsorbed chromium atom a chance to move to a lower position[34]. By decreasing the output power to the chromium cathode, while maintaining the same voltage of -400 V, the rate of sputtered atoms can be decreased. In figure 3.13 XRR measurements of chromium films coated at varying power output can be seen.

It is seen that at lower power settings, the hills and fringes become less pronounced, indi-

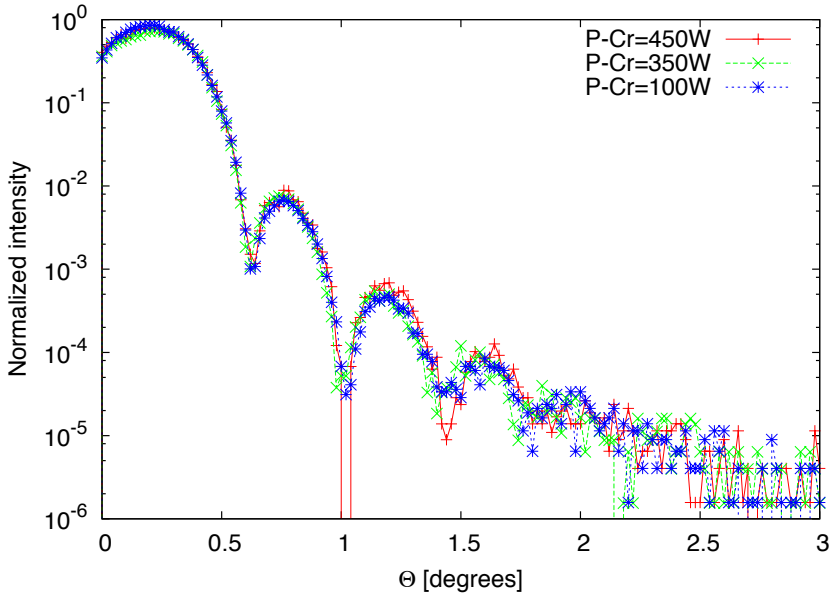

Figure 3.13: XRR measurements of four chromium single layer coatings made with varying power settings.

cating a higher roughness. This would indicate that the flux of sputtered atoms adhering to the substrate have time to coalesce into islands, thereby giving rise to island-growth also known as *Volmer-Weber* growth[35]. In that case, it would seem that lowering the power on chromium yields a higher surface roughness because given enough time, the chromium adatoms will form into their preferred configuration.

A second experiment involves changing the Ar gas pressure during coating. A minimum pressure is required in order to sustain the cathode plasma, but it is beneficial to coat at the lowest possible pressure. At a given pressure, the sputtered atoms going from target to substrate will have a chance of hitting an Ar atom given by the mean free path. A sputtered atom that would otherwise hit the substrate at a very low normal angle, will after having hit an Ar atom reach the substrate at a much higher angle, thereby giving rise to shadow-effects[36] as seen in figure 3.14.

By producing chromium coatings at varying Ar pressures and measuring using XRR, a correlation was found between Ar pressure and chromium surface roughness. The XRR measurements along with IMD fits can be seen in figure 3.15. A decrease in chromium surface roughness from 1.0 nm to 0.7 nm is seen when going from 2.4 mTorr to 1.5 mTorr Ar pressure.

Earlier investigations of the baseline Ir/B_4C coating with chromium sublayer[23] have hinted that the interface roughness of Ir/B_4C becomes lower than the interface roughness of Cr/Ir. A simple bilayer coating of Cr/Ir have now been made, where boron carbide can be factored out of the fitting procedure. The boron carbide has been left out, so to easier constrain the surface roughness of iridium and chromium in the fitting process as the model only has 4 variables compared to 6 variables for a $Cr/Ir/B_4C$ coating. The coating was made using the standard Ar pressure of 2.9 mTorr. XRR measurement of the sample can be seen in

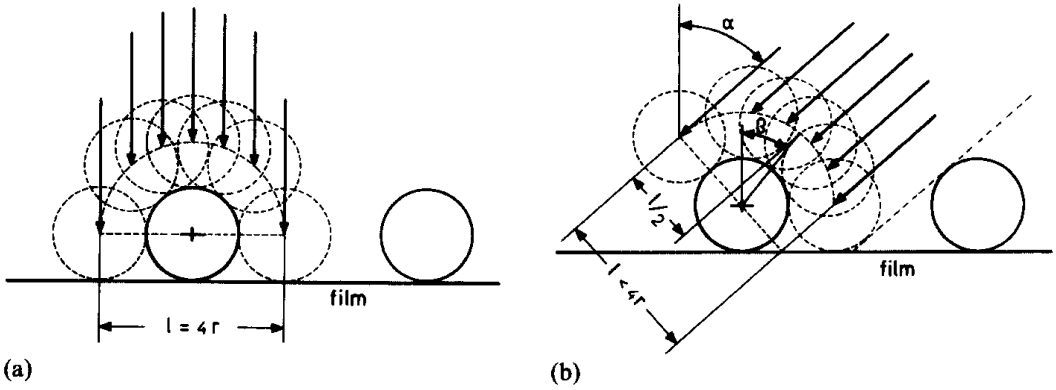

Figure 3.14: Principle of self-shadowing during angled deposition on a surface. At higher angles, incoming particles will have a tendency to adsorb on top of single particles already on the surface instead of filling gaps in the film. From [37].

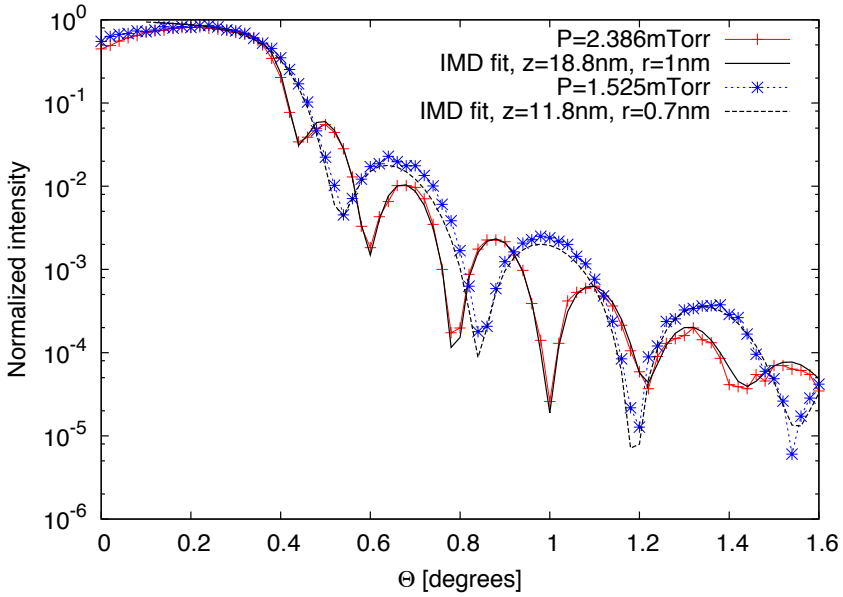

Figure 3.15: XRR measurements of two chromium single layer coatings made with varying Ar pressure. Blue points are IMD models fitted to the data.

figure 3.16 along with a an IMD fit. The fitted curve shows a Cr/Ir interface roughness of 0.62 nm and an iridium surface roughness of 0.3 nm. This is an extremely promising result, since the baseline Athena coating depends on the iridium surface for most of the energy response above ∼3 keV. So to have this surface smooth while at the same time keeping a low amount of film stress is reassuring.

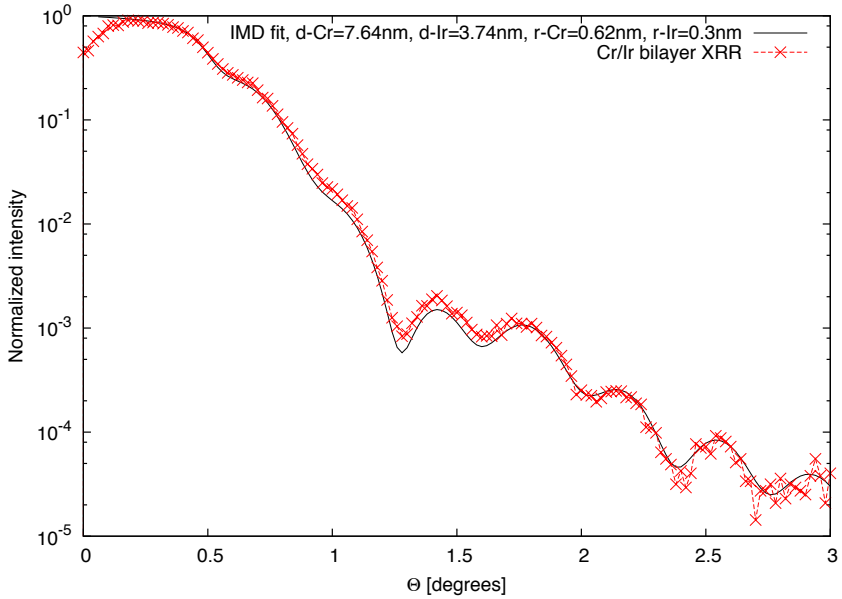

Figure 3.16: XRR measurement of a bilayer of Cr/Ir (red) along with an IMD model fitted to the data (blue).

3.3 Investigation of process improvements

3.3.1 Investigation of pulsed-DC sputtering

We investigated the use of pulsed sputtering to decrease roughness as thickness increase as described in the litterature[38, 39, 40]. In the paper by Pei et al, a sputtering cathode with a C target was supplied with -400 V and 1.5 A at 350 kHz and 50% duty cycle. The substrate was place 10 cm away from the target and supplied with -40 V at 250 kHz at 50 % duty cycle. The high frequency at the target allows for a much higher percentage of the sputtered atoms to become ionized, giving them a positive charge. At regular non-pulsed DC sputtering, only 10 % are ionized atoms, but for pulsed that increases to 60-70 %[41, 42]. The negative pulsed bias on the substrate will pull in the ionized sputtered atoms at much higher velocity than possible for DC sputtering. The higher velocity sputtered atoms gives rise to denser and more smooth films, as the momentum of the impact causes a temporary *liquification* of the immediate surrounding thin film on the nano-scale.

Attempts by Pei et al show promising results for decreasing interlayer roughness in multilayers using a high frequency pulse modulation on the power delivered to the cathode with lighter material, in their case carbon was used. For coatings for the Athena mission, it is critical to use boron carbide as the light material, as a regular C layer will be dissolved in the lift-off process that removes the lithographic resist.

We acquired the same power supply, an Advanced Energy Pinnacle Plus+ 5+5 capable of delivering two channels of 5 kW at 350 kHz. Using tungsten and boron carbide, 10 bilayer coatings were produced with the same power supply setup as mentioned in [38]. The entire rotating ring in the multilayer coating chamber at DTU Space is designed to hold a separate

bias or be grounded depending on configuration. Initial results can be seen in fig. 3.17.

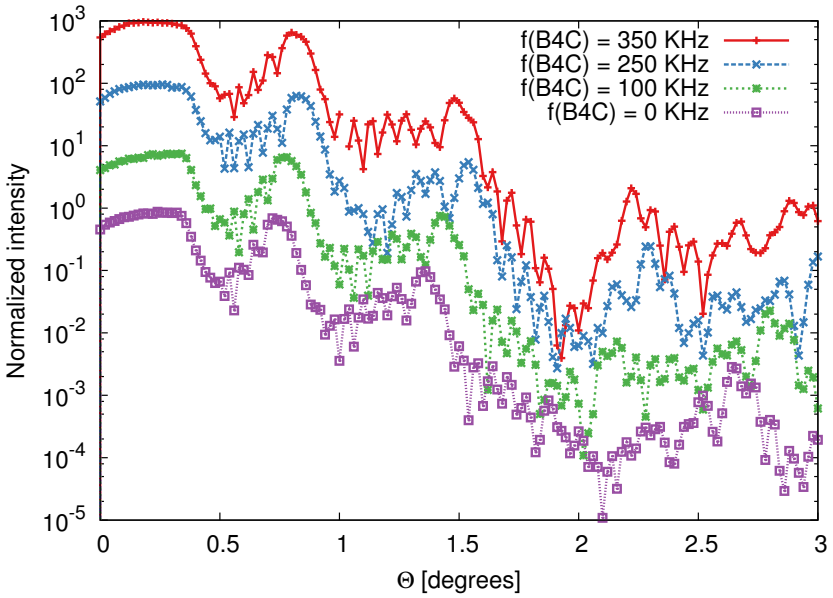

Figure 3.17: XRR measurements of four W/B_4C 10 bilayer films made with varying pulsed-DC frequency on the boron carbide cathode. Note: Measurement data shifted vertically to be easier to distinguish.

The figure show XRR measurements of 4 samples coated with 10 bilayer W/B_4C with different frequencies supplied to the boron carbide target. For a 10 bilayer coating, we expect to see clear Bragg peaks with 8 Kiessig[43] fringes between, but all samples show washed out 1st and 2nd order Bragg peaks and an indeterminate number of Kiessig fringes. Even the sample coated without a pulsed boron carbide cathode show the same behavior. In figure 3.18, the two samples coated with 350 kHz and 0 kHz in the same coating run is compared to a sample from a different run coated with regular DC sputtering showing well-defined Bragg peaks as would be expected.

Something has clearly gone wrong in the pulsed-DC coating. The new software recently installed to control the multilayer coating chamber logs the cathode output every 5 seconds and a plot of that can be seen in figure 3.19 (top) compared to a log from a regular DC coating, figure 3.19 (bottom). The figure shows clearly that the power output to the boron carbide cathode drops to zero in the middle of a rotation. The boron carbide cathode should be at 900 W output for the entire time the tungsten cathode is off.

It is not uncommon to see a cathode 'drop out' during a coating run, where the power supply is unable to sustain the plasma. In that case the power supply will increase the voltage to get the plasma to ignite again and the power output will in that period be 30-40 W. In this case the power output drops to zero, which is inconsistent with a conventional drop-out. Investigating the matter further shows that the 'arc'-protection system on the power supply goes off rapidly during a coating (see sec. 2.1.1). The arc-protection will protect the power supply from the power surge and will tell the user when it happens. The inner anode shield in the boron carbide cathode clearly shows damage from arcing in the steel and the shielding teflon strips, which looks like welding marks. The damage implies

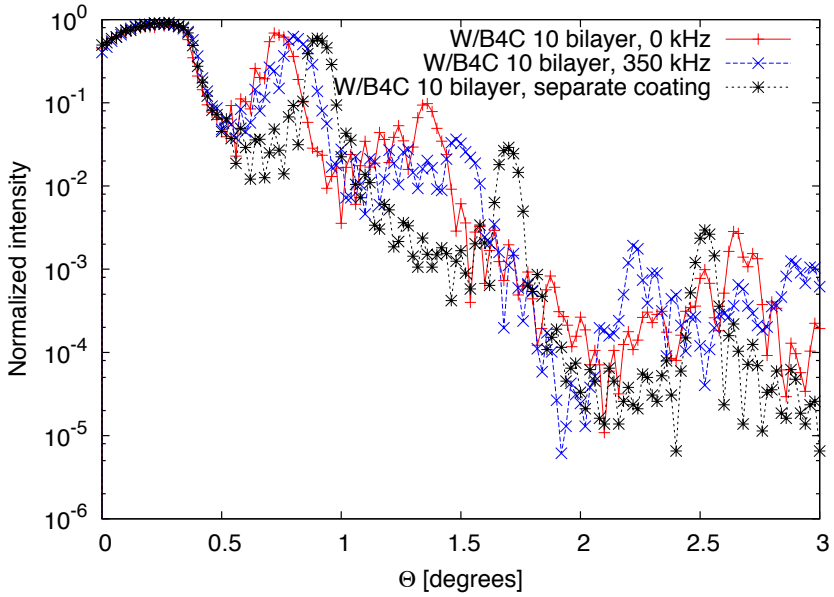

Figure 3.18: XRR measurements of three W/B_4C 10 bilayer films. Two (red and blue) made using pulsed-DC sputtering and also shown in figure 3.17. The last one (black) is made in a separate coating run without pulsed-DC sputtering, but otherwise with the same coating parameters.

that the arcs appearing are quite powerfull and might be the result of insufficient shielding or the cables between power supply and cathode being too long. As the energy is stored inductively in the cable and cables are rated by inductance per meter, a longer cable will be able to store more power to deliver to a potential arc.

It is at this moment still unclear what precisely causes the arcing. The pulsed-DC system brings many more variables into an already complicated sputtering process. In most cases arcing is caused by a buildup of insulating material on either the target or anode (chamber walls, anode shield etc.), which causes a localized charge buildup. The localized increase in charge density will eventually cause and arc between anode and cathode, and the arc-protection system on the power supply try to control it, while keeping the process running. The power supplies are however programmed to shut off power if the rate of arcing goes above a certain limit, which is likely what happened in fig. 3.19 (top).

The second attempt at using the pulsed-DC method was with chromium single layer coatings. XRR measurements of the coated samples can be seen in figure 3.20. Four samples were coated with varying frequencies applied to the chromium cathode. The measurements show clear differences in coated thickness between the frequencies used (position of Kiessig fringes does not overlap) and higher frequencies show a lower surface roughness (Kiessig fringes are less pronounced and shows a wavy pattern at the highest frequency). The XRR measurements were difficult to fit using IMD, indicating that the films are of non-uniform density. The coating done without pulsed-DC fitted to a ∼17 nm chromium thickness and the coating done with the highest frequency pulsed-DC sputtering fitted to a ∼13 nm chromium thickness. No arcing was seen when coating chromium using pulsed-DC sputtering.

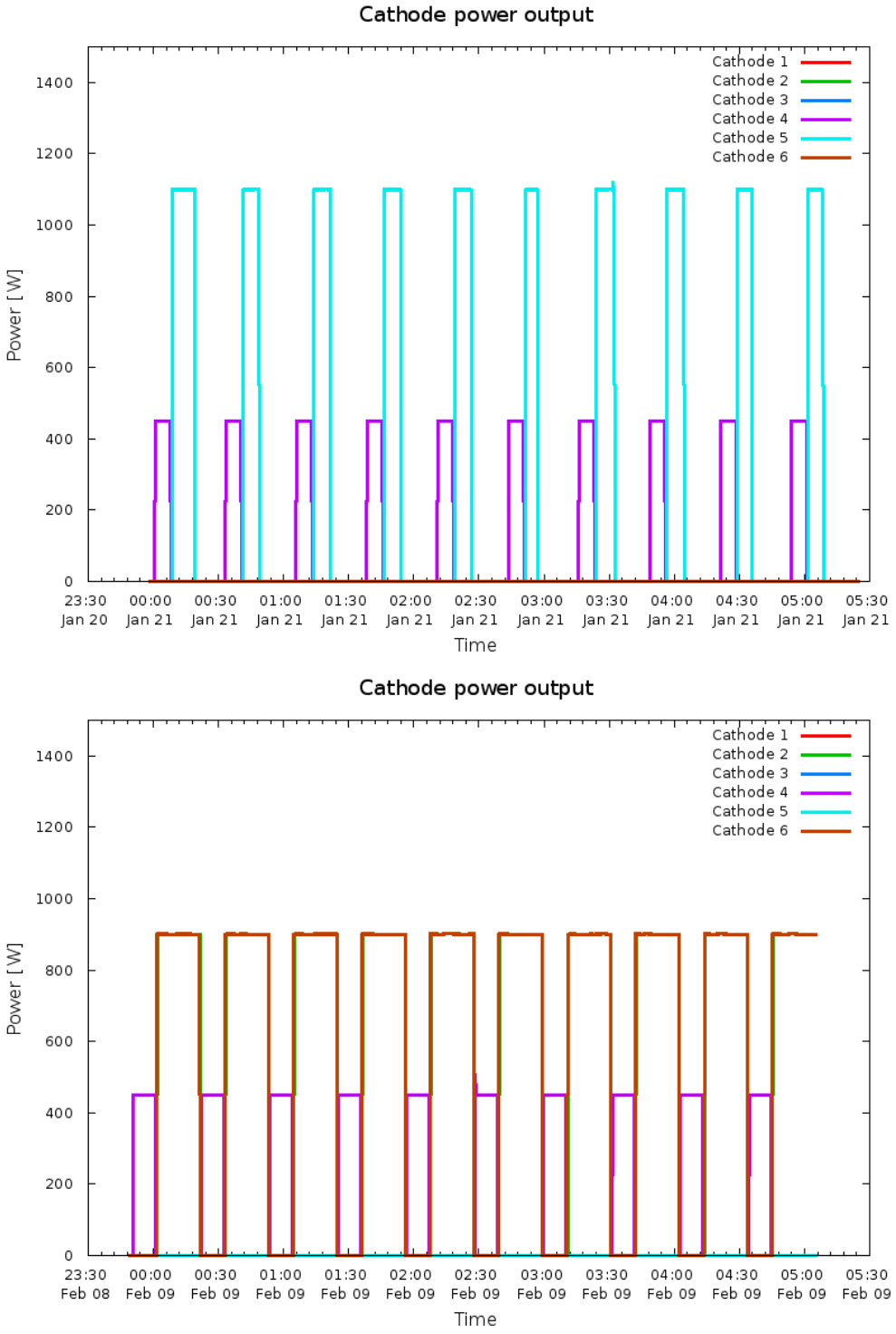

Figure 3.19: Graphs of cathode power output over time during a coating run. **Top:** A W/B_4C 10 bilayer coated using pulsed-DC sputtering on the boron carbide material. Cathode 5 turns off in the middle of the process at every layer. **Bottom:** A W/B_4C 10 bilayer coating made without pulsed-DC sputtering. Both cathodes behave as designed during this coating run.

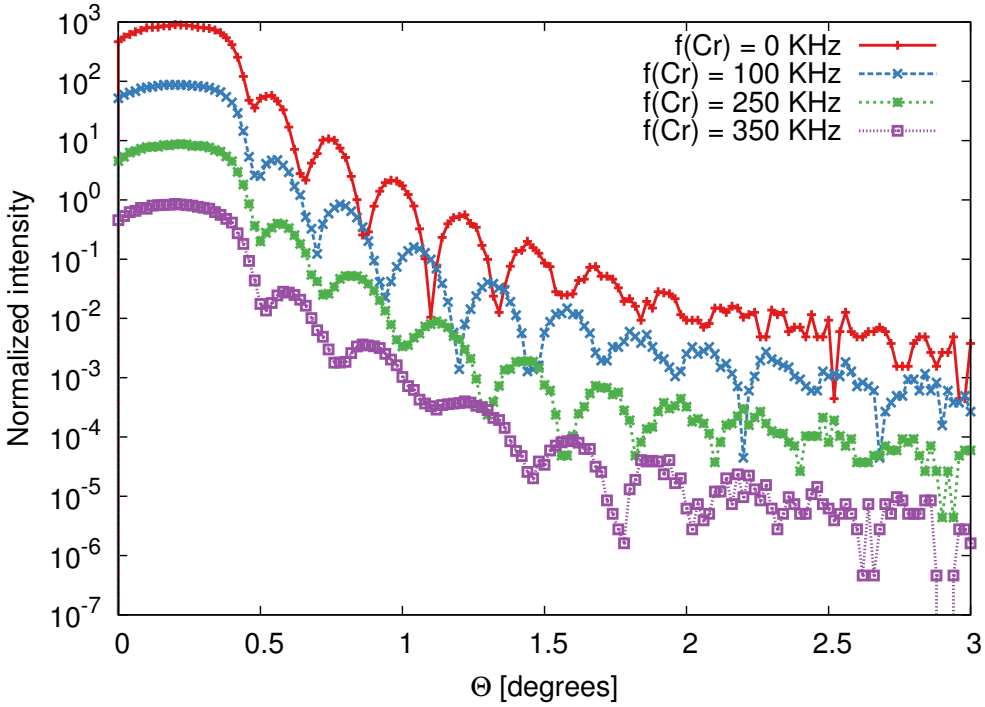

Figure 3.20: XRR measurements of four samples coated with single layers of chromium using pulsed-DC sputtering at varying frequency. Sample coated with $f = 0$ kHz (red) has a thickness of ∼17 nm. Sample coated with $f = 350$ kHz (purple) has a thickness of ∼12 nm. Note: Measurement data shifted vertically to be easier to distinguish each greph.

We believe that the investigation of pulsed-DC sputtering have concluded with no improvements in the coatings. The arcing that was seen during pulsed-DC sputtering of boron carbide, but did not show up for chromium, can have a variety of causes. First, the output power when coating boron carbide is significantly higher than for chromium (1100 W compared to 450 W). The higher power puts higher demand on electrical shielding as well as the cable length between power supply and cathode. Second, there are fundamental differences in the two materials. The chromium is a well conducting and hard metal, whereas boron carbide is not very well conducting and brittle. A very good contact is required between cathode and sputter material, but since the boron carbide is very stiff and not as malleable as metal, the target can easily crack which will give rise to areas of non-contact.

In conclusion, the whole process is not well understood, but has potential as seen in the literature. A significant effort was applied to reproduce the results from Pei et al[38]. The major difference was the use of boron carbide instead of pure carbon, which might explain the lack of positive results. Boron carbide being a compound material of two elements with different atomic weight and electron configuration might behave differently under the application of a large electric field. The purpose was to ionize sputtered atoms, then reverse the electric field which would drag them into the substrate with a higher kinetic energy, thus creating a denser film with smoother surface. Using a compound material has likely introduced unknown variables to the process.

3.3.2 Reactive sputtering of W/B_4C with nitrogen gas

Improving interlayer roughness of multilayer coatings using nitrogen reactive deposition has been shown before[44, 45], specifically for W/B_4C films. For this project, coatings of 10 bilayer W/B_4C were produced using nitrogen reactive sputter deposition and compared to similar coatings made without nitrogen gas. XRR measurements of the results and comparison can be seen in figure 3.21. The right figure show coatings with a d-spacing of ∼3.5 nm, and the left coatings with d-spacings of ∼5.0 nm. The right figure show a horizontal offset in the XRR measurement between the two coatings, contributed by an offset in the calibration. The left figure show a similar offset, but also a significant change in Kiessig fringe intensity between the 2nd and 3rd Bragg peak. The 3rd Bragg peak is also less pronounced for the reactively sputtered film than the non-reactively sputtered. The results indicate that the reactive sputtering does not improve the interface roughness, but rather increases interlayer roughness.

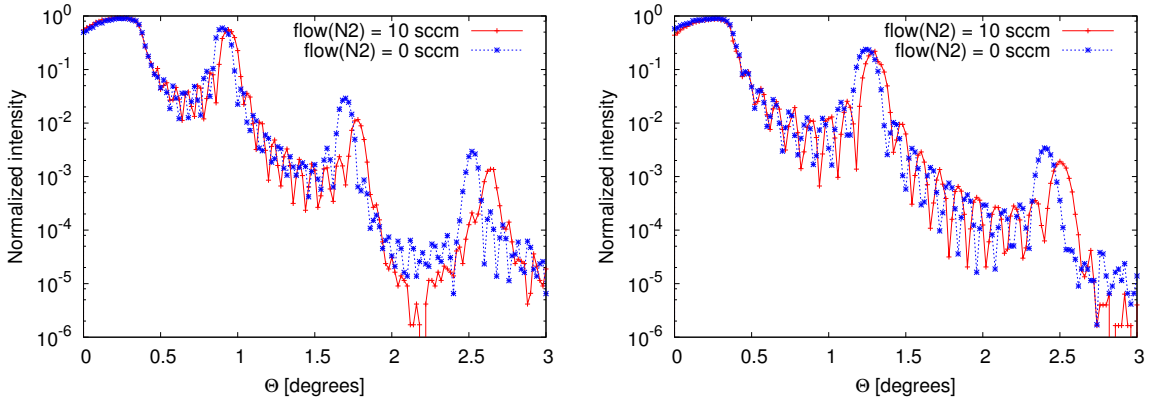

Figure 3.21: XRR measurements of 10 bilayer W/B_4C coatings made with and without nitrogen reactive sputtering (10 % N_2, 90 % Ar). **Left:** Coatings with a d-spacing of ∼5 **Right:** Coatings with a d-spacing of ∼3.5 nm. nm.

It was later found out from samples stored over a longer period, that the coatings will visibly change over time if coated with nitrogen reactive sputtering. A sample with discoloration can be seen in figure 3.22 (picture taken July 2014). The sample is a W/B_4C 10 bilayer calibration coating with a d-spacing of ∼5 nm. It was coated in February 2012 using 10 % N_2 with 90 % Ar at a total pressure of 2.9 mTorr.

Investigation into the literature gives a possible explanation. Boron carbide coatings react to humidity, but for BN coatings the effect is even more pronounced. The coating will absorb water molecules from the air, which diffuses through the coating and can eventually make the film peel off[46]. When boron carbide coatings are sputtered with nitrogen present, the nitrogen atoms become part of the film and will form B-N bonds. That would make all boron carbide films produced with nitrogen reactive sputtering deteriorate at ambient humidity. To test the hypothesis, a number of samples were produced with and without reactive sputtering, measured with XRR and subsequently placed in a desiccator at ∼20% humidity.

The results can be seen in figure 3.23. The upper row are thick (∼5.0 nm) and thin (∼3.5

Figure 3.22: Picture of Si wafer sample coated with 10 bilayers of W/B_4C using nitrogen reactive sputtering. Sample was coated in February 2012, picture taken July 2014. The surface over time turned a yellow/brown colour with the edges black/blue. Top and bottom are marks from the clips holding the sample in place during coating. The clear uncoated surface is visible in those spots.

nm) samples of 10 bilayer W/B_4C coated with 10 SCCM nitrogen gas flow ($\sim$10% N_2). Middle row are samples with the same type and thickness of coating, but without nitrogen gas present. Bottom row are also coated without nitrogen but placed at ambient humidity ($\sim$50%) outside the desiccator. The bottom row are also only stored for 3 months. The reactively sputtered coatings in the upper row show little change from Feb. 4th to June 28th, $\sim$5 months. What is interesting is the center row that show some interfacial changes in the film, especially for the thicker sample (left figure). Comparing to the bottom row, the thicker sample does not show the same changes over the 3 month period, but the thinner sample show significant change. The critical angle has shifted or washed out, the Bragg peak has widened and lowered in intensity. The sample also show visible discoloration, which is something that was not expected of a coating made without nitrogen reactive sputtering.

3.4 Findings from long term storage of coated samples

All samples coated at DTU Space are stored indefinitely for possible later investigation. The calibration samples of each material type for the Athena coatings are especially suitable for a long term investigation since the XRR measurement results of these samples have distinct features. In figure 3.24 the results of XRR measurements of W/B_4C calibration samples are shown immediately after coating and again up to 18 months later. The samples are coated without nitrogen gas and using the standard Ar pressure of 2.9 mTorr.

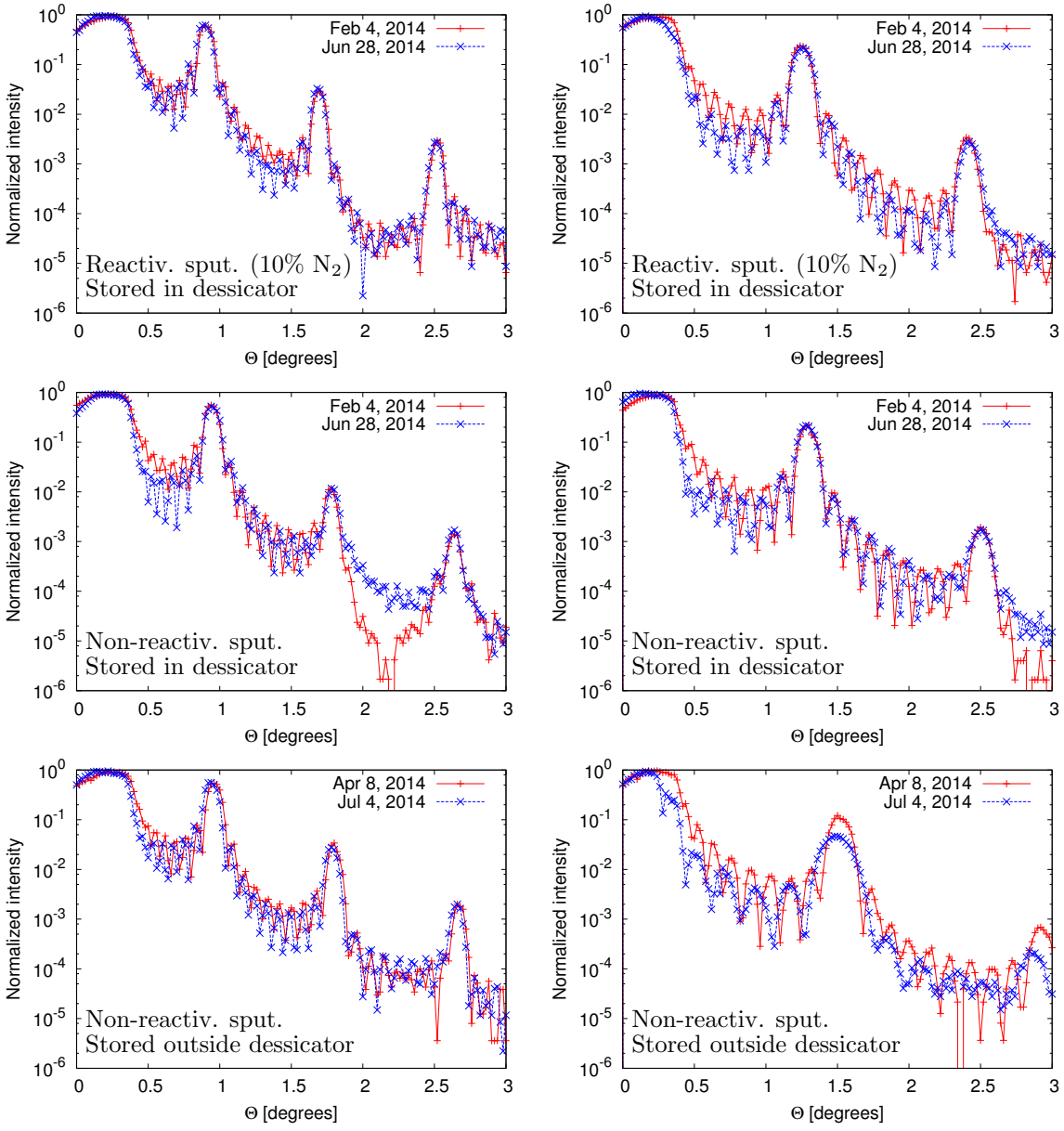

Figure 3.23: XRR measurements of samples coated with 10 bilayer W/B_4C films measured after coating and at a later time. Top and middle row samples were stored in a desiccator with ∼20 % humidity. Bottom row samples were stored at ambient humidity (∼50 %). **Top row** Samples coated with nitrogen reactive sputtering (10 % N_2, 90 % Ar) and stored in desiccator, d-spacings of ∼5 nm (left) and ∼3.5 nm (right). **Center row** Samples coated with non-reactive sputtering and stored in desiccator, d-spacings of ∼5 nm (left) and ∼3.5 nm (right). **Bottom row** Samples coated with non-reactive sputtering and stored outside desiccator, d-spacings of ∼5 nm (left) and ∼3 nm (right)

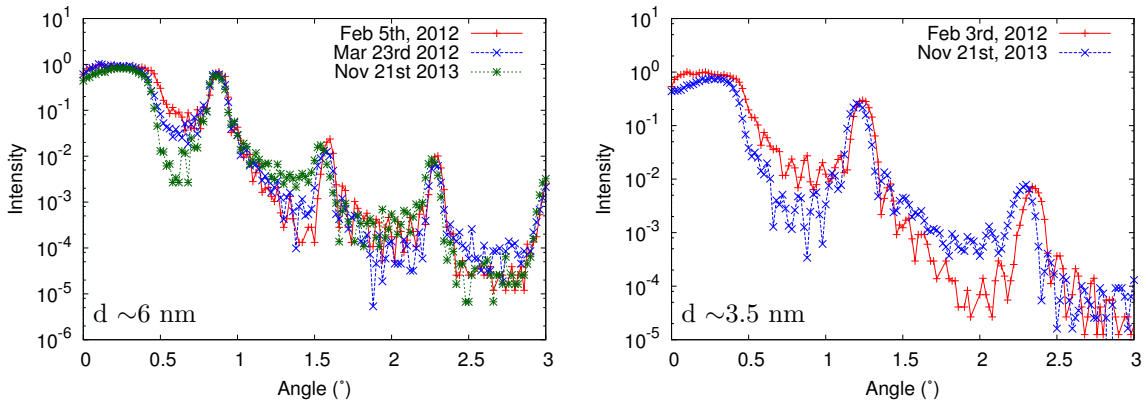

Figure 3.24: XRR measurements of coatings stored for 2-3 years at ambient conditions (outside desiccator). 10 bilayer W/B_4C with d-spacings of ~6 nm (left) and ~3.5 nm (right).

The W/B_4C multilayers show significant change after less than two months. The thicker sample (left) have a shifted critical angle, corresponding to a change in Γ in the multilayer. The thinner film (right) also show a change in critical angle, although less pronounced. The change in critical angle indicate either a change in Γ in the multilayer or a change in density of either boron or tungsten.

Changes in Γ would be a diffusion process from one material to the other, which might be the case. The van der Waals radius of boron atoms is very small, so it is possible that they could diffuse in between the larger tungsten atoms. Alternatively, oxygen atoms could be present in the boron carbide film that would over time diffuse into the tungsten layer[47], forming WO_x. No change in Bragg peak intensity is seen however, except for the very thinnest coatings of 3–3.5 nm d-spacing. A diffusion of light boron or oxygen atoms into tungsten would decrease Bragg peak reflectivity, as the interface between tungsten and boron carbide would be less sharp caused by lowering of electron density of the tungsten closest to the interface. An explanation could be that all the tungsten films in the multilayer have been saturated by oxygen or boron atoms in the first month, which would explain that the critical angle changes in figure 3.24(left) after a month, but is unchanged six months later.

3.4.1 Long term storage investigation of Pt/B_4C and Ir/B_4C

The discovery of changes in W/B_4C coatings over time necessitated an investigation of the two other material combinations, Pt/B_4C and Ir/B_4C. XRR measurements of coated calibration samples measured immediately after coating and after up to two years later can be seen in figure 3.25. All the samples are coated without nitrogen gas and using the standard Ar pressure of 2.9 mTorr.

In the upper row are shown 10 bilayer Pt/B_4C multilayers, and bottom row show Ir/B_4C multilayer (left) and Ir/B_4C multilayer with chromium sublayer (right).

The Pt/B_4C multilayers show significant change over time. The thicker film (left) show a

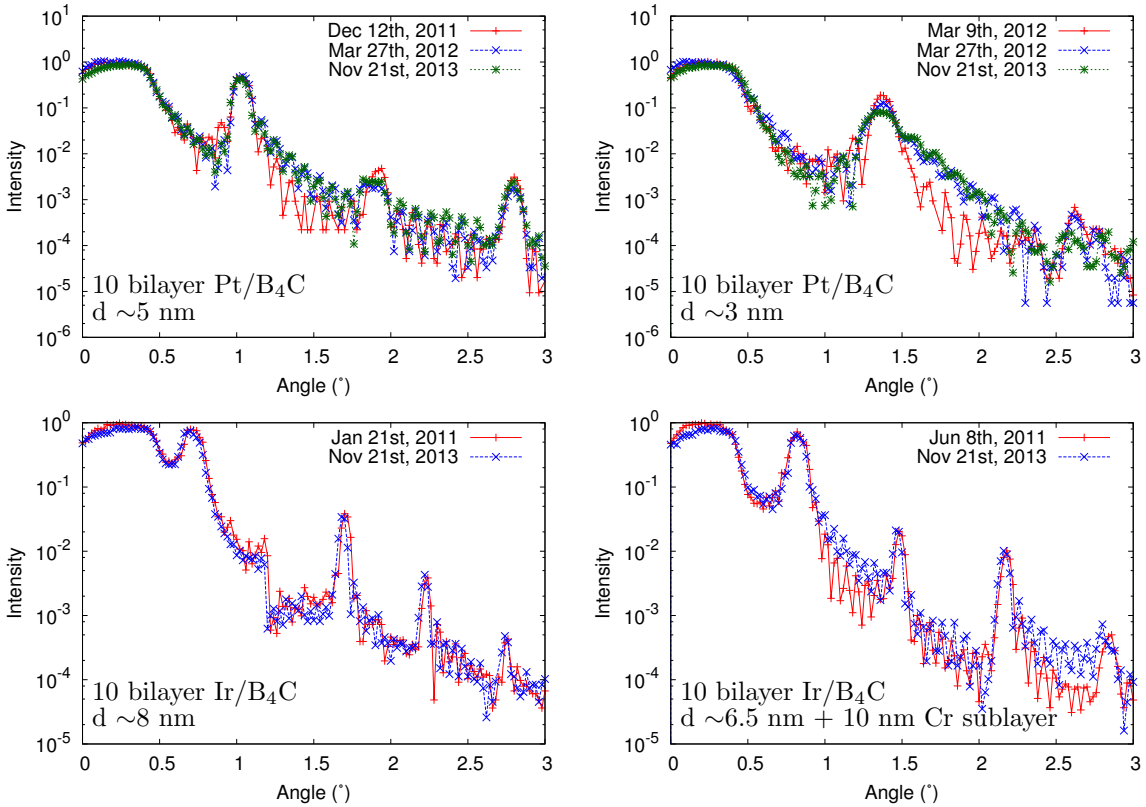

Figure 3.25: XRR measurements of coatings stored for 2-3 years at ambient conditions (outside desiccator). **Top row** 10 bilayer Pt/B_4C with d-spacings of ∼5 nm (left) and ∼3 nm (right). **Bottom row** 10 bilayer Ir/B_4C with d-spacings of ∼8 nm (left) and 10 bilayer Ir/B_4C with d-spacings of ∼6.5 nm and a 10 nm chromium sublayer (right).

rise in Kiessig fringe intensity between 1st and 2nd Bragg peak as well as a flattening of the 2nd Bragg peak. These effects show up already after ∼4 months. The thinner Pt/B_4C film (left) show even more deterioration, even after only 18 days. The 1st Bragg peak have widened and have grown a significant shoulder at higher angles. No shifts in Bragg peaks or critical angle are seen, indicating that the the thicknesses of both platinum and boron carbide stays constant and the overall density for either material is unchanged. A diffusion is the most likely explanation here, as the decrease in sharpness at the interface causes less-defined Bragg peaks. Especially for the thinnest layer (figure 3.25 (top right)), where the Bragg peak broadening could be caused by density gradients in platinum caused by diffusion of boron or carbon.

Ir/B_4C multilayers in the bottom row show very little change even after 2-2.5 years. The sample with chromium sublayer (right) shows some change in the Kiessig fringe intensity.

These results indicate serious problems in using boron carbide films with platinum (and tunsten as discussed in section 3.4). However, the baseline Athena coating of an Ir/B_4C bilayer and the alternative Ir/B_4C multilayer will according to these results be stable over longer periods of time.

3.5 Upscaled production

For the Athena mission, the coating of the mirror substrates will be a large undertaking as 140,030 silicon pore optic (SPO) substrates will need a coating of between two and twenty layers.

Every piece will have to be transported from the SPO substrate fabrication facility (SFF) to a new dedicated coating facility, thoroughly cleaned, coated in specially designed chambers and then transported to the stacking facility. After stacking into mirror modules (MM), each MM will be measured at one of three dedicated beam lines at the BESSY II synchrotron in Berlin.

In this paper, an estimate of cost and timeframe of the coating and coating qualification of all SPO substrates for the Athena mission is given.

3.5.1 Timeline and cost of procurement and setup of coating facility

Cleaning and coating of SPO substrates will require as a minimum an ISO 7 clean room to avoid dust particles. Dust on the substrates before coating will result in small holes in the coating, which will reduce the effective area. There are two possibilities for the location of the coating facility which is discussed in this paper. Either the facility is located in the

same building or adjacent building as the stacking facility or the coating facility is placed further away, i.e. another country within Europe.

Moving substrates in and out of clean rooms and transporting them over larger distances has drawbacks and extra costs associated. But locating the two facilities separately can reduce costs as it will be easier cheaper to find two smaller clean rooms to re-purpose into production facilities. Building and setting up clean rooms of a sufficient size for both facilities will take several years and come with a significant cost, but if it is possible to re-purpose existing laboratories that cost can be reduced.

The first part of the clean room should be for opening shipments from the SFF and cleaning each substrate. As the substrates are produced in a clean room at the SFF, it is assumed that they will at maximum need to be cleaned with an air gun with dry nitrogen. After being cleaned, each substrate is mounted onto a substrate holder that will be inserted into a coating chamber for coating. When the coating is done, the substrate holder is taken out of the chamber and the substrates are ready to go into the stacking facility.

Clean rooms can be build inside existing larger storage areas or cleaner production facilities. The approximate timeline for the setup of the entire facility is as follows:

9 years before launch:

- Planning begins for the construction of a shared cleanroom facility.
- Planning begins for coating chambers.

7-8 years before launch:

- Construction of facility is carried out.
- Produced coating chambers are installed and qualifications begun.

6 years before launch (CDR):

- Coating capabilities ready.

The cost of building and preparing the coating facility will differ between a shared facility and separated facilities, but the coating chambers will have a similar configuration.

3.5.2 Coating chambers

The telescope of Athena consists of 19 rings of mirror modules, each with two stacks of 68 coated SPO substrates, resulting in 140,030 SPO substrates in total. Considering the coating chamber design used at DTU Space, a maximum of 100 plates can be coated per day in an 8 hour workday. In a year of 200 workdays, 20,000 substrates can be coated. Using six chambers, 120,000 substrates can be coated per year, within the two year time frame a total of 240,000 substrates can be coated. A minimum of 1.5 times the needed 140,000 coated substrates is considered the baseline ($\sim$210,000), as we account for damaged

plates, bad coatings etc. That leaves an acceptable down time of ∼2 months throughout the project.

Using chambers of same design as DTU Space will give a cost of around 1M € per chamber. Those chambers have the drawback of a long pump down time after having the chamber opened to change samples. The advantage of coating SPO substrates compared to e.g. NuSTAR glass is that the SPO substrates are flat and only ∼1 mm thin.

If a new chamber design is considered, it would be advantageous to pursue a design similar to what is used in the semiconductor industry. Here an entire wafer are given a number of different coatings and automatically moved from one cathode to another using a robotic arm. As those wafers can have a thickness of up to 3 mm, we propose to use a substrate holder shaped like a wafer 3 mm thick with a diameter of 300 mm. Recessions in the substrate holder can accommodate SPO substrate and no clips will be needed to hold substrates in place, since the wafer will at all times be horizontal. A chamber of that design will not need pump down time between each batch of substrates, since wafers will be inserted into the central vacuum chamber through a narrow slit directly from a clean magazine in atmospheric pressure. Every coating cathode is also in a separate chamber and can be accessed without venting the entire machine. Custom made machines like seen in figure 3.26 are priced at ∼2M €.

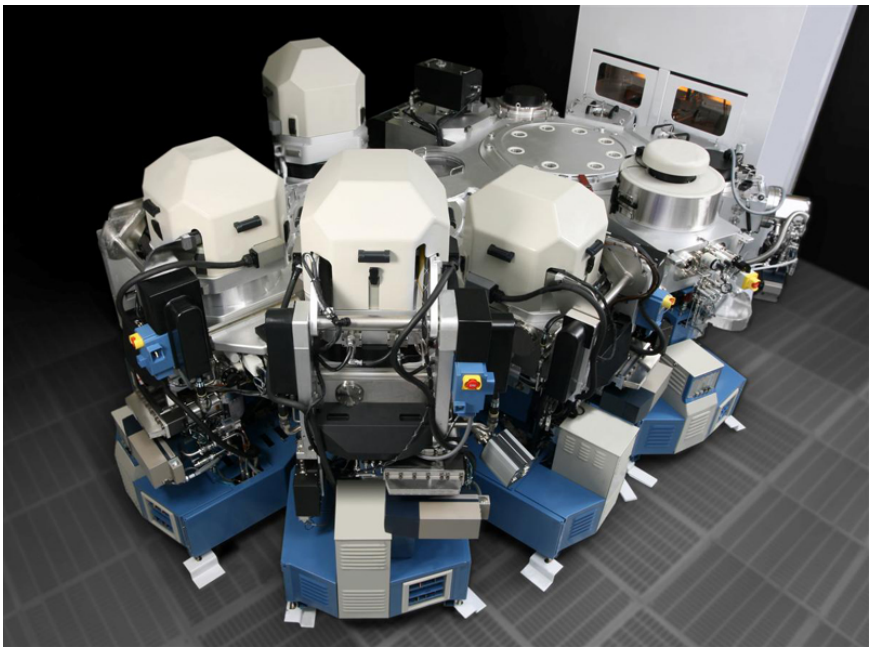

Figure 3.26: Multi-chamber deposition machine from Applied Materials. Each white dome is a sputtering chamber with a circular cathode depositing downwards. Wafers are moved between chambers using a robotic arm placed in the central vacuum chamber. *Source: www.appliedmaterials.com*

A significant increase in production rates can be achieved using machines like this. It also gives a cleaner environment for samples, since the machine itself can stay closed for longer periods of time. Higher production rates means that only three or four chambers are needed to complete the coating of 210,000 SPO substrates in two years.

3.5.3 Shared facility

Since both the coating facility and stacking facility needs a clean room, these can be combined or connected in a shared facility. If the chamber design from DTU Space is used, a separate clean room will be needed to accommodate these chambers as they can give off dust flakes of material every time they are opened. If instead a multi-chamber coating system is used as described in section 3.5.2, the coating machinery can be in a separate clean room against the wall into the stacking facility. That way wafer cassettes full of wafer-shaped SPO substrate holders can be inserted and retrieved from the stacking facility clean room.

For a shared facility with multi-chamber coating systems as described in section 3.5.2, we propose the following facility setup:

- Common class 10,000 clean room for mounting SPO substrates on wafer-shaped sample holders. The same room will be used for fast X-ray system for pre- and post coating measurements.
- Access to insertion port of multi-chamber coating system from the common clean room. Wafer cassettes are mounted directly to accessible part of the machine.
- The back end of the coating chambers are in a separate room, so targets can be changed without giving off dust near the substrates.
- In connection to the common clean room is a separate class 100 - 10,000 clean room with stacking robots. The robots can be in a separate ventilated tent inside the clean room to decrease particle dust. Mirror modules will be sealed here and moved outside the clean rooms for packing and shipping to BESSY II.

3.5.4 Separated facilites

If the facilities are separated, a large effort will be required to keep substrates clean when packing/unpacking for transport. The substrates will be send from the SFF in batches of 3,000 and double or triple sealed, so the package can be opened partly when inside a moderately clean room and opened completely in the main class 10,000 clean room. The following setup of clean rooms is proposed.

- Two separate class 10,000 clean rooms, one for substrate handling and one for coating chambers. Alternatively, one larger clean room parted by a clear plastic curtain.
- Substrate handling clean room will also be used for the fast X-ray system for pre- and post coating measurements.
- Coated samples will be packed and double sealed inside the clean room before being shipped to the stacking facility.

3.5.5 Resist deposition and removal at alternative facility

One of the processes done at the SFF to the substrates before sending them to the coating facility will be the lithographic process of resist deposition. It requires a semiconductor grade facility to apply the resist using spray-on and afterwards removing stripes by a UV radiation process.

The process can, instead of at the SFF, be done either at the coating facility by including the proper equipment or at an external facility. DTU Danchip is the Danish National Center for Micro- Nanofabrication, which runs a class 10 clean room with equipment capable of depositing the resist and UV curing the SPO substrates.

The removal of the resist after coating can be done at the stacking facility, but can also be done at the coating facility if these are separated. By doing the resist removal at the coating facility, a visual inspection can be done of the substrate before being transported to the stacking facility. If the process damages the coating, the problem can be located and new coated substrates can be produced quickly.

3.5.6 Cost for setting up

To prepare the lab before the coating campaign starts, the coating chambers will need to be installed and configured. An extensive campaign with scientific personnel is needed to ensure the system's capability to produce coatings of sufficient quality. We estimate 12-24 months to qualify the coating chambers for the Athena coating campaign and will need approximately four scientific personnel and two technicians.

The coating qualification equipment described in section 3.5.9 will be needed to qualify the coating chambers.

Equipment	Approx. price
6 x Coating chambers of DTU design	6 x 1,000,000 €
or:	
4 x Multi-chamber coating systems	4 x 2,000,000 €
Personnel for setup	980,000 €

3.5.7 Timeline and cost for production of Athena coatings

SPO substrates are fabricated at the SFF and should be shipped to the coating facility weekly in shipments of 3,000 substrates. 600 substrates are daily mounted on wafer shaped sample holders after they have been measured using the fast X-ray system. The substrates are coated in one of the coating chambers and subsequently taken out to have resist removed and be measured again using the fast X-ray system.

Cost drivers during production are sputtering targets and personnel. The final cost is dependent on which material combination is used for coating. The differences can be seen below.

Material combination	High Z thickness (nm)	Approximate price / mm^3 (High Z)	Low Z thickness (nm)	Approximate price / mm^3 (Low Z)
$Cr/Ir/B_4C$	10	10.9 €	8	0.26 €
Pt/B_4C	∼16	10.5 €	∼22	0.26 €
W/B_4C	∼16	0.73 €	∼22	0.26 €

The approximate cost is calculated based on a 10% efficiency of the sputtering cathodes, meaning 10% of the target material ends on a substrate. For a single layer of 10 nm on all the substrates of Athena, the volume of material needed will be approximately 10 cm^3 = 10,000 mm^3. From that, the total target cost can be estimated.

Material combination	Type of coating	Approx. cost	Approx cost incl. 30 % target usability
$Cr/Ir/B_4C$	Tri-layer	114,000 €	380,000 €
Pt/B_4C	Graded-d multilayer	174,000 €	580,000 €
W/B_4C	Graded-d multilayer	17,400 €	58,000 €

Only 30% of the target can be used before it has to be replaced, so a factor of 3-4 should be applied to these cost estimates. The leftover targets of precious metals, platinum and iridium, can be sold back at market value, which can reduce the total costs of precious metal consumption by up to ∼50 %.

For a Pt/B_4C graded-d multilayer, the total thickness of Pt is 16 nm in average and 22 nm of boron carbide. Thus, $1.6 \cdot 10000$ mm^3 of Pt is needed at a price of 10.5 € per mm^3 at 90 % coating loss, combined with $2.2 \cdot 10000$ mm^3 of boron carbide at 0.26 € per mm^3 gives a total cost of 174,000 €.

3.5.8 Personnel

During the two year coating campaign, 600 substrates will be handled daily. Procedures to be done daily include:

- Unpacking substrates.
- Measuring using fast X-ray system.
- Mounting substrates on sample holders.
- Load sample holders in coating chamber.
- Running coating equipment.

- Unloading sample holders.
- Remeasuring using fast X-ray system
- Repacking samples for transport to stacking facility.

Additionally, the coating chambers will require new targets to be installed on a weekly basis. We estimate 4-5 technicians are needed in addition to 3-4 scientific personnel to run the coating production.

For five technicians four scientists, a two year coating campaign will cost ∼2,800,000 €.

3.5.9 Coating QA during production

We envision a significant coating qualification campaign for the Athena mission. We propose a fast automated 8 keV X-ray setup, that can measure every plate before and after coating. The plan is to make reflectivity scan of ca 50 % of the pores. Each measurement is an angular scan at a fixed 8 keV energy and at an angular range of 0°to ∼ 1.5° will determine micro roughness to an accuracy of +/- 0.02 nm. It till require automatic alignment to an accuracy of +/- 0.01°. Measurements for each plate should be conducted in less than 5 minutes and each scan should be automatically fitted, with the data logging and plotting part of the facility. The foot print of the beam should cover more than 10 % of each pore.

The total database of reflectivity measurements can be used when building the final optical response model for Athena. During the campaign it will be required to measure 1,200 SPO substrates per day, so the system should be capable of measuring each substrate in a batch automatically.

Every chamber needs to be calibrated twice a week to ensure a precise layer thickness. This will require samples to be coated with constant-d multilayers, which will be measured using a separate 8 keV X-ray reflectivity (XRR) setup at the facility.

In every coating run, a piece of Si wafer (∼2 x 8 cm^2) will be included along with SPO substrates as *witness samples*. The purpose of the witness samples is to have a representative sample of every coating run for more precise measurements later or for some yet unknown test that needs to be done on that specific coating. These witness samples will be measured using the 8 keV XRR setup to ensure proper layer thickness interfacial roughness. In addition, 5x70 mm wafer pieces are also coated measured for stress using a stylus measurement tool. One or two times a week, a coated SPO substrate will be taken out to check for adhesion and visual QA in a microscope. If contamination is suspected, an AFM analysis will be carried out, if necessary externally.

Measuring samples at the energies visible by Athena can help build the final optics model. We propose this optional addition: A single coated substrate per day will be selected for reflectivity scatter measurements at the BESSY II synchrotron at PTB Berlin. 25 substrates per month can be measured using X-ray reflectivity energy scans at 4 to 10 keV at BESSY

II within 2-3 days. A few more days per month will be needed to measure scattering from select substrates.

Below are approximate prices for equipment needed.

Equipment	Approx. price
Fast automated 8 keV X-ray setup	1,000,000 €
Separate 8 keV X-ray setup	500,000 €
Stylus stress measurement setup	30,000 €

3.5.10 Timetable and cost

The timetable is independent on whether the coating facility is shared with the stacking facility or separate.

T - 9 years	Planning begins for the construction of a shared clean room. Planning begins for coating chambers.
T - 8 years	Construction of facility is carried out. Produced coating chambers are installed and qualifications begin.
T - 7 years	Continuation of coating chamber qualifications.
T - 6 years	Coating chamber qualifications complete. Coating capabilities ready.

The timetable gives the possibility of starting the coating campaign six years before launch. The coating campaign is set for two years including delays will have the optic ready four years before launch. The four year window between optic readiness and launch is specified in the ESA timetable.

Total cost for a shared facility is calculated below. For a separate facility, transport costs of substrates will have to be included, estimated at minimum 100,000 €. Substituting six DTU design coating chambers with four more advanced multi-chamber systems will increase the cost of coating chambers from 6 mio. €to 8 mio. €, but the possible improvement in cleanliness and uptime will in our opinion make up for the difference.

3.6 Athena discussion and conclusion

The Athena mission is set to launch in 2028 and it is clear that many things has to fall into place to meet the deadline, especially the large production effort that has to be realised. From the results in described in this chapter, the choice of Ir/B_4C material combination

Expense	Approx. price
6 x Coating chambers of DTU design	6 x 1,000,000 €
or:	
4 x Multi-chamber coating systems	4 x 2,000,000 €
Fast automated 8 keV X-ray setup	1,000,000 €
Separate 8 keV X-ray setup	500,000 €
Stylus stress measurement setup	30,000 €
Sputtering targets	600,000 €
Personnel during setup	2,000,000 €
Personnel during production	3,000,000 €
Total	$\leq$ 15,130,000 €

seems to be the only possibility to meet the target of 2 m^2 effective area at 1 keV. An alternative material combination that could work with the lithographic process described in section 3.1.3 is W/Si, but the higher electron density of Si would seriously impact the effective area at lower energies and so would the absorption edge of Si at $\sim$1.8 keV.

Selecting boron carbide as the low-Z material in the reflective coating is an obvious choice for an X-ray telescope with sensitivity down to 0.1 keV, but as this chapter shows, there are serious problems with boron carbide in combination with Pt or W. Reflective W/B_4C multilayer coatings for X-ray purposes has been reported in the litterature[48, 49], but none has shown the long term effect ambient conditions can have on these coating. Some report on the stability of W/B_4C multilayers after heat treatment to 500°C[50] or 800°C[51], but both were done under vacuum ($< 10^{-4}$ Torr).

Extensive investigations in the literature has shown no reports on the deposition of a Pt/B_4C multilayer combination, so this chapter provides the first measurements of the coating and long term stability. The multilayers were found to have a high interlayer roughness by XRR immediately after coating, so it was decided to use a single Pt/B_4C bilayer as a backup solution to the Ir/B_4C baseline because of the lower stress. However, the long term stability tests revealed what seems to be a large amount of diffusion at the Pt/B_4C interface, leading to a break-down of the multilayer structure. Even in a single bilayer film the high amount of diffusion will significantly increase interlayer roughness over time.

The changes in both Pt/B_4C and W/B_4C over time seems to be only under ambient humidity, i.e. not an issue after launch; but keeping every single coated SPO substrate out of humidity for 4–6 years during production and until launch is not quite realistic. The end result is a complete disqualification of both Pt/B_4C and W/B_4C for Athena in favor of Ir/B_4C single bilayer or multilayers and with W/Si as a backup solution, although without meeting science requirements of 2 m^2 effective area at 1 keV.

The qualification tests of Ir/B_4C coatings on SPO substrates described in section 3.2.1 showed great promise in the stability of the material combination even under high humidity and temperature. Later tests were done to see how high a temperature the coatings can withstand before breaking down, and at 250°C, a change was seen in structure in XRR

measurements. The high stress of the materials that was seen early in the investigations can be mitigated using a chromium underlayer, and the high surface roughness of chromium can be mitigated by a unique smoothening effect of iridium. Even without a chromium underlayer, it seems that the high stress has no consequence on the stability of the coatings; and as the SPO substrates are extremely stiff, no bending is likely to occur as a result of film stress.

The choice between single bilayer or multilayer Ir/B_4C coatings for Athena is a question of cost. Applying a single bilayer is the inexpensive solution, as it puts the least requirements on production facilities; every SPO substrate will get the same coating. Multilayers of 5–10 bilayers will require more time per sample to apply as well as more complicated coating chambers. One could imagine a linear coating system with one iridium cathode and one or two boron carbide cathodes, SPO samples would enter in one end of the system and exit in the other end, thereby finishing a baseline single bilayer coating with just a linear movement through the chamber. A similar setup for multilayer coatings would require a system with up to 20 cathodes in a row of interchanging iridium and boron carbide, a massive system with multiple points of failure. An alternative approach is the multi-chamber solution as described in section 3.5.2, which is the recommended solution reported to ESA by DTU Space. The multi-chamber coating facility takes advantage of the SPO technology heritage from the semi-conductor industry, primary advantage being the completely flat geometry of SPO substrates before stacking.

The past decades of rapid growth and technological progress in the semi-conductor industry will definitely be a major reason for making a telescope with more than 140,000 mirror substrates possible. A similar sized mission with individually slumped glass substrates as in the NuSTAR mission will require a substantial man-power effort as each step from flat glass to curved, cleaned and coated glass mirrors are labor-intensive and almost impossible to automate. The SPO technology has drawbacks, such as limits on material combinations and a larger minimum inner radius compared to slumped glass, but the low substrate figure error, mass production capability, and rigidity of mirror modules gives SPO a substantial advantage in large X-ray missions.

Chapter 4

X-ray optic for the CAST experiment

After the launch of NuSTAR, the X-ray optics group at DTU Space was invited to participate in the creation of an X-ray optic for the CERN Axion Solar Telescope (CAST) [52, 53]. CAST is an experiment at CERN that looks for the hypothetical axion particle[54, 55, 56, 57] which is a solution to the charge-parity (CP) problem of the standard model in particle physics[58]. If the axion exist, it constitutes some or all of the Dark Matter in the universe[59, 60]. It was decided that the optics technology from NuSTAR[12, 10, 61, 62, 9] could be leveraged and therefore use spare glass to make an inexpensive and relatively simple X-ray optic.

The optic was designed between 2012 and 2014. Production, assembly, installation and alignment with CAST was done during summer 2014 in cooperation with University of Zaragoza (UoZ) in Spain and Lawrence Livermore National Lab (LLNL) in the US. In this chapter the reader will find a description of the whole process from start to finish.

My part of the work was to design the optic geometry and coating as well as produce the coated substrates and participate in the installation. LLNL designed the vacuum vessel and alignment procedure and UoZ designed detector and the X-ray source assembly.

A complete software package was developed that could calculate the geometry of the optic given a focal length and substrate specifications. The software then optimises the coating for a range of material combinations with respect to energy range and axion spectrum by incorporating IMD. I chose to make the software in Python because of the huge amount of documentation and specialised packages available. To interface with IMD, a package called Pidly was used to communicate with IDL, which could spawn an IMD session. The principle is described in section 4.6.1

4.1 The CAST instrument

The axion is a theoretical ultra-light particle formed from the interaction of a photon with an electromagnetic field. The effect is called the Primakoff conversion, which is a conversion of

plasma photons into axions in the Coulomb field of charged particles. Other possible sources of axions are the ABC processes: Axion recombination, Brehmstrahlung and Compton[63]. A primary source of the particle would be from inside stars where high densities of photons and charged particles are found in the plasma. From Earth the best nearby source will of course be the Sun. The axion is weakly interacting so in order to detect it, CAST uses a strong magnet to convert the axion back to a photon, again by the Primakoff effect. The photons subsequently hit a detector.

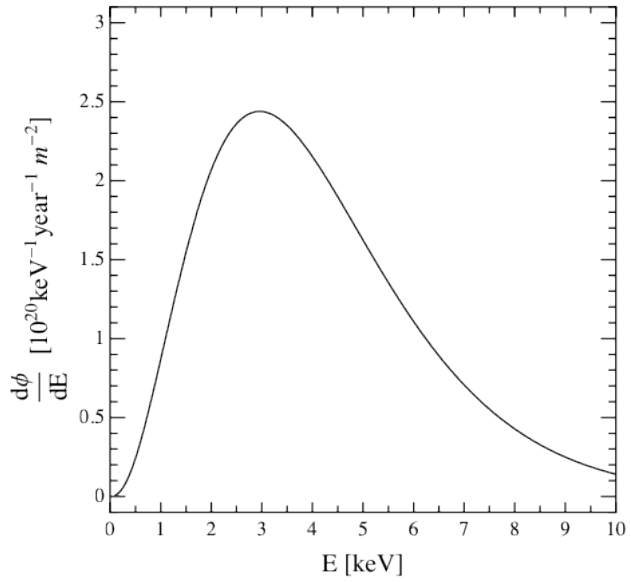

Figure 4.1: Solar axion flux spectrum at Earth based on the Primakoff conversion. The spectral shape is predicted by solar observations and the unknown axion-photon coupling constant, $g_{a\gamma}$, which is only a multiplicative factor.

The spectrum of X-rays from solar axions reaching Earth can be seen in figure 4.1. It is relatively low energy X-rays with a peak around 3 keV and a shape similar to the black-body radiation spectrum.

Cosmological observations constrain the axion mass between 1 μeV and 1 eV. In figure 4.2 the parameter space can be seen with the axion-photon coupling constant, $g_{a\gamma}$, as a function of the axion mass, m_{axion}. The yellow line represents the area where we expect to see the axion if all dark matter in the universe consists of axion particles with the same m_{axion} and $g_{a\gamma}$. The CAST helioscope is by 2014 the most comprehensive axion search, and has set an experimental upper limit of

$$g_{a\gamma} \leq 8.8 \cdot 10^{-11} \text{ GeV}^{-1} [65,\ 66]. \tag{4.1}$$

The CAST experiment is largely made from spare parts of other projects at CERN and other research institutions. The magnet is one of three prototype superconducting dipole magnets from the Large Hadron Collider. It is designed to transport particles in two directions inside a strong magnetic field, so it has two bores inside with diameters of 43 mm. As can be seen in the picture of the CAST instrument (figure 4.3), the magnet is able to pitch and yaw up to a limit. That makes it possible to follow the sun as it comes up with one end, and as it goes down with the other end. Since the axion does not interact with matter, detectors are

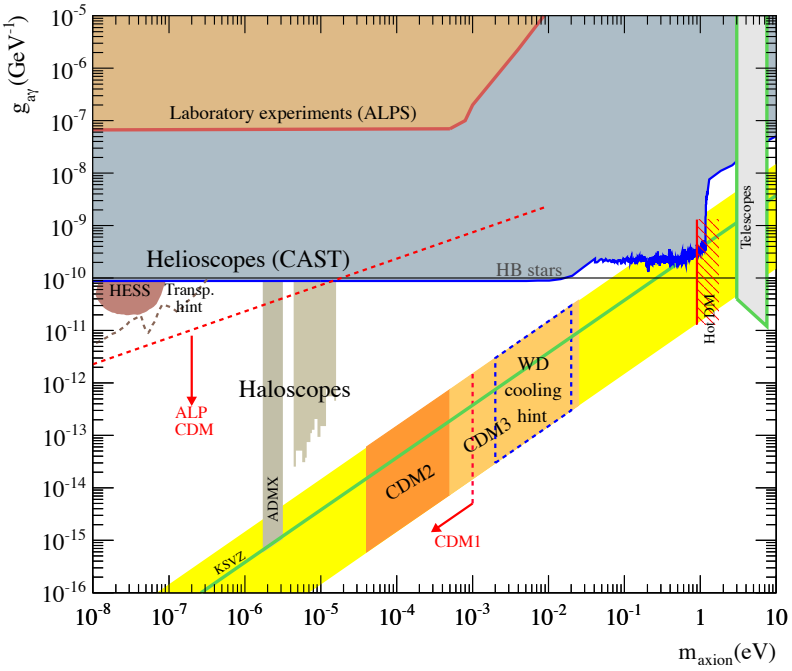

Figure 4.2: The axion (and axion-like partikle) parameter space, showing the limits of detection for current direct detection experiments. The yellow "axion band" represents areas of the parameter space where theoretical models predicts axions. The part of the parameter space excluded by the CAST axion helioscope so far is represented by the blue line and grey area. (From [64])

placed at both ends of the magnet and at both boreholes, so two detectors can be used at sunrise and two at sunset. The detectors used are low-background time projection chambers with MicroMegas readouts [67, 68, 69]. They were originally developed for ion detection, where a charged particle interacting with a gas creates a an avalanche of ion/electron pairs in the presence of a strong electric field. Similarly, an X-ray photon in a gas will ionize the atoms to create ion/electron pairs. The cascade of electrons will drift towards a readout electrode and the shape and amplitude of the signal yields information on the energy of the initial charged particle. A mesh of readout electrodes will give a position sensitive detector that gives a 2D output of positions and the energy spectrum at each position.

CAST has been doing axion searches since 2002 and the experiment continually improves and reiterates the equipment to get higher sensitivity. One major problem is to get a high enough signal-to-noise ratio, the majority of the noise coming from background radiation from the ground, the materials in the instrument and cosmic rays. The detectors cover the entire area of each bore opening, so are relatively large. Detector size is proportional to the background radiation, so it makes sense to have smaller detectors. By using X-ray optics, the X-ray photons can be focused into a detector area of only a fraction of the previous. This will significantly increase the signal-to-noise ratio and will let the CAST helioscope search for the axion in new areas.

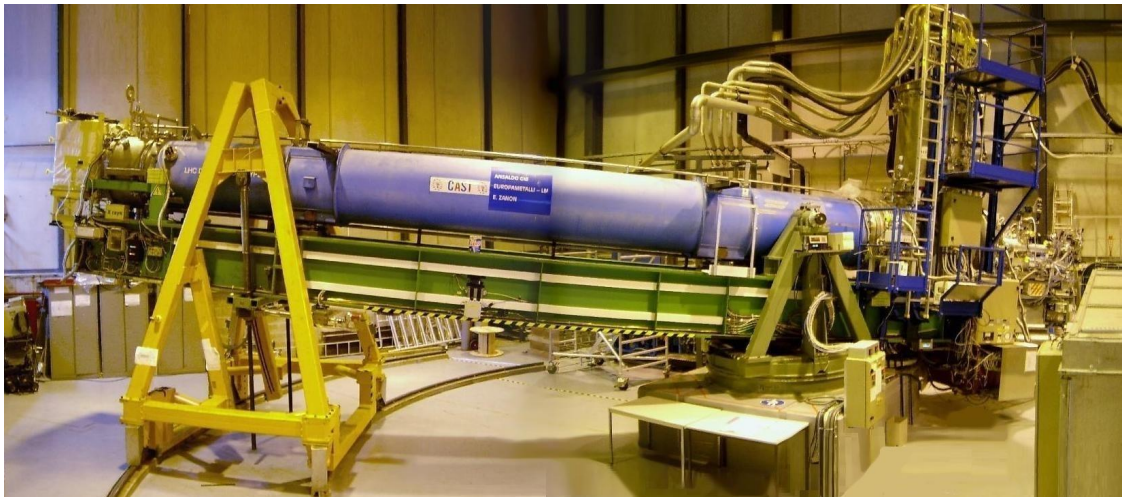

Figure 4.3: The Cern Axion Solar Telescope (CAST) located near Geneva, Switzerland. The main component of the experiment is a Large Hadron Collider (LHC) prototype dipole magnet that has a 10 T magnetic field, physical length of 13 meters and a mass of 50 tonnes.

4.2 Developing an optic for CAST

One major concern in making an X-ray optic from NuSTAR glass for the CAST helioscope is the limited space available. The optic would have to fit on the end of the magnet nearest the wall, which leaves only about 2 meters for optic, detector and the focal length between the two. Another problem is the small bore opening of only 43 mm, which is smaller than the inner radius of the NuSTAR telescopes. Both of those problems can be solved by realising that the optic does not require a symmetric field of view and that the axion spectrum is of relatively low energies. In figure 4.5 is seen a top-down view of the end of the magnet bore where the optic and detector can be attached. By stacking a number of reflectors, X-rays can be reflected to one side, something that would not be possible for a traditional imaging X-ray astrophysical telescope.

By using only 1/6 of the Wolter I azimuthal area, a pie-slice (figure 4.4), two stacks of mirrors can be used to reflect X-rays to one side. The stack only needs to be high enough to cover the bore opening, but each mirror should also be wide enough. The NuSTAR glass pieces are made in 60° segments for the inner radii and 30° segments for the outer radii.

4.2.1 Optic geometry considerations

The geometry of the optic was calculated using the following equation for a Wolter I optic:

$$\tan(4\alpha) = \frac{R3}{f}, \tag{4.2}$$

where α is the angle of reflection of each mirror, f is the focal length and $R3$ is the radius between center of optic and the midpoint between parabolic and hyperbolic mirror (figure 4.6). The center of the bore will need an off-set with the focal plane of the telescope, given

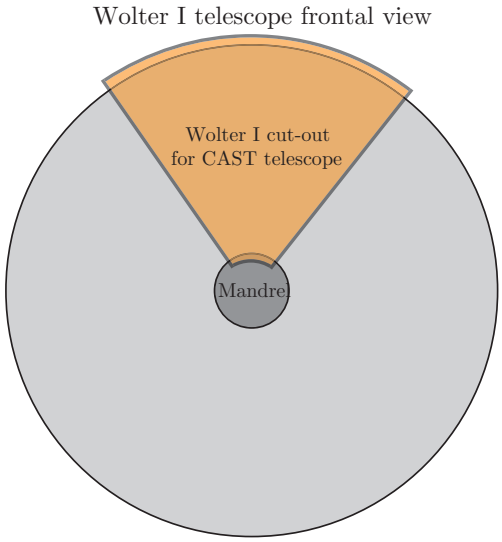

Figure 4.4: Front view of Wolter I type optic with section used in the CAST XRT shown.

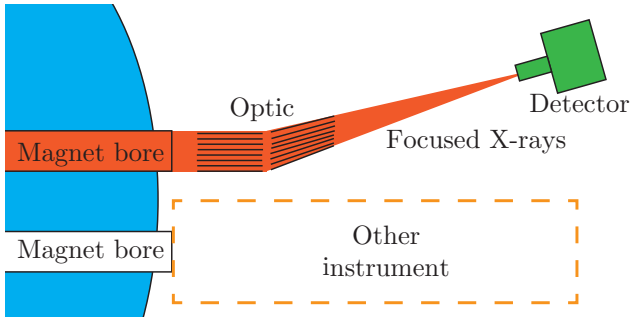

Figure 4.5: Top-down view of the end of the CAST magnet, where an optic can be attached at one magnet bore. The other magnet bore is taken up by another instrument, resulting in limited space for the CAST XRT.

by $d = r_{\text{bore}} + r_{\text{min}}$, where r_{bore} is the radius of the bore and r_{min} is the minimum radius of a NuSTAR optic. The length of the NuSTAR mirrors is $l = 225$ mm.

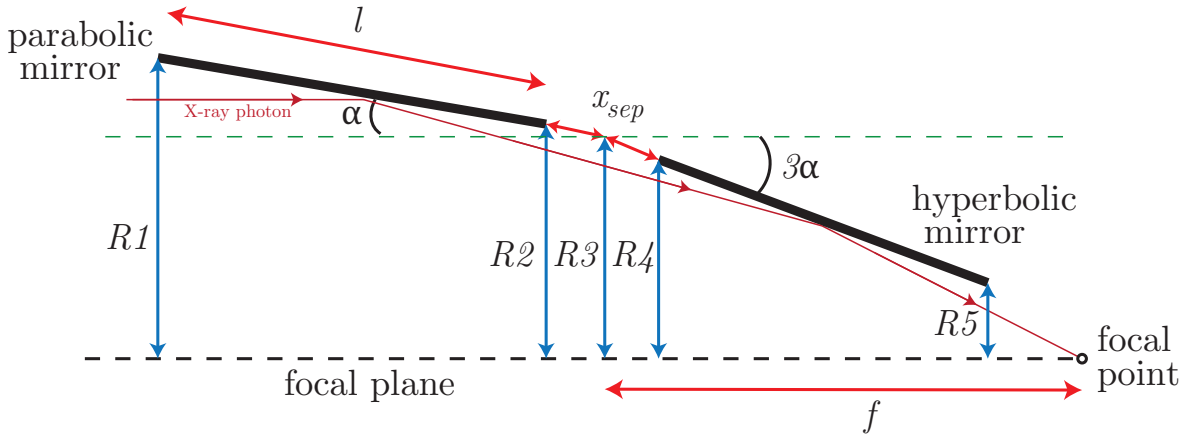

Figure 4.6: Diagram of Wolter I from side with *R1*-*R5* designated. The principle of the Wolter I double reflection can be seen as an X-ray photon is reflected off the parabolic and hyperbolic mirrors. l is mirror length, f is focal length, x_{sep} is distance between parabolic and hyperbolic mirror and α is the angle of reflection for an X-ray photon parallel to the focal plane.

The focal length f was set to a fixed value of 1.5 m. Using r_{min} as the 0th layer radius, $R3_0$, the angle of the first layer, α_0, can be calculated using eq. 4.2. From α_0 and $R3_0$, we can calculate $R1_0$, $R2_0$, $R4_0$ and $R5_0$:

$$R2_i = R3_i + 0.5\ x_{\text{sep}} \tan(\alpha_i), \tag{4.3}$$
$$R1_i = R2_i + l \sin(\alpha_i), \tag{4.4}$$
$$R4_i = R3_i - 0.5\ x_{\text{sep}} \tan(3\alpha_i), \tag{4.5}$$
$$R5_i = R4_i - l \sin(3\alpha_i), \tag{4.6}$$

for layer $i = 0$, where x_{sep} is the distance between the parabolic and hyperbolic mirror. $R4_1$ and $R5_1$ will be a lower value than r_{min}, so it was nessecary to increase the bore to focal plane distance, d.

The next layer can be added by setting $R3_{i+1} = R1_i + d_{\text{glass}}$, where d_{glass} is the thickness of the glass. Thereby the opening of the next layer will be exactly large enough for all incoming photons to hit the parabolic mirror. All mirror layers are subsequently added using the same method until the stack is high enough to cover the bore opening:

$$R1_{\text{last}} \geq r_{\text{min}} + 2r_{\text{bore}}. \tag{4.7}$$

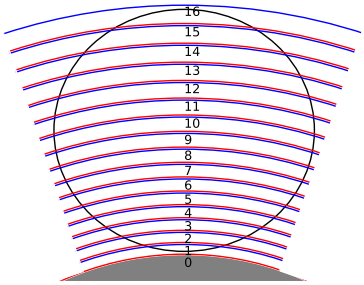

Figure 4.7: Computer generated CAST XRT design from front. Black ring designates the magnet bore opening.

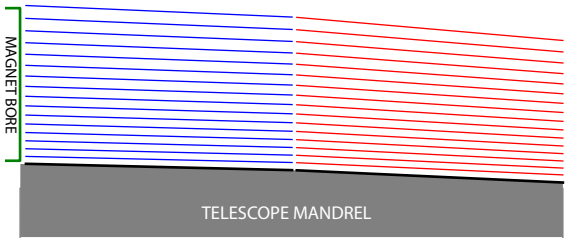

Figure 4.8: Computer generated CAST XRT design from side. Magnet bore opening is shown to the left.

The calculated geometry can be seen in figure 4.7 and 4.8. The calculated radius and angle for each layer can be seen in table 4.1. The area is the cross sectional area of the layer opening which overlaps with the magnet bore opening, a description of the calculation can be seen in section 4.2.3.

Layer	Area [mm^2]	α [°]	α [mrad]	$R1$ [mm]	$R5$ [mm]
1	13.863	0.579	10.113	63.006	53.821
2	48.175	0.603	10.530	65.606	56.043
3	69.270	0.628	10.962	68.305	58.348
4	86.760	0.654	11.411	71.105	60.741
5	102.266	0.680	11.877	74.011	63.223
6	116.172	0.708	12.360	77.027	65.800
7	128.419	0.737	12.861	80.157	68.474
8	138.664	0.767	13.382	83.405	71.249
9	146.281	0.798	13.921	86.775	74.129
10	150.267	0.830	14.481	90.272	77.117
11	149.002	0.863	15.062	93.902	80.218
12	139.621	0.898	15.665	97.668	83.436
13	115.793	0.933	16.290	101.576	86.776
14	47.648	0.970	16.938	105.632	90.241

Table 4.1: Geometric properties of the computer generated CAST XRT design.

Finally, we note that the actual radii and angles had to be slightly adjusted to allow the optic adhere to a cone-approximation to a true Wolter I design. These minor modifications to the radii and graze angles ensured the best possible focusing of the telescope and had negligible impact on multilayer optimisation.

4.2.2 Optimising reflective coatings

To achieve the maximum possible efficiency of the optic, the coating needed to be optimised for the energy range. In contrast with most astrophysical observatories, the CAST telescope will only look at a single object with a very specific spectrum. That means that the coatings can be tailored to achieve maximum reflectivity in that area of the spectrum. Also known is the quantum efficiency of the detector.

An algorithm was developed to calculate all the different permutations of multilayers for a wide variety of material combinations. The spectrum is at a relatively low X-ray energy, so single layer coatings could be relevant. The algorithm calculates the reflectivity for a multilayer with given material combination and geometry at an angle, α, given by the radius of the layer from the optical axis. *F.O.M.* is then calculated using the following integral:

$$F.O.M. = \int_{0.1}^{10} \mathbb{R}^2(\alpha, \mathrm{E})\ QE_{\mathrm{det}}(\mathrm{E})\ S_{\mathrm{axion}}(\mathrm{E})\ dE, \tag{4.8}$$

with $\mathbb{R}^2(\alpha, \mathrm{E})$ being the squared reflectivity because of the double reflection, $QE_{\mathrm{det}}(\mathrm{E})$ the detector quantum efficiency and $S_{\mathrm{axion}}(\mathrm{E})$ the axion spectrum as seen in figure 4.1. By integrating over the energy range from 0.1 keV to 10 keV, a figure of merit can be obtained that takes both coating, spectrum and detector into account.

The material combinations considered were multilayers of W/B_4C, W/Si, Pt/C, Pt/B_4C, Ni/B_4C as well as single layers of W, Pt, Ir and Ni. W/Si and Pt/C were the most well understood for slumped glass type substrates, since they both were used in the NuSTAR mission. To find the optimal coating, the parameter space considered for each material combination can be seen in table 4.2. By using d_{min} and d_{max}, both linearly graded-d coatings and constant-d coatings can be computed. To avoid computing cases where d_{min} is larger than d_{max}, the condition $d_{\mathrm{min}} \leq d_{\mathrm{max}}$ was set.

Parameter	Minimum	Maximum	Interval
N	1 layer	30 layers	1 layer
d_{min}	3 nm	300 nm	0.5 nm
d_{max}	3 nm	300 nm	0.5 nm
Γ	0.1	0.9	0.05

Table 4.2: Parameter space used for finding optimal coating recipes for each material combination.

For single layer coatings, only a single thickness of 50 nm was considered. The surface and interface roughnesses were fixed at 0.5 nm. The complete computation can be done for

every layer in the optic, as α changes throughout the mirror stack. The algorithm does the following steps:

1 Finds the next combination in the parameter matrix.

2 Calculates the reflectivity using IMD's FRESNEL function.

3 Uses the calculated reflectivity in the $F.O.M.$ equation 4.8.

4 If the calculated value is higher than the previous maximum value, the parameters are saved and the calculated value set as the new maximum.

When the entire parameter space has been covered for a mirror layer and material combination, the algorithm saves the best $F.O.M.$ value and the coating recipe and goes on to the next mirror layer. When all mirror layers are covered, the effective area is calculated whereafter the algorithm continues on to the next material combination.

For the CAST coatings, making a separate coating recipe for each layer would result in having to produce ∼14 different coating runs, each with only four mirror substrates. Instead only four different coating recipes were made, where each recipe would be applied to three or four mirror layers. That way 16 mirror substrates could be coated at a time and all substrates could be coated in four coating runs. The result of a full computation using the algorithm with four recipes is shown in figure 4.9.

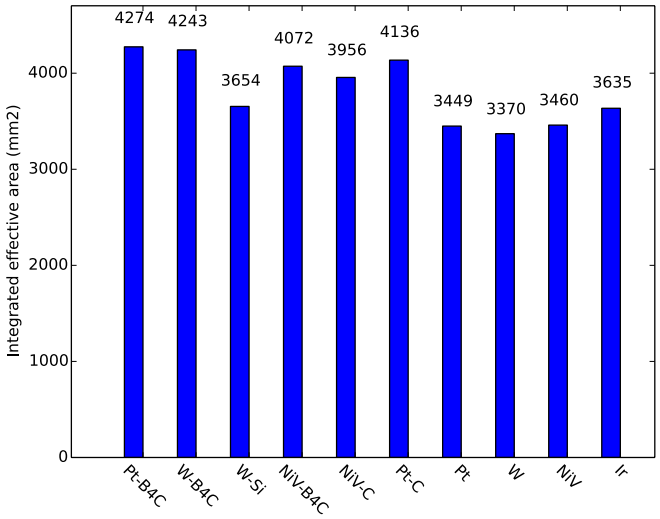

Figure 4.9: Integrated effective area comparison for computed material combinations in the CAST XRT optic.

The best result for the Pt/C material combination can be seen in figure 4.10, which is the output from the software for a given material combination. Curves show the reflectivity squared times detector quantum efficiency times axion spectrum ($\mathbb{R}^2 \cdot QE_{\text{det}} \cdot S_{\text{axion}}$) for a given recipe. In figure 4.11 can be seen a table of the optimised coating recipes along with side view illustrations of the coatings.

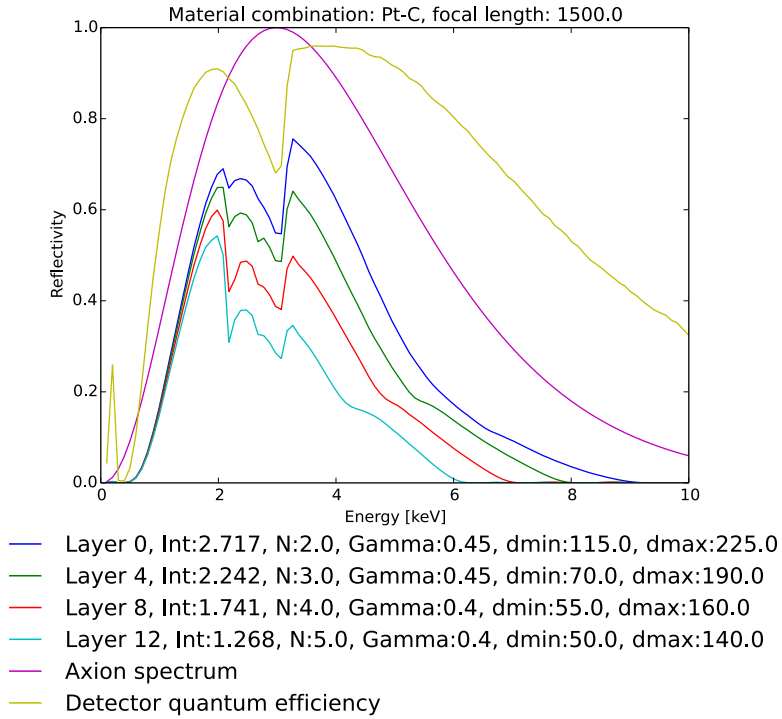

Figure 4.10: Optimised coatings for CAST XRT with a Pt/C material combination as calculated by the software. The four recipes are for layer 0-3 (layer 0 is the mandrel), layer 4-7, layer 8-11 and layer 12-14.

The coating optimisation for the CAST X-ray optic was done in parallel with most of the Athena coating investigations that is described in chapter 3. The findings from long term storage that are discussed in section 3.4 show changes in the coatings over time at ambient conditions for most boron carbide containing films. For that reason, it was decided to make the CAST coatings with Pt/C, as the combination is well described for NuSTAR-like glass substrates. W/Si was also used for NuSTAR and would be a cheaper solution, but the silicon absorption line at ~ 2 keV would decrease efficiency of the coatings around the peak of the axion spectrum.

4.2.3 Calculating effective area

As also described in section 4.2.3, the effective area is the cross sectional opening of the optic multiplied by reflectivity squared for each layer. Total effective area is the sum of effective area for each layer:

$$A_{\mathrm{eff,i}} = A_{\mathrm{CS,i}}\mathbb{R}_i^2(\mathrm{E}) \tag{4.9}$$

$$A_{\mathrm{eff}} = \sum_{i=0}^{n} A_{\mathrm{eff,i}} \tag{4.10}$$

The cross sectional opening is the intersection of the circle of the bore opening and a layer opening. The layer opening is the cross sectional area between two circles of radius $\mathcal{R}_i$ and

Recipe	# of layers	d_{min}	d_{max}	Γ
1	2	11.5	22.5	0.45
2	3	7.0	19.0	0.45
3	4	5.5	16.0	0.4
4	5	5.0	14.0	0.4

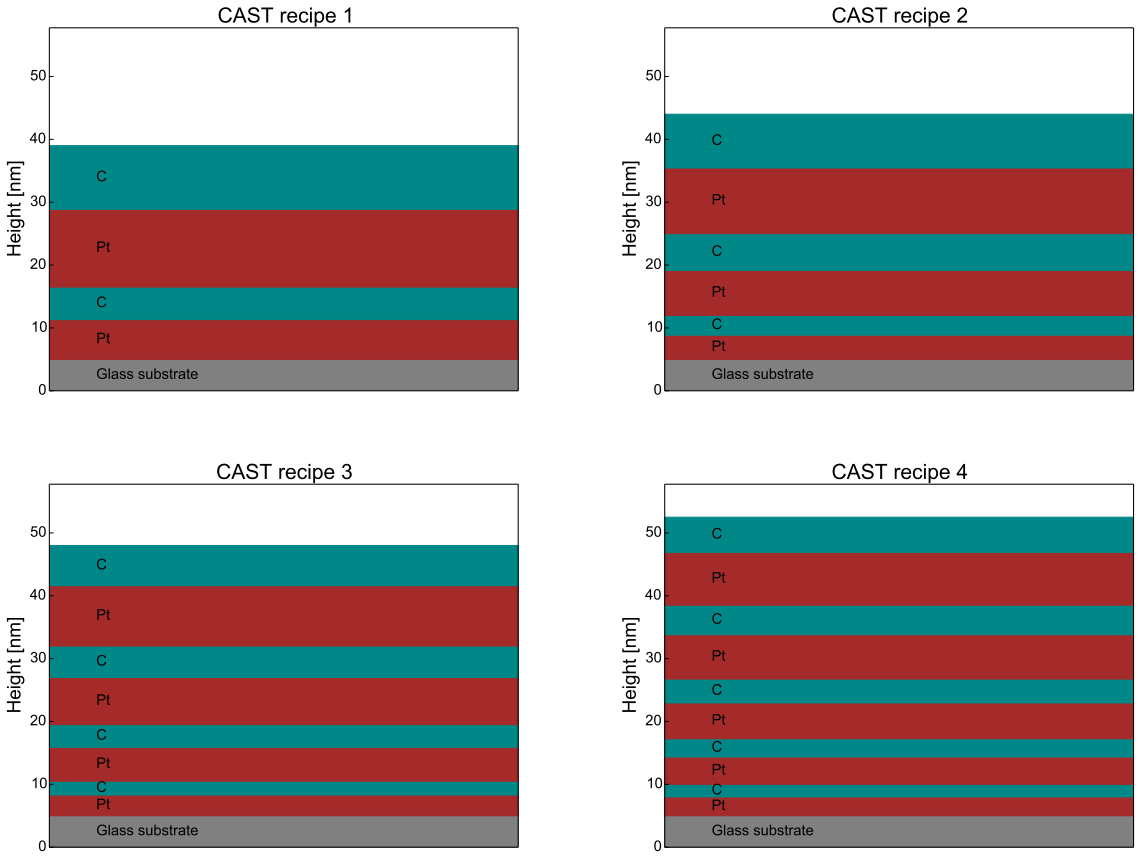

Figure 4.11: Side view illustrations of the four optimised coating recipes calculated for CAST, along with a table showing the recipes.

$\mathcal{R}_{i-1}$, where

$$\mathcal{R} = R1. \tag{4.11}$$

It can be calculated using the overlap of the outer shell of the layer opening and the bore opening. From that is subtracted the overlap of the inner shell of the layer opening with the bore opening as seen in figure 4.12.

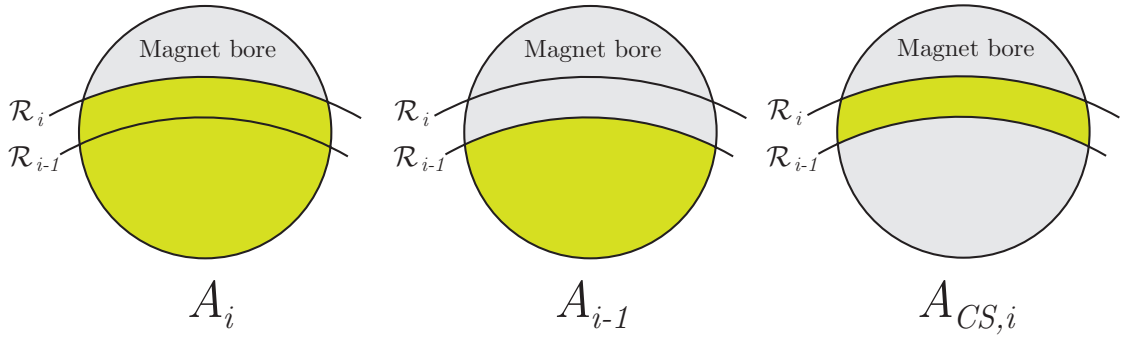

Figure 4.12: Diagram of cross sectional area (CSA) calculation for the intersection of the CAST XRT and CAST magnet bore. **Left:** CSA of layer i and magnet bore. **Middle:** CSA of layer $i-1$ and magnet bore. **Right:** CSA between layer i, $i-1$ and magnet bore.

Area of the overlap of shell i with bore (figure 4.12 left) is:

$$\begin{aligned} A_i &= r_{\text{bore}}^2 \cos^{-1}\left(\frac{d^2 + r_{\text{bore}}^2 - \mathcal{R}_i^2}{2 d r_{\text{bore}}}\right) \\ &\quad + \mathcal{R}_i^2 \cos^{-1}\left(\frac{d^2 - r_{\text{bore}}^2 + \mathcal{R}_i^2}{2 d \mathcal{R}_i^2}\right) \\ &\quad - \frac{1}{2}\sqrt{(-d + r_{\text{bore}} + \mathcal{R}_i)(d + r_{\text{bore}} - \mathcal{R}_i)} \\ &\quad \times \sqrt{(d - r_{\text{bore}} + \mathcal{R}_i)(d + r_{\text{bore}} + \mathcal{R}_i)}, \end{aligned} \tag{4.12}$$

Area of the overlap of shell $i-1$ with bore (figure 4.12 middle) is:

$$\begin{aligned} A_{i-1} &= r_{\text{bore}}^2 \cos^{-1}\left(\frac{d^2 + r_{\text{bore}}^2 - \mathcal{R}_{\text{bot}}^2}{2 d r_{\text{bore}}}\right) \\ &\quad + \mathcal{R}_{\text{bot}}^2 \cos^{-1}\left(\frac{d^2 - r_{\text{bore}}^2 + \mathcal{R}_{\text{bot}}^2}{2 d \mathcal{R}_{\text{bot}}^2}\right) \\ &\quad - \frac{1}{2}\sqrt{(-d + r_{\text{bore}} + \mathcal{R}_{\text{bot}})(d + r_{\text{bore}} - \mathcal{R}_{\text{bot}})} \\ &\quad \times \sqrt{(d - r_{\text{bore}} + \mathcal{R}_{\text{bot}})(d + r_{\text{bore}} + \mathcal{R}_{\text{bot}})}, \end{aligned} \tag{4.13}$$

where

$$\mathcal{R}_{\text{bot}} = \mathcal{R}_{i-1} + d_{\text{glass}}, \tag{4.14}$$

with $\mathcal{R}_{i-1}$ being the radius of the layer underneath layer i and d_{glass} being the thickness of the glass.

The NuSTAR type telescope is built up from glass layers with graphite spacers between. Since the optic is so small, but with relatively large openings between the layers, it is necessary to use graphite spacers in the middle. Each of those are rectangular in shape, as high as the opening and $x_{\mathrm{gr}} = 2$ mm wide. The spacer obscures the opening, so will have to be subtracted from cross sectional opening. The cross sectional area of the opening of layer i is then:

$$A_{\mathrm{CS,i}} = A_i - A_{i-1} - (\mathcal{R}_i - \mathcal{R}_{i-1})x_{\mathrm{gr}} \tag{4.15}$$

The effective area and throughput for the optimised Pt/C coating can be seen in figure 4.13.

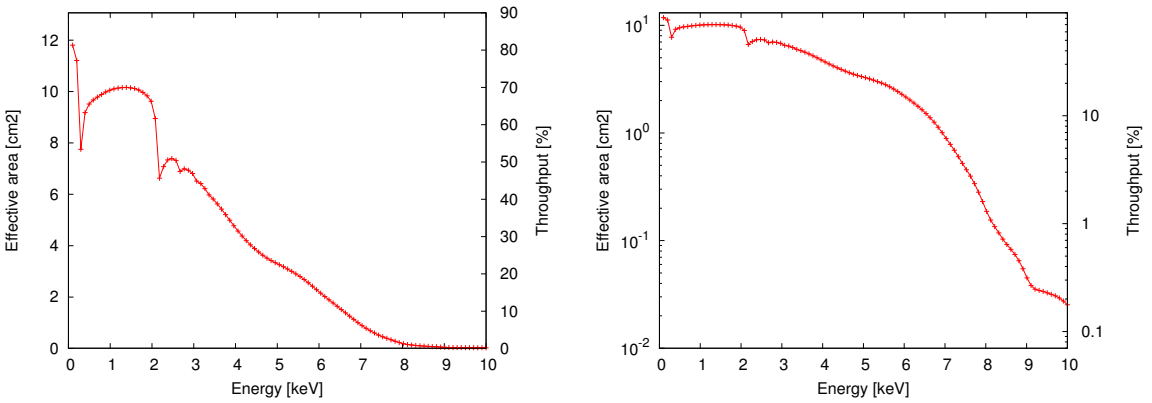

Figure 4.13: Linear and logarithmic effective area curves of the CAST XRT given in cm^2. Throughput is given on the right side of each plot as the fraction of the magnet bore covered by the optic at a given energy.

4.3 Producing coated substrates

DTU Space has a fairly large selection of leftover slumped glass substrates from the NuSTAR mission. An extra amount of glass substrates were produced to cover broken pieces and pieces that failed visual inspection. From this surplus, the substrates for the CAST XRT was selected.

4.3.1 Collecting substrates for coating

Each layer for NuSTAR corresponded to a shell diameter, which was described in the serial number of each substrate. The serial number includes diameter and wether it is a parabolic or hyperbolic piece. It is written with a marker on the back of the substrate like the following:

NXXX(A/B)yyy-zzz(s/p),

where XXX is the diameter of the shell, (A/B)yyy describes the production batch of the slumped glass process, zzz is the layer number of the optic and (s/p) describes wether it

is for the first or second stack (parabolic or hyperbolic). The NuSTAR optic is a conical approximation to the Wolter I geometry, but the glass substrates are produced on cylindrical mandrels. So instead of being parabolic or hyperbolic, they are straight along the optical axis.

To find pieces for the CAST XRT, the diameter described by XXX would need to correspond with the calculated *R1* and *R2* values for the first piece, or *R4* and *R5* for the second piece. The pieces should be mounted at higher grazing incidence angles than NuSTAR, so the difference between *R1* and *R2* are higher for CAST than NuSTAR. That difference would need to be corrected for by bending each piece to the correct shape during the mounting process. The NuSTAR pieces corresponding to the CAST radii can be seen in table 4.3.

Figure 4.14: Glass substrates selected for the CAST XRT before cleaning. The substrates required for each recipe were collected in four different baskets.

With 14 glass layers and two stacks, 28 pieces are needed for the CAST XRT optic. As the glass pieces are very fragile and tend to break, it was decided to produce twice the amount, 56 in total.

Each piece was visually inspected and the best pieces were selected for the CAST XRT (figure 4.14). The pieces were subsequently cleaned by the following process:

1. Ethanol rinsing to clear away markers.
2. Clean room wipes were used to remove visible blemishes.
3. 15 min. in ultrasonic bath with milli-Q water and soap (figure 4.15).
4. Thorough rinse with milli-Q water to remove soap.
5. 15 min. in ultrasonic acetone bath (figure 4.16).
6. 15 min. in ethanol bath (figure 4.16).
7. Each piece rinsed with milli-Q water and carefully dried with dry N_2.
8. Visual inspection, if failed, repeat from step 2.

Layer	Mean diam. (parabolic) [mm]	Corresp. NuSTAR diam. [mm]	Mean diam. (hyperbolic) [mm]	Corresp. NuSTAR diam. [mm]
1	124.2	124	114.7	116
2	129.3	128	119.5	120
3	134.7	136	124.4	124
4	140.3	140	129.6	128
5	146.0	144	134.9	136
6	152.0	152	140.5	140
7	158.3	160	146.2	148
8	164.8	164	152.2	152
9	172.5	172	158.4	160
10	178.4	180	164.8	164
11	185.7	184	171.5	172
12	193.2	192	178.5	180
13	201.0	200	185.7	184
14	209.1	208	193.1	192

Table 4.3: Table of radii of each layer for the parabolic and hyperbolic mirrors in the CAST XRT compared to compatible NuSTAR radii.

Figure 4.15: Ultra-sonic bath with soap.

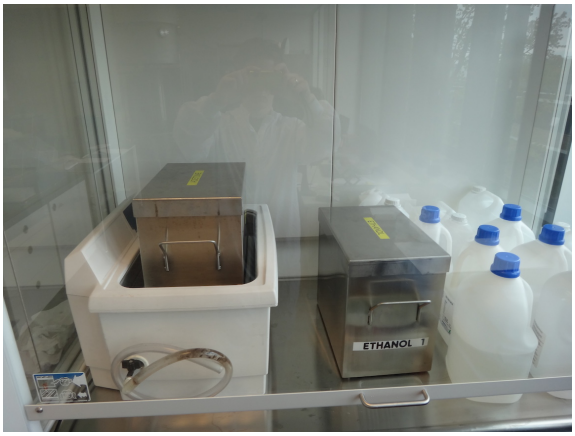

Figure 4.16: Acetone and ethanol tubs. **Left:** Acetone tub in ultra-sonic machine. **Right:** Ethanol tub.

The pieces were moved directly to sample mounting plates (figure 4.17) in a downflow module to avoid dust contamination.

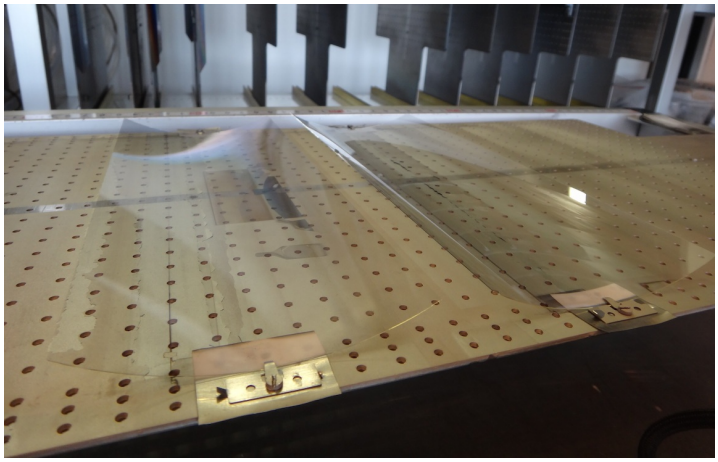

Figure 4.17: Cleaned glass substrates attached to sample mounting plate before coating. Two glass substrates were mounted onto each plate at positions 25 cm and 35 cm above coating chamber floor.

4.3.2 Coating of substrates

Four coating recipes were made for the CAST XRT. With 56 pieces to coat, 12-16 pieces are needed per recipe. The coating chamber in the DTU Space multilab can hold up to 36 substrates if the entire length of each cathode is utilized. To ensure a uniform coating, only the center part of the coating cathodes are used. Two substrates were mounted on each plate so the center of each sample was 25 cm or 35 cm above the chamber floor. Along with the glass substrates, two Si wafer pieces were installed on a separate plate at the same height to become witness samples.

From the coating optimisation calculations described in section 4.2.2, the optimal material combination was chosen to be Pt/C. Before coating, a thorough calibration was needed, which was done as described in section 2.3. Honeycomb (6.4 mm opening, 5 mm thickness) was used as collimation in front of the cathodes. A platinum target was mounted in cathode 2 and a 2-piece carbon target was mounted in cathode 4. Power settings were 450 W for cathode 2 and 900 W for cathode 4. Argon was supplied to the chamber at 88 SCCM, corresponding to a coating pressure of 2.9 mTorr. Background pressure for each coating was $\leq 2 \cdot 10^{-6}$ Torr.

In figure 4.18 can be seen the glass substrates after a coating still mounted in the coating chamber.

The coating was done with each material separately. With all cathodes turned off and the ring at the position where the first sample plate is between cathode 1 and 4, the ring would first move so sample plate 1 is next to the cathode of the first material. The cathode would then turn on, the shutter open and the ring start moving at the speed obtained from calibration corresponding to the thickness found in section 4.2.2. After one full rotation,

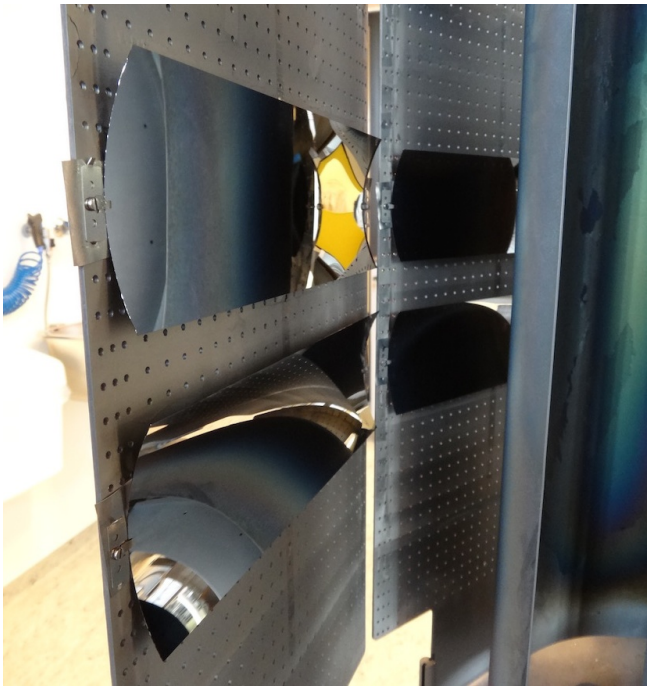

Figure 4.18: Mounted glass substrates in coating chamber after coating.

the shutter closes, the cathode turns off and the ring returns to the start position before starting on the next material.

The power supplies were polled every 5 seconds to get the power output, which can be seen in figure 4.19 for the coatings of recipe 1 and recipe 4. Cathode 5 and 6 are actually cathode 3 and 4 in the chamber, but are run from a third dual channel power supply. During the recipe 4 coatings can be seen some fluctuations in the cathode 4 power output, they are caused by the instabilities that occur when coating with non-metallic materials at high power.

The Si witness samples were measured at the XRR lab at DTU Space. XRR results from each witness sample for recipes 1-4 can be seen in figure 4.20. In each of the four coating runs, the two witness samples show completely similar XRR structure indicating a high uniformity between the two sample mounting positions. An exception is the witness samples from recipe 2, which show shifted peaks especially at higher angles as well as dissimilarities around the 5th peak.

XRR data of witness samples were compared to an IMD model as seen in figures 4.21, 4.22, 4.23, 4.24 and 4.25. All fits show good agreement with XRR measurements despite the difficulties in fitting graded-d coatings as each layer thickness and interface roughness is an independent variable. All fits showed Pt/C and C/Pt interface roughness of ∼0.25–∼0.35 nm.

Both top and bottom witness sample from the recipe 2 coatings were fitted given the dissimilarities stated above. The targeted coating for recipe 2 were 3 layers with $d_{min} = 7$ nm, $d_{max} = 19$ nm, $\Gamma = 0.45$. Both top and bottom witness sample show a significant

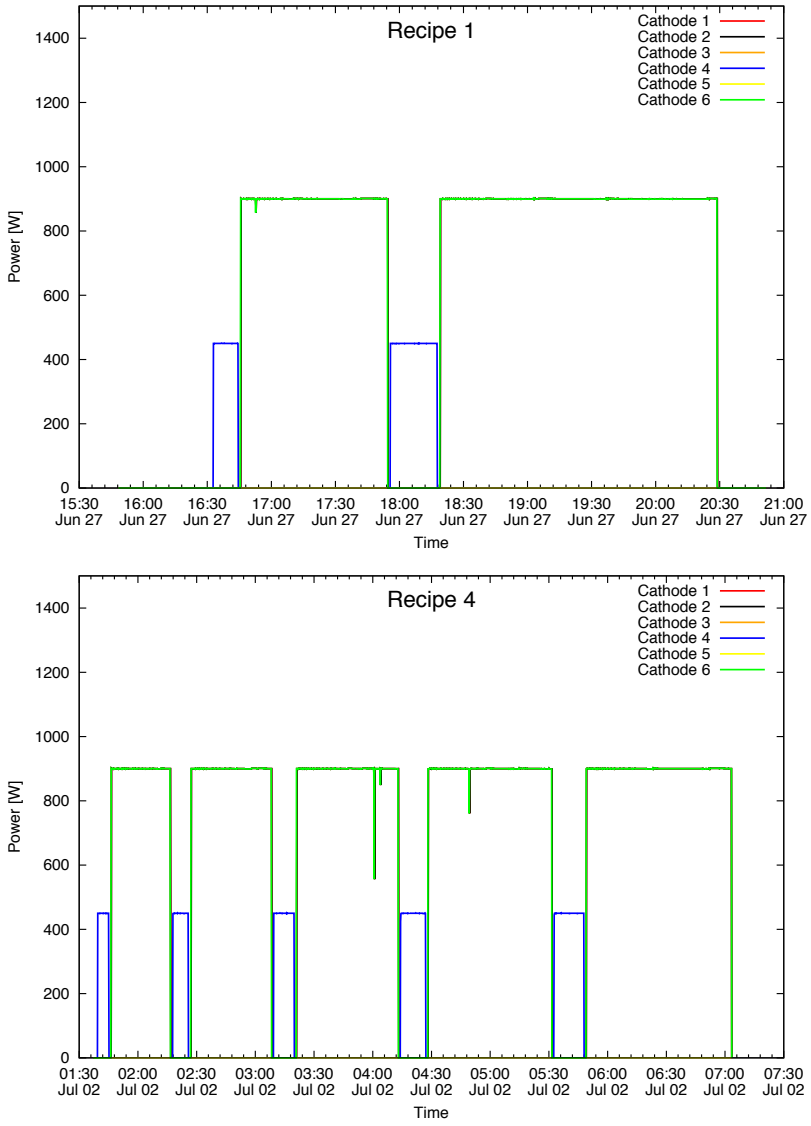

Figure 4.19: Graphs of power output delivered to cathodes from power supplies during CAST XRT multilayer coatings. **Top:** Cathode power output during recipe 1 coatings, two bilayers. **Bottom:** Cathode power output during recipe 4 coatings, five bilayers.

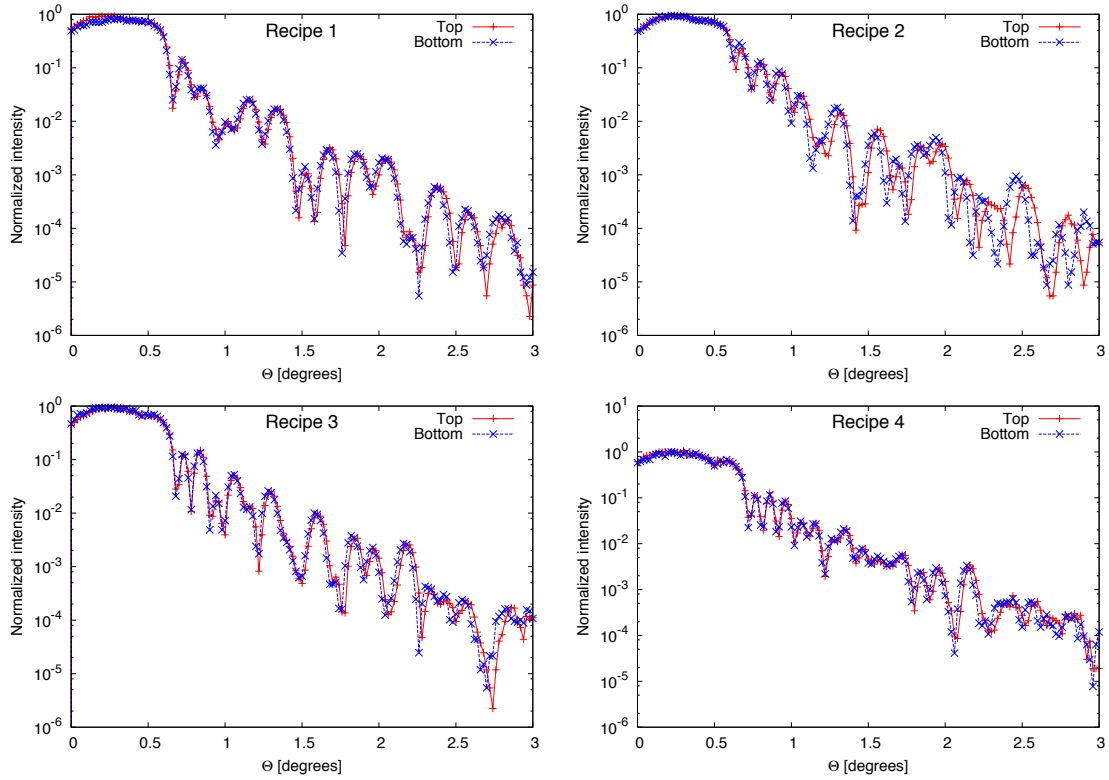

Figure 4.20: XRR measurements of witness samples from CAST XRT coatings recipe 1-4. Each coating run included two witness samples placed at 25 cm and 35 cm above coating chamber floor, same as glass substrates.

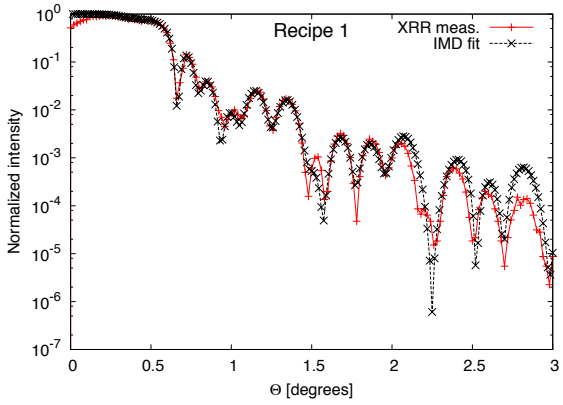

i	d_{aim} [nm]	Γ_{aim}	d_{fit} [nm]	Γ_{fit}
1	22.5	0.45	22.48	0.462
2	11.5	0.45	11.19	0.462

Figure 4.21: XRR measurement of witness sample from CAST XRT recipe 1 coating compared to IMD model fit.

irregularity in the second bilayer where $\Gamma \simeq 0.55$ and $d \simeq 13.93$-14.57 nm. The results warranted a thorough check of coating log and the coating macro used for the coating, as the irregularities could be at least partly explained by an error in the coating macro. No sign of error in the calculations of the coating macro, and the coating log also revealed that the speeds used during the coating corresponded to the values obtained in the calibration.

The d-spacings for the second layer in recipe 2 compared to IMD fits of XRR data from top and bottom witness sample are shown in table 4.4. An explanation for the inconsistencies

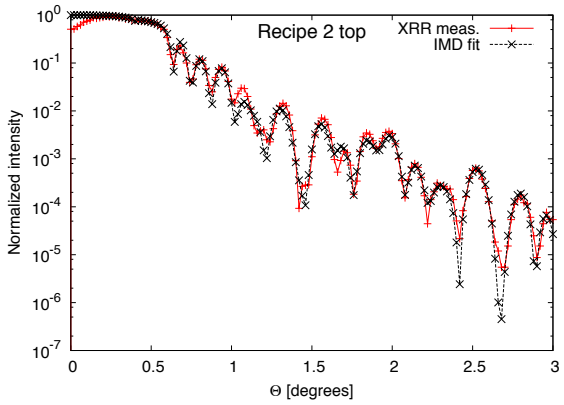

i	d_{aim} [nm]	Γ_{aim}	d_{fit} [nm]	Γ_{fit}
1	19	0.45	18.53	0.46
2	13	0.45	13.93	0.54
3	7	0.45	6.89	0.46

Figure 4.22: XRR measurement of witness sample from CAST XRT recipe 2 coating compared to IMD model fit. Witness sample was mounted 35 cm above coating chamber floor.

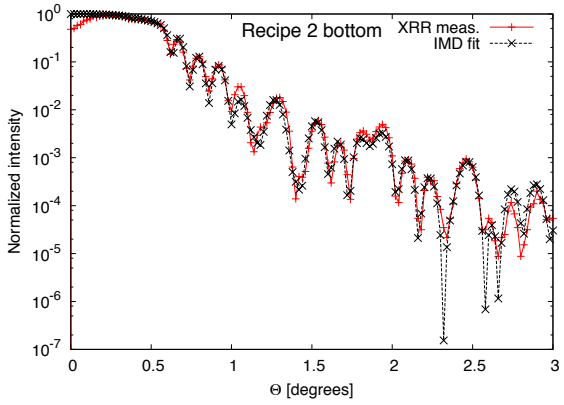

i	d_{aim} [nm]	Γ_{aim}	d_{fit} [nm]	Γ_{fit}
1	19	0.45	18.40	0.448
2	13	0.45	14.57	0.558
3	7	0.45	6.99	0.449

Figure 4.23: XRR measurement of witness sample from CAST XRT recipe 2 coating compared to IMD model fit. Witness sample was mounted 25 cm above coating chamber floor.

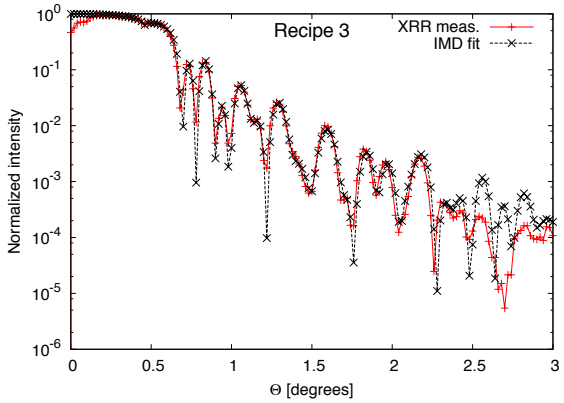

i	d_{aim} [nm]	Γ_{aim}	d_{fit} [nm]	Γ_{fit}
1	16	0.4	16.19	0.411
2	12.5	0.4	12.27	0.394
3	9	0.4	9.04	0.386
4	5.5	0.4	5.17	0.440

Figure 4.24: XRR measurement of witness sample from CAST XRT recipe 3 coating compared to IMD model fit.

between top and bottom witness sample could be problems with a cathode during coating. Column 3 shows inconsistencies between top and bottom witness sample in the carbon thickness, but it is not seen in the platinum thickness, column 5. That corroborates the hypothesis that the carbon cathode had difficulties during the application of the second layer, as indeed can be seen in figure 4.26. The cathode is only polled every 5 seconds,

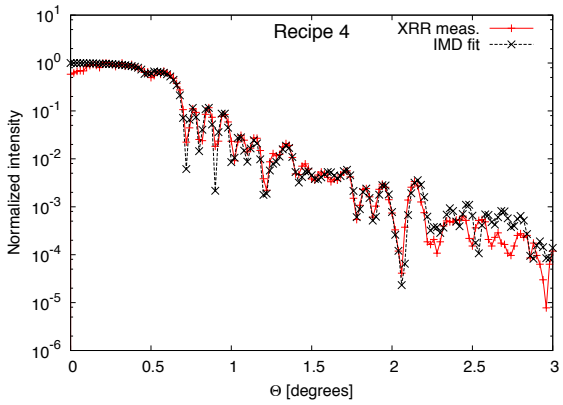

i	d_{aim} [nm]	Γ_{aim}	d_{fit} [nm]	Γ_{fit}
1	14	0.4	13.61	0.397
2	11.75	0.4	11.44	0.400
3	9.5	0.4	9.27	0.404
4	7.25	0.4	7.10	0.408
5	5	0.4	4.93	0.412

Figure 4.25: XRR measurement of witness sample from CAST XRT recipe 4 coating compared to IMD model fit.

Witn. sample	d-C_{aim} [nm]	d-C_{fit} [nm]	d-Pt_{aim} [nm]	d-Pt_{fit} [nm]
Top	5.85	7.52	7.15	6.41
Bottom	5.85	8.13	7.15	6.44

Table 4.4: Thicknesses of CAST XRT recipe 2 layer 2 in top and bottom witness sample, designed d-spacings from recipe compared to d-spacings obtained from XRR measurement and IMD fitting.

so intermittent dropouts between polling are likely to have occurred. Top and bottom witness sample were mounted on the same plate, so passed the cathode simultaneously. The difference in carbon thickness can only be explained by a non-uniform coating rate of carbon during the coating of layer 2. A partial dropout of the carbon cathode could have put the power supply in a state where to reignite the plasma, the cathode would for some time have a non-uniform plasma density. Another explanation could be a localized charge-up on the carbon target during coating caused by the insulating properties of the material [1]. Such a charge-up would change the electric field in front of the target and thereby create a non-uniform plasma density (see sec. 2.1.1).

The drop-outs of the carbon cathode can only explain the difference in carbon thickness between top and bottom witness sample. The inconsistencies of layer 2, recipe 2 is at the time of writing still of unknown origin.

The coated substrates were packed and shipped to LLNL for assembly.

The substrates were shipped with DHL, but the package was lost between Denmark and the US. A new batch of substrates were collected, cleaned, coated, packed and shipped during June/July of 2014. In this chapter is described the process for the second batch.

[1] The carbon targets used at DTU Space are boron-doped to increase the conductivity of the bulk material.

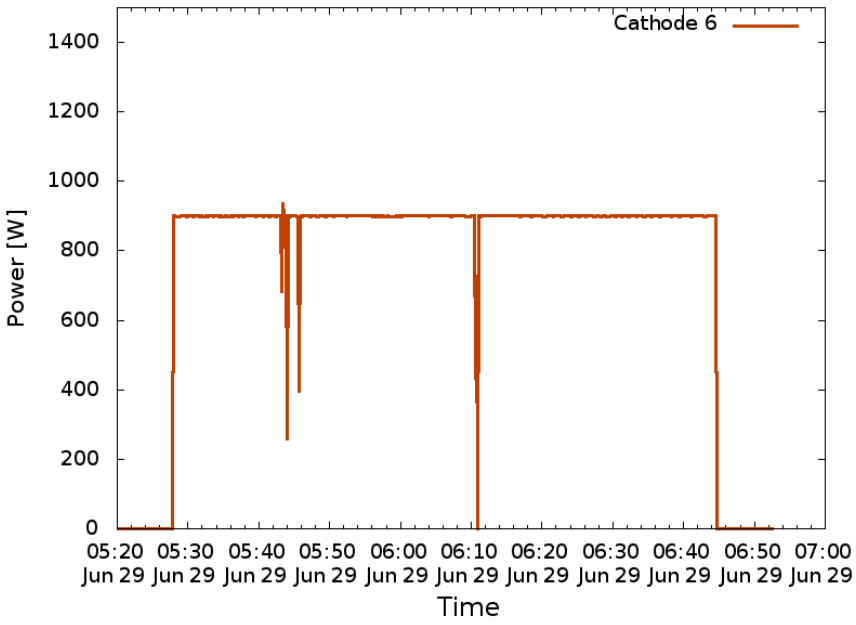

Figure 4.26: Power output delivered to cathode 6 (carbon target) during coating of layer 2, recipe 2.

4.4 Assembling coated substrates

Optic assembly was carried out at LLNL, where one of the NuSTAR assembly machines were set up for that purpose. The machine had been adjusted to make only a 30° section of substrates, and a specially designed Ti mandrel had been procured.

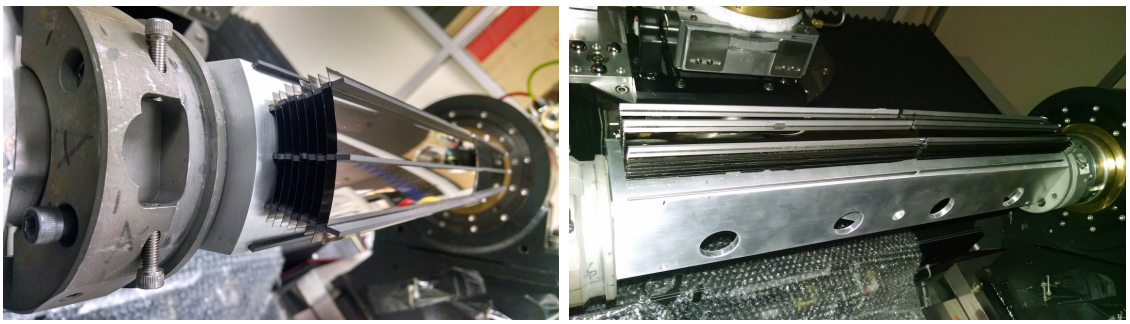

Figure 4.27: Pictures of glass substrates mounted on Ti mandrel during assembly. Three graphite spacers are attached on top of each glass substrate and machined to correct thickness before mounting of the next substrate.

Three graphite spacers were mounted onto the mandrel with epoxy glue and machined to the correct thickness before the two pieces for the first layer were mounted, again using epoxy. The next set of graphite spacers were mounted onto the first glass substrates and then machined to the right thickness (figure 4.27).

4.4.1 Vacuum vessel

The magnet bores and detectors in the CAST helioscope operates at vacuum levels, so the entire optic had to be mounted inside a vacuum vessel. To align the optic after mounting it on the CAST helioscope, it was necessary to have linear actuators for the translation and rotation of the optic while under vacuum.

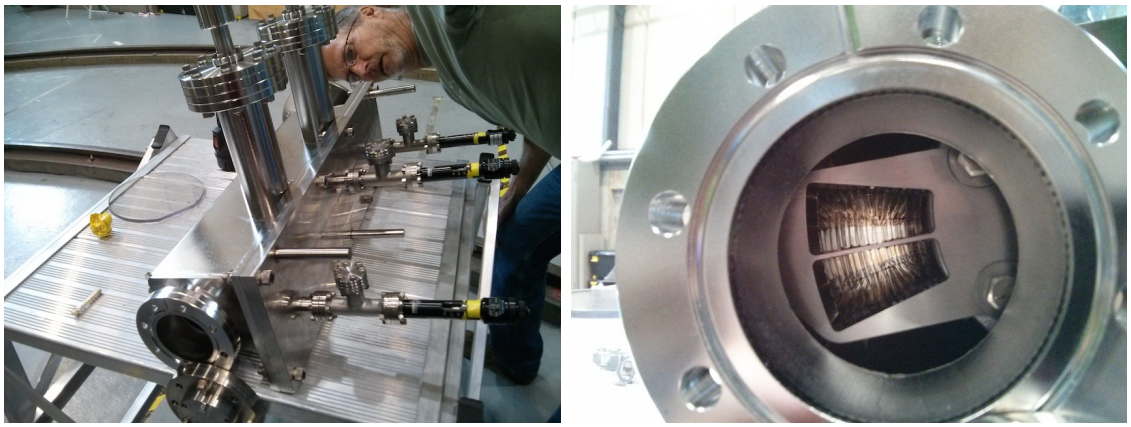

Figure 4.28: Vacuum vessel for the CAST XRT. **Left:** Vacuum vessel with linear actuators and guide rods viewable. CF flange is mounted directly to the magnet. **Right:** Inside of vacuum vessel as viewed from CF flange. A metal plate with two openings cover the graphite spacers in the center between the glass layers.

The vacuum vessel can be seen in figure 4.28. It was designed by Todd Decker (also pictured), an engineer from LLNL. In the picture can be seen five linear actuators, two on top to control pitch, three on the side, one for translation and two for yaw control. The three metal rods also visible on the side are for sliding out the optic, to make a precise optical alignment using a theodolite, described in detail in section 4.5.1.

Because of the limited space at the place where the optic had to be installed and the method of which to align it, the number of layers were cut from 14 to 13 layers. With 14 layers, the freedom of movement of the optic inside the vacuum vessel would have been severely limited and possibly caused the optic to hit the vacuum vessel wall during alignment.

4.5 Installation of optic at CAST

The optic mounted in the vacuum vessel was shipped to CERN for installation in Aug. 2014. The vessel was leak tested with He before being lifted into position in front of the magnet bore using a crane as seen in figure 4.29.

After mounting, vacuum view ports were mounted at either end of the magnet bores, making it possible to shine a laser straight through into the optic from the other end. The entire helioscope and magnet bore were also precisely aligned with a theodolite.

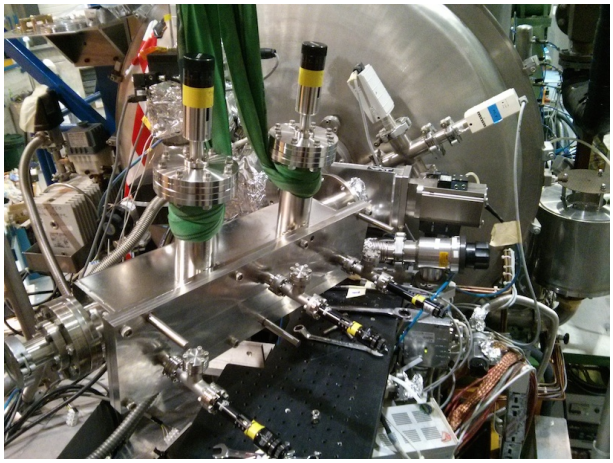

Figure 4.29: The vacuum vessel housing the CAST XRT is lowered into place at the end of the CAST magnet using a crane.

4.5.1 Optic alignment

Inside the vacuum vessel, specially designed metal pieces were mounted to either end of the mandrel, one piece can be seen in figure 4.28 (right). They have openings to allow photons into the optic and a narrow piece in the middle that blocks the graphite spacers between the glass pieces. Just above the top layer of glass was made a small hole in one of the metal pieces and on the other was mounted a small metal ball. The ball and hole were at the same distance from the center of the optic. The side of the vacuum vessel was designed so it could slide out a short distance along three precisely machined rods. By setting a pair of premachined spacers in the opening, the distance that the optic has slid out is exactly the distance from the hole and ball and the center of the optic.

A theodolite mounted 3 m from the front of the helioscope was aligned with the bore axis, so looking through the theodolite one could see the ball and hole of the optic. The optic rotation and translation could then be adjusted using the linear actuators to line up the ball and hole, and get a precise alignment. The theodolite could be set to shine a laser beam with adjustable divergence through the bore and at the optic. The view from the detector side can be seen in figure 4.30. After the hole and ball was lined up, the optic was slid back into the vacuum vessel and the bolts were fastened.

The optic reflected the laser light nicely, making it possible to get an exact position for the detector as seen in figure 4.31 (left). A fake detector with a carbonite back was used for the alignment. That allowed the laser light focused by the optic to shine at the carbonite back and be viewable from the other side.

The position of the detector was adjusted to make the spot hit in exactly the center. The detector mounts could then be fastened and the fake detector could then be replaced by a real one as seen in figure 4.31 (right).

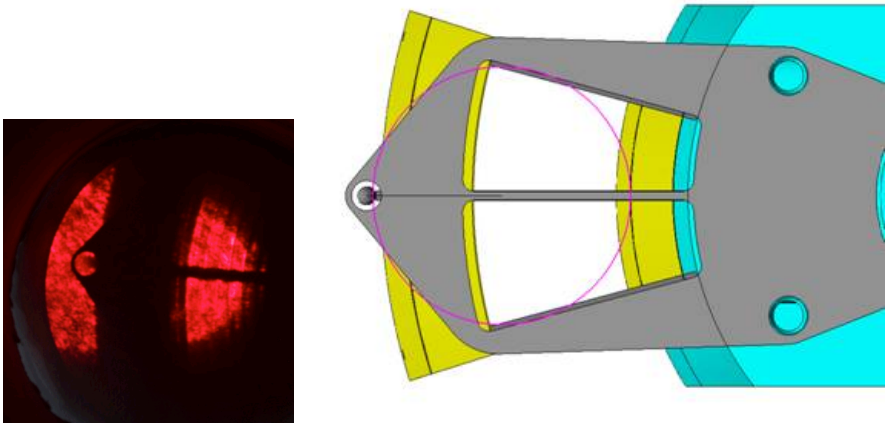

Figure 4.30: Left: Picture taken from the detector side of the CAST XRT as a divergent laser beam shines through. A piece of paper covers the opening and is lit up by the laser. The optic has been moved out for alignment and the ball and hole are visible above the top glass layer. **Right:** CAD drawing of the CAST XRT with end-plates showing the ball and hole of the gunsight used for alignment (from Todd Decker, LLNL).

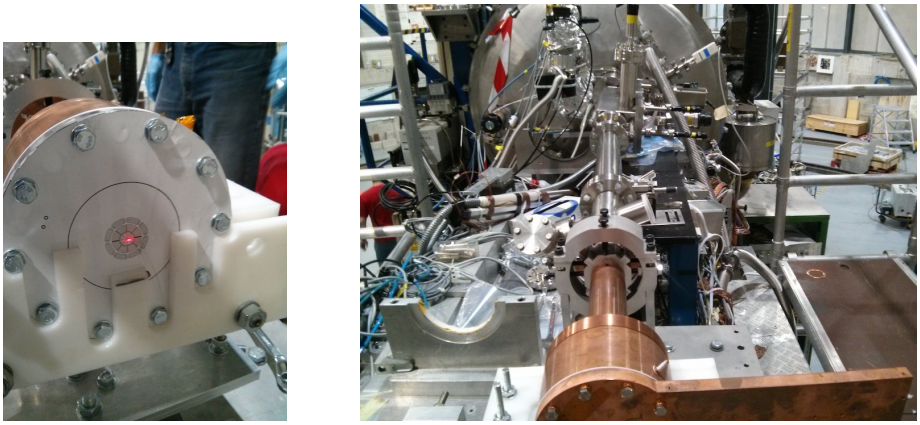

Figure 4.31: MicroMegas detector alignment. **Left:** A fake detector with a carbonite back was installed. The divergent laser beam focused to a spot by the X-ray optic can be seen through the carbonite back. **Right:** The fake detector was exchanged for a functioning MicroMegas detector in the same mounting bracket and was connected to the vacuum system with XRT and magnet.

4.5.2 Tests with 8 keV X-ray source

The last task with detector and optic in place was a test with X-rays. An X-ray souce had to be mounted in front of the helioscope, but still under vacuum. It was decided to use a COOL-X pyroelectric X-ray source. It works by warming and cooling a pyroelectric element, which emits electrons that subsequently hits a Cu target, resulting in a bremsstrahlung spectrum and characteristic Cu emission lines. The source has a flux of 10^8 photons/sec. emitted at an angle of 160°, so at a distance of ∼14.2 m from the optic, < 10 photons/sec. would arrive at the detector on average given the integrated efficiency of the optic and the detector.

Ray-tracing was done by Michael J. Pivovaroff from LLNL, and can be seen in figure 4.32. The simulations assumes a 6 mm diameter source placed 14.2 m from the optic and glass figure errors comparable to the NuSTAR optic. The MicroMegas data from the 5 hour measurement was rotated 45 degrees and binned into 200 x 200 μm^2 virtual pixels. By ray-tracing a 6 mm spot at discrete photon energies from 0-10 keV and using the measured spectrum as weight, a composite image was created to compare with measured data. The left plot of figure 4.32 is the ray-tracing and the right is the measured data with the ray-tracing model shown as red lines.

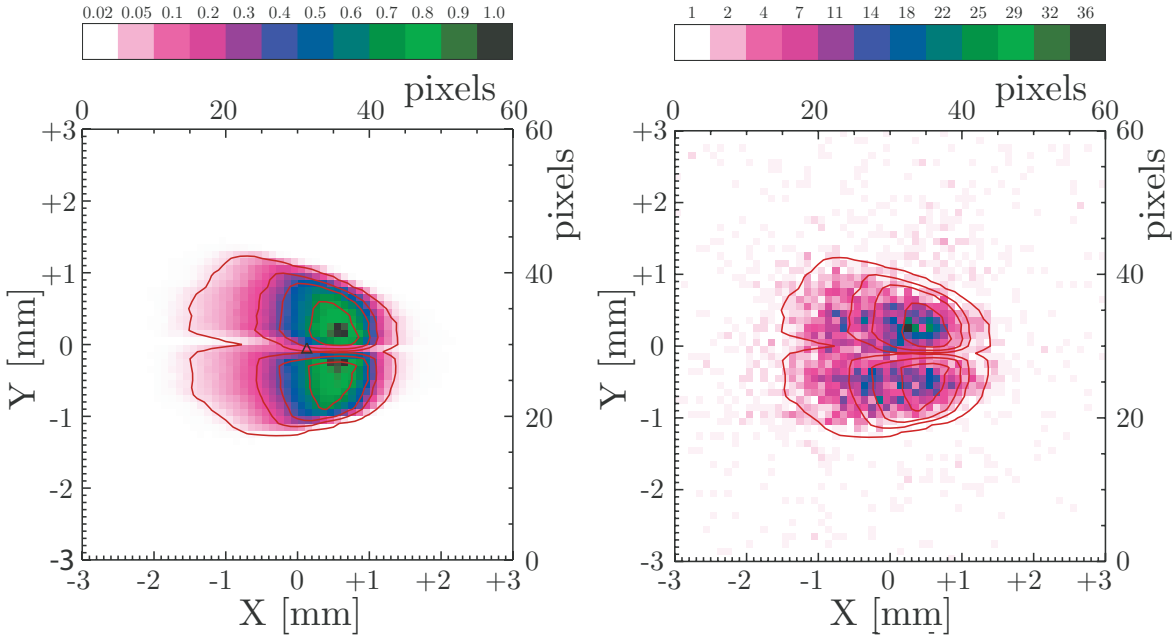

Figure 4.32: Comparison of ray-trace model with measurement using the COOL-X X-ray source. **Left:** Ray-tracing simulation considering a 6 mm source 14.2 m from the optic. **Right:** Measurement over 5 hours using the COOL-X X-ray source. White contours are from ray-tracing simulation. (From Michael J. Pivovaroff, LLNL)

Using the same model, a ray-tracing was done using a 3' source to mimic the helioscope looking at the sun and having axions converted into X-rays in the magnet. In figure 4.33 can be seen two ray-tracing models with a 3' source. Left plot assumes optic figure error of 1' (similar to NuSTAR) and right plot assumes optic figure error of 1.3'.

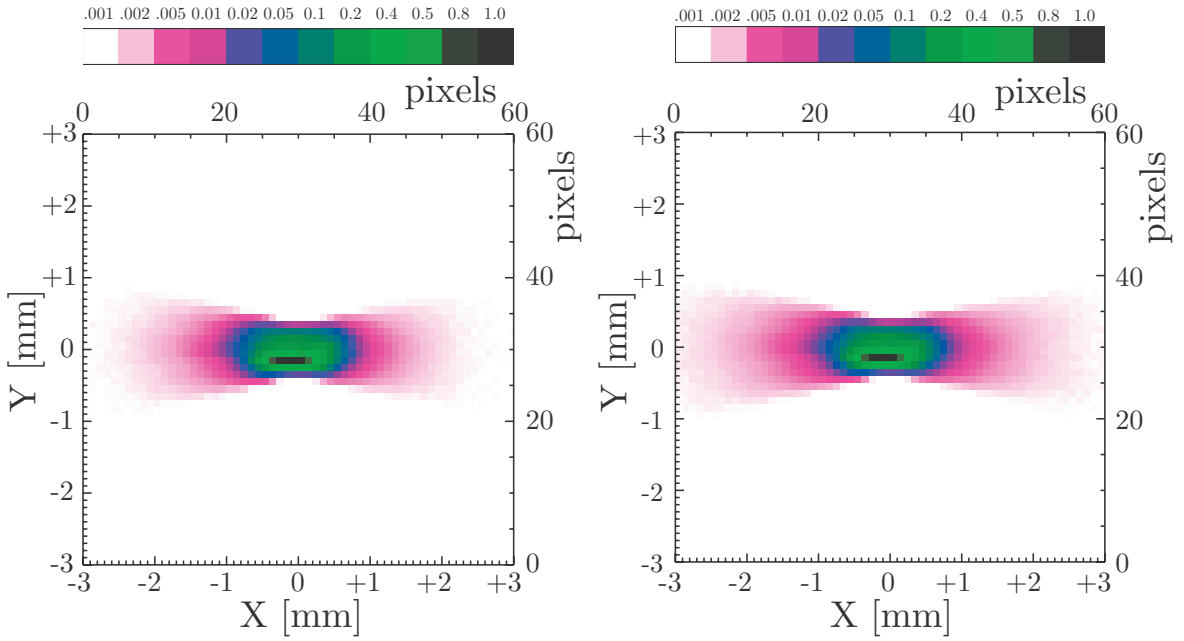

Figure 4.33: Ray-trace model of CAST XRT considering the sun as a 3' source. **Left:** Ray-tracing simulation considering optic with a figure error similar to NuSTAR of ∼1'. **Right:** Ray-tracing simulation considering optic with a figure error 1.3 times greater than for NuSTAR (∼1.3'). (From Michael J. Pivovaroff, LLNL)

The ray-tracing models show a half-power area of 8.6 mm^2 for the COOL-X X-ray source simulation , which corresponds well with the measurements seen in figure 4.32 (right). The measurements only lasted for 5 hours, so the photon count was relatively small because of the low flux from the source that actually reached the optic. The ray-tracing for a 3' source mimicking the sun show a half-power area of 1.44 mm^2. Had the optic figure been perfect (0'), the half-power area would be 1.39 mm^2, so the CAST XRT is close to the optimal performance.

In figure 4.34 can be seen the ray-tracing model computed for the as-designed multilayer coating (fig. 4.10) compared to the actual XRR measured and fitted multilayer coating (figures 4.21–4.25). The as-coated multilayers differ in reflectivity response from as-designed multilayers by up to 0.5% at the higher energies, at mid and lower energies the difference is less than 0.1%. At higher energies, the effective area of the CAST XRT is $< 10^{-1}$ cm^2 so changes in effective area become more pronounced.

4.6 CAST conclusion

In this chapter was shown the creation of an X-ray optic from design phase to installation. The whole process was ∼2 years from start to finish and realised on a minimal budget with surplus materials and instrumentation where possible.

The measurement results obtained using the COOL-X X-ray source combined with ray-

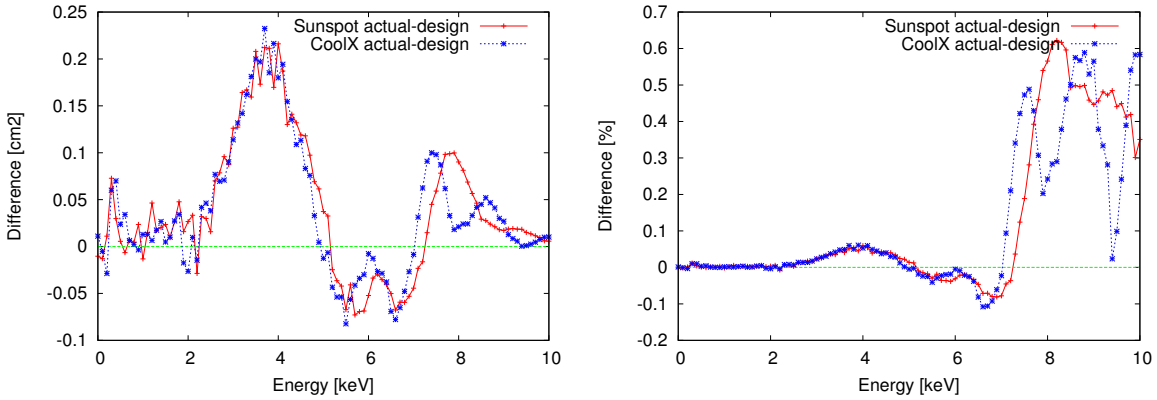

Figure 4.34: Difference in the ray-trace model between as-designed multilayer coatings and actual XRR measured and fitted multilayer coatings. **Left:** Difference in cm^2. **Right:** Difference in % from actual effective area. (From Michael J. Pivovaroff, LLNL)

tracing simulations, show that surplus slumped glass can be re-purposed into well-behaving X-ray optics for specialised tasks.

It was shown that a customised software solution interfacing to IMD can find the optimal geometry for a specific X-ray optic and make comparisons of best recipe material combinations. The specially designed software can make a full computation with a wide range of material combinations and multilayer coating geometries within 2-3 days using a regular desktop computer. Using a calculation of the overlap between optic opening and magnet bore opening, a precise effective area can be calculated with the software.

A discussion of possible improvements in the software can be found in the following section.

4.6.1 Improvements to the software

The software is limited by the inability of IMD to use more than one core on common multicore CPUs that is found in most computers today. The limit can be circumvented by letting the software spawn an instance of IMD for every processor core. That could be done by separating the calculations of each recipe, so e.g. four cores can calculate four recipes at the same time. The challenge is however to let each subprocess return the calculated optimised recipes without interrupting another subprocess. It would also require the same number of IDL instances run at the same time on one computer. This can be done using the Python `subprocess.Popen` class. An example is given here. The first Python script imports the Popen procedure and spawns an instance of Popen that opens the file `subp.py` in Python and that is called `process1`. Popen can be set to pipe back output from `process1`, but that will make the script wait for the output from the first instance before spawning the second instance called `process2`. This script will simply open subp.py in two separate instances of Python and then quit.

```
from subprocess import Popen

process1 = Popen(['python', 'subp.py', '-d'])

process2 = Popen(['python', 'subp.py', '-d'])
```

The contents of `subp.py` can be seen below. It imports `pidly`, which is a class that facilitates communication between Python and IDL. It then spawns an instance of Pidly called `idl` (that also opens IDL), and using the `idl` instance, commands can be piped directly into the IDL application. It can also run IDL procedures (`*.pro`-files) or start an IMD terminal in that instance (`.r IMD`).

```
import pidly

idl = pidly.IDL()
idl('for i=0, 100000 do begin & a=sqrt(i/255)')
```

The example given above will use 100% of two cores in a multi-core CPU, and is a very simplistic form of multi threading. The output from each instance of IDL can be written to files on the hard drive and read by the main Python program when the IDL computation is done. That can be done in a brute force manner by simply letting the main Python program wait until the number of IDL instances running on the computer is zero. That works well if each computation takes roughly the same time, but a more advanced approach can be taken in other cases, where Python will open a new process whenever a CPU core becomes available. The two Linux Bash commands below will get the number of CPU cores in the system and the number of IDL instances running, respectively. The second line will also count itself as a program running that is called something with `idl` in the name, which should be accounted for.

```
$ cat /proc/cpuinfo | grep -c cpuid

$ ps a | grep -c idl
```

In codebases where new instances of `Popen` are spawned rapidly and output files are read in between, the main process should run on its own CPU core. Otherwise a bottleneck will occur where the main program is slowed by subprocesses taking over system resources and new subprocesses will not be spawned fast enough.

Apart from speed improvements, the software is made with lower energy X-ray optics in mind. Specifically, it is limited to linearly graded multilayers, where for higher energy (10+ keV X-rays) the optimal choice would be a power-law grading. In that case, the variables to optimise would be a, b, and c in the power law $d_i = a/(b+i)^c$ and the number of layers, N.

Chapter 5

Telescope design for the International AXion Observatory (IAXO)

CAST is a third generation axion helioscope and was the first experiment to surpass the astrophysical limit on the axion-photon coupling of $g_{a\gamma} \lesssim 10^{10}$ Gev^{-1} in a broad axion mass range. The CAST helioscope search has reached slightly into the part of parameter space predicted by models to be most likely to detect the axion.

To improve on the CAST achievements and reach further into the *axion band* of the parameter space, a more sensitive instrument is required.

5.1 IAXO concept

Considering that the probability of converting a solar axion into a photon in a magnet with magnetic field B and length L is given by[66, 65, 70]:

$$P_{a\gamma} = 2.6 \cdot 10^{-17} \left(\frac{B}{10\ \mathrm{T}}\right)^2 \left(\frac{L}{10\ \mathrm{m}}\right)^2 (g_{a\gamma} \cdot 10^{10}\ \mathrm{GeV})^2 \mathcal{F}, \tag{5.1}$$

where $\mathcal{F}$ is the coherence length:

$$\mathcal{F} = \frac{2(1-\cos qL)}{(qL)^2} \tag{5.2}$$

and q is the momentum transfer. It becomes apparent that in order to improve on the probability of axion-photon conversion, either B or L has to be improved. In CAST $B \leq 9$ T, and it is already the limit of what is achievable with a large superconducting magnet.

The magnet could be made longer, but it also has to be able to point at the sun and the improvement will only be a factor of two for a magnet twice as long. The last possibility is to increase the collecting area of the magnet, so instead of two bores of 43 mm diameter like in CAST, bore diameter could be prioritised over magnetic field. An optimal design for a new magnet was identified[71] in the ATLAS magnet for LHC[72], since it achieves a much larger cross section area by having much larger bores.

Using the toroidal design of the ATLAS magnet, a proposed design gave a magnet 25 m long with a peak magnetic field of $B \leq 5.4$ T. Using eight one meter wide and 21 m long racetrack coils. The magnet bores would be each 600 mm diameter and could be placed either inside the coils or between them. A higher magnetic field could be achieved by placing the bores inside the coils, but the coils would themselves block converted X-ray photons from reaching the detector (fig. 5.1). Eight magnet bores of 25 m length, 600 mm diameter and $B \leq 5.4$ T, would equal approximately the same BL as CAST, but achieving a cross section area of ~ 2.3 m^2 compared to $3 \cdot 10^{-3}$ m^2 for CAST.

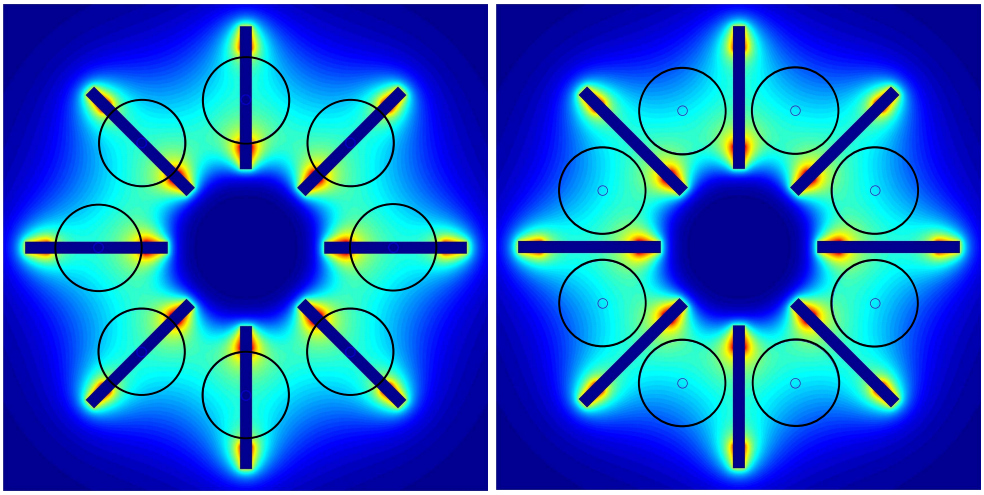

Figure 5.1: Illustration of the bore configurations with respect to superconducting coils in the IAXO magnet. Having the bores inside the coils (a) will give a stronger magnetic field, but X-ray telescopes at the end of each bore will be blocked in the center by the coil. With the bores between the coils (b), the magnetic field is not as strong, but the entire bore cross section area is usable. From [73].

The large cross section will require X-ray telescopes to focus converted X-ray photons into detectors, as low-background detectors with such a large collecting area would not be possible. A design of the IAXO helioscope[74, 75, 76] with X-ray telescopes at each magnet bore can be seen in figure 5.2. The proposed design of IAXO can achieve much higher inclination than CAST ($\pm 25^o$ vs. $\pm 8^o$), so will be able to follow the sun for longer periods ever day.

IAXO will be able to achieve a sensitivity five orders of magnitude better than CAST, which translates into $g_{a\gamma}$values as low as $\sim 5 \cdot 10^{-12}$ GeV^{-1} for axion masses up to $\sim$0.01 eV, as can be seen in figure 5.3. The experiment would explore deep into the ALP[1] and axion parameter space, and even without detection would exclude a large region of QCD axion

[1] Axion-like particle

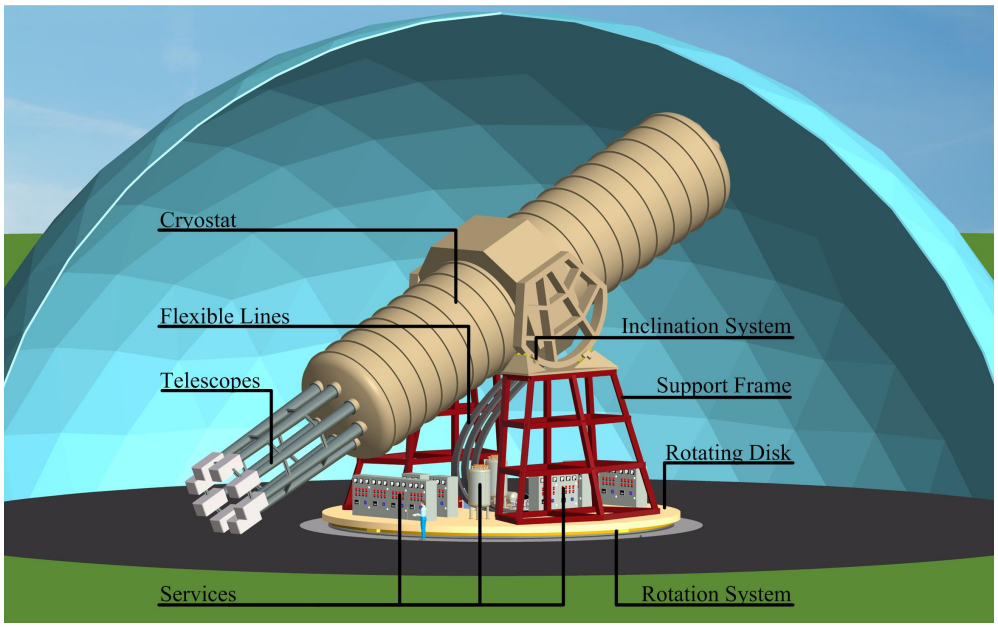

Figure 5.2: Schematic view of the IAXO helioscope. The cryostat containing the toroidal superconducting magnet is placed on a turret with complete 360° of rotation. Eight telescopes with separate detectors are placed at the end. Flexible lines feeds the magnet with liquid He and power. A fixed dome can cover the whole experiment as axions will not interact with the walls. From [64].

phase space that is completely unexplored. A detection of any fundamental pseudo-scalar particle would be groundbreaking for particle physics.

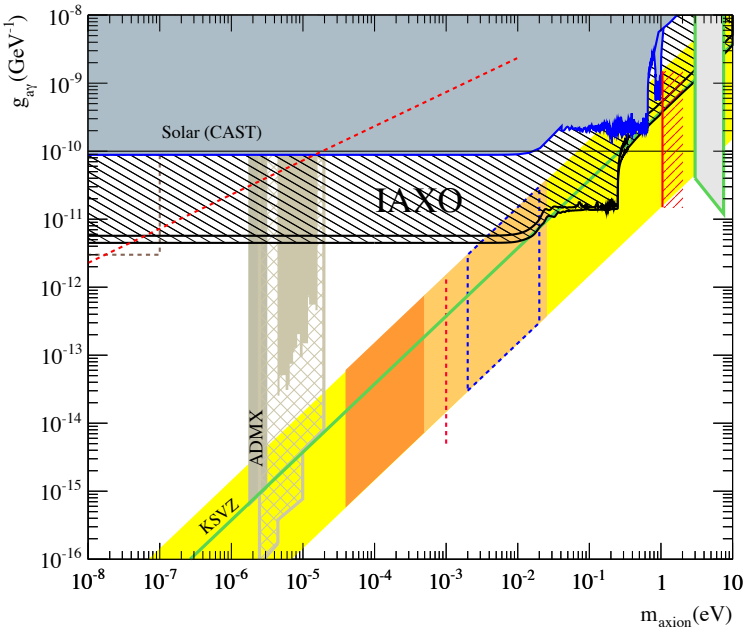

Figure 5.3: The expected sensitivity of IAXO with currently excluded regions by CAST and ADMX[77] shown. Refer to fig. 4.2 for labels of the various regions. From [73].

5.2 X-ray telescope design

In appendices D, and to some extent C, the design of X-ray telescopes for IAXO is described in detail. Using a modified version of the software developed for the CAST optic, a geometry for a NuSTAR-like optic was found.

The IAXO helioscope will be without the limitations in telescope focal length found in the CAST experiment. The design of the telescope should however take into consideration the focal spot size resulting from the optic figure error and angular size of the sun. A longer focal length will increase the throughput of the optic, but will also increase the spot size. An algorithm for optimising the focal length was developed, and a 5 m focal length was found to be the optimal solution.

An additional outcome of the shorter focal length is the easier production demands as a result of fewer glass substrate layers in the optic. A 10 m focal length would require 235 glass substrate layers, compared to 133 layers for NuSTAR which has a similar focal length but only 400 mm diameter. With eight telescopes, that would result in $\sim 8,000 \cdot 8 = 64,000$ glass substrates for IAXO, which is a large undertaking considering that the coating of $\sim 6,000$ glass substrates for NuSTAR took a year full time at the DTU Space coating facility. The 5 m focal length would only require 110 glass substrate layers; it would also put less demand on the structure of vacuum tubes going from telescopes to detectors (see figure 5.2).

5.3 Coatings for IAXO X-ray telescopes

Eight telescopes with 110 glass substrate layers is still a large undertaking for the coating chamber at DTU Space. The coating of all glass substrates would not be achievable in the 2.5 year time span set by the Letter of Intent[73] submitted to CERN in 2013. New coating chamber(s) would be needed and a year is set aside for the setup of new coating facilities before production begins.

For a large-scale coating production on curved glass substrates, a departure from the design of the coating facility at DTU Space is required. One of the main drawbacks is the inability to change samples for coating without opening the chamber completely. After closing the chamber with new samples inside, five to six hours of pumping is required in order to achieve the base pressure of $\leq 2 \cdot 10^{-6}$ Torr. A NuSTAR like coating that takes 12 hours to coat, requires 18 hours after samples are put into the chamber before they are completely coated. A load lock system would be able to almost remove the pump-down time.

The coatings for IAXO are similar to CAST and Athena coatings, 5–15 bilayers of 5–20 nm d-spacing, so each coating is relatively quick. The coating chamber at DTU Space has a rotational geometry, an advantage when coating many (> 100) bilayers, but that is not required for IAXO. Instead it is advantageous to make a linear coating system, where

substrates are placed on ∼60x60 cm^2 horizontal sample holder plates and the plates are stacked in a hopper-like system. A hopper with 10 plates each holding 6–8 samples could be placed in a load-lock and the system would automatically take out the plates to be coated one at a time. The plates would move horizontally past a number of cathodes, where one layer would be deposited on the way out and one layer on the way back, resulting in one bilayer per return trip. Each plate can be applied a different coating based on the velocity of the plate across the cathode plasma and the cathode power setting. The number of bilayers is set by the number of return trips of a plate.

The cathodes should be linear magnetrons of ∼80 cm length, placed horizontally and pointing down. Increased uniformity of coating on the cylindrically curved substrates that would be used for IAXO can be achieved by measuring the curvature of each sample in the chamber immediately before coating using a distance sensor. The cathodes could then automatically increase/decrease power as the samples move by according to the curvature of each sample.

Using two chambers of the design proposed above, the ∼30,000 substrates can be coated within the two year time span set by the Letter of Intent.

5.4 IAXO conclusion

In this chapter was described shortly the considerations taken in the design of X-ray telescopes for IAXO. Using a modified version of the software used to design the CAST XRT, telescopes suitable for IAXO were designed and an optimal focal length of 5 m were found.

IAXO is an international collaboration involving 29 institutes from across the world, each playing a part in the design, construction and operation of the experiment. The main barrier at the time of writing is the funding of the ∼100M € experiment, but both European and American institutions and agencies have expressed their interest in the project.

The Letter of Intent for IAXO, submitted in 2013, was approved by CERN in spring of 2014 making IAXO an official experiment at CERN. The IAXO collaboration was encouraged by CERN to take the next steps toward a technical design report that would include R&D on magnet, detectors and X-ray telescopes.

Chapter 6

Conclusion and outlook

In this thesis I have described investigations into grazing angle type X-ray optics for astrophysics and astroparticle physics, in particular I have during the PhD study worked with the following:

1. Developed new software to control the coating chamber at DTU Space.
2. Characterised and qualified coatings for the European Athena mission.
3. Investigated production facility requirements to coat flight substrates for Athena.
4. Designed, produced and installed an X-ray telescope for the CAST helioscope at CERN.
5. Designed X-ray telescopes for the proposed International AXion Observatory (IAXO).

In the first chapter of the thesis I have described the coating facility at DTU Space and the former software solution used to control the multilayer coating deposition process for the past decade. A number of features were missing in the old software, such as continuous logging and customisation options. A new software solution was produced using the SPEC package to address the missing features. At the time of writing, the software has been controlling the chamber for $\sim$1 year and been capable of producing complicated NuSTAR-like coatings as well as several coatings in a single run while varying e.g. power supply pulse frequency or chamber pressure. A continuous log of chamber pressure and power supply output is updated every 5 seconds and kept on the computer. A webpage has been set up to show plots of pressure and power output for the preceding three days and is accessible from any internet-connected computer.

Investigations into baseline and optimised coatings for the Athena mission led to a characterisation of the B_4C-based multilayer material combinations Pt/B_4C, Ir/B_4C and W/B_4C. Long term storage investigations showed instabilities in Pt/B_4C and W/B_4C at ambient conditions, where interdiffusion and reaction to humidity changed the multilayer structure over time. Ir/B_4C baseline and optimised multilayer coatings showed complete stability in the qualification tests.

Deposition of coatings using pulsed-DC sputtering and reactive sputtering were investigated for the Athena mission. The two methods showed no improvements in interlayer roughness. Coatings of a single iridium layer with chromium sublayer has shown a significant improvement in iridium surface roughness compared to the Ir/Cr interface roughness.

To scale production of coated SPO substrates to the 210,000 needed for Athena within a 2 year timespan, possible manufacturing methods were investigated. A solution with 2-3 multi chamber sputtering instruments were found to be the optimal solution to meet the requirements.

An X-ray telescope was designed for the CAST helioscope using custom software to find optimal geometry and reflective multilayer coatings, taking into account the detector quantum efficiency and axion spectrum. Surplus NuSTAR glass substrates were coated with optimised multilayer coatings, which were subsequently assembled into a Wolter I type telescope at Lawrence Livermore National Lab. The telescope was installed on the CAST helioscope at CERN and aligned using a theodolite and a gun-sight construction on the optic. Lastly, a pyroelectric X-ray source was used to check the alignment of telescope and detector; the resulting detector output matches a ray-tracing calculations of the setup.

The software used to design and optimise the CAST X-ray telescope was repurposed to design telescopes for IAXO. An optimal focal length of 5 m for the telescopes was found by taking the estimated telescope figure error and angular size of the sun into account. Producing coated substrates for IAXO requires a different approach than Athena due to the substrates being curved instead of flat. A method and possible design of a coating chamber has been described; the coating non-uniformity due to substrate curvature being addressed with a distance sensor in the coating chamber.

6.1 Outlook

A natural extension of the work described in this thesis would be further investigations into the ability of iridium coatings to mitigate the roughness of the Cr/Ir interface underneath. A rough chromium surface might not be necessary for iridium to mitigate roughness, so it could be used to improve surface roughness on substrates. Both SPO substrates and NuSTAR glass substrates have a surface roughness of $\sigma_{rms} \approx 0.45$ nm, which traditionally limits the coatings deposited on top to have $\sigma_{rms} \geq 0.45$ nm. To make new telescopes that reach higher energies than NuSTAR, the interface roughness should significantly decrease in order create multilayers with thinner d-spacings and abiding the rule of thumb $\sigma_{rms} \leq d/6$. A great contender for soft gamma-ray focusing is the WC/SiC material combination that can reach an interface roughness of $\sigma_{rms} \leq 0.15$ nm using an ultra-flat and highly polished quartz substrate. Such a quartz substrate coated with a WC/SiC multilayer with d-spacings of 1.5 nm have shown Bragg reflections up to 635 keV at the ID15 beamline at ESRF[78, 79]. To apply those coatings to the current flight mirror technology of either SPO substrates or NuSTAR glass substrates requires a method to reduce the surface roughness, and the roughness mitigating qualities of iridium might be the answer.

One major obstacle in obtaining precise multilayer coatings on curved glass substrates is the non-uniformity that comes as a result of the glass curvature. I believe the problem can be overcome by having the cathode power supply be output adjusted as the substrate passes by the cathode, with the adjustment corresponding to the glass curvature. The cathode power supplies at DTU Space can be output adjusted on an analog input port on the back of each power supply by varying the input voltage on that port between 0-10 V.

The X-ray telescopes worked on during this PhD are in completely separate stages of development and deployment. The CAST helioscope has been upgraded with the X-ray telescope and a one-year measurement campaign has begun. It is the hope of the collaboration that a detection will be seen with the new upgrade. Unfortunately the helioscope will likely be decommissioned at the end of 2015, but the telescope has already worked as a proof of concept for the IAXO X-ray telescopes. The Athena mission was selected for a 2028 launch, and with an estimated 10 years required to build it, the European Space Agency is hard at work defining the production facilities required for the optic.

Appendix A

Preliminary coating design and coating developments for Athena

Preprint

Preliminary coating design and coating developments for ATHENA

Anders C. Jakobsen[a], Desiree Della Monica Ferreira[a], Finn E. Christensen[a], Brian Shortt[b], Max Collon[c], Marcelo D. Ackermann[c]

[a]DTU Space, Juliane Maries Vej 30, 2100 Copenhagen Ø, Denmark);
[b]European Space Research and Technology Ctr. (Amsterdam, Netherlands)
[c]Cosine Research B.V. (Leiden, Netherlands)

ABSTRACT

We present initial novel coating design for ATHENA. We make use of both simple bilayer coatings of Ir and B_4C and more complex constant period multilayer coatings to enhance the effective area and cover the energy range from 0.1 to 10 keV. We also present the coating technology used for these designs and present test results from coatings.

1. INTRODUCTION

In this paper we investigate the possibility of increasing the ATHENA telescope effective area in the range between 0.1 and 10 keV. We studied the performance of five different material combinations, W/Si, Ir/B_4C, Pt/C, Pt/B_4C and Mo/Si, considering a simple bilayer, simple multilayers and linear graded multilayers. To reduce stress in the Ir/B4C coating, we investigated the need of a third stress reducing material as an undercoat to the Ir/B4C bi-layer.

The ATHENA mission consists of two identical telescopes with fixed focal planes, the first containing a calorimeter spectrometer and the second a wide field imager. The ATHENA focal plane is of 11.5 m, the telescopes innermost radius of 0.15 m and outermost radius of 0.90 m. The operational energy range is from 0.1 to 10 keV.

The coating recipe adopted as baseline is a bilayer with an 8 nm layer of B_4C on top of a 10 nm Ir layer. The same coating is adopted for all mirror modules at all radii.

2. OPTIMIZING ATHENA COATING DESIGN - PRELIMINARY RESULTS

2.1 Low energy range

The choice for radii division and coating recipes is based on the need of optimization at different energy ranges. The use of a simple bilayer coating is appropriate for energies lower than 5 keV, while to improve the telescope performance above 5 keV the use of multilayers is required.

The telescope radius where simple bi-layers should be applied is considered to be the radius at which the reflectance of the Ir/B_4C baseline coating at 6 keV is above 30%. This is a somewhat arbitrary choice and considered as a good starting point for investigation. This radius corresponds to the seven innermost rows of mirror modules, see figure 1. The optimization of bi-layer coating is performed for this region (radius between 0.15 m to 0.59 m).

The criterion applied for the choice of a simple bilayer coating material is based on the coating performance at 1 keV and 6 keV considering the seven innermost rows of mirror modules.

We computed the best coating thickness for each material combination in order to maximize the effective area at 1 keV and 6 keV. The surface roughness considered is 0.65 nm for Ir/B_4C, and 0.45 nm for W/Si, Pt/C,

Further author information: (Send correspondence to A.C.J.)
A.C.J.: E-mail: jakobsen@space.dtu.dk, Telephone: +45 3532 5735
D.D.M.F.: E-mail: desiree@space.dtu.dk, Telephone: +45 3532 5734

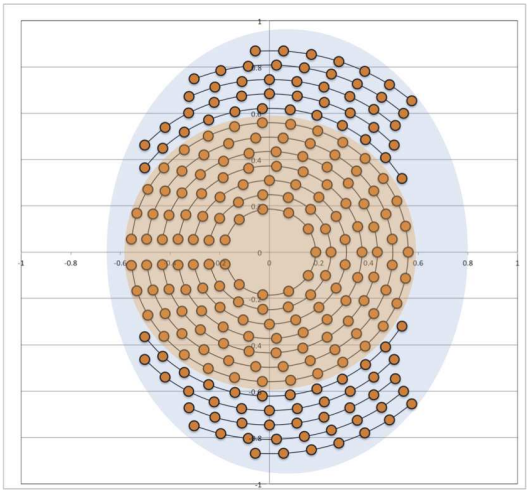

Figure 1. Diagram of one of two telescope optics for ATHENA. Each orange circle represents a mirror module with 68 coated SPO substrates. The inner part chosen for simple bilayer/trilayer and outer part chosen to carry a multilayer with cap layer and top layer.

Pt/B_4C and Mo/Si. We observe that Pt/B_4C presents superior effective areas at both energies, followed by Ir/B_4C.

Because the material combination of Pt/B_4C is still unknown at the present time, and properties such as roughness and stress need further investigation, Ir/B_4C is considered as the best option for a bi-layer coating.

We investigate the best layer thickness to maximize the on-axis effective area at 6 keV considering a Ir/B_4C coating. As the effective area scales with the reflectivity square, we base our study on the reflectivity curve computed at this energy. To optimize the Ir/B_4C coating we vary the thicknesses of Ir and B_4C and compute the on-axis effective area at 1 keV and at 6 keV. We list the parameter combinations that provide maximum effective area at those energies and parameter combinations resulting in 99% and 95% of the maximum effective area. The best parameter combination provides minimal loss of on-axis effective area on both energies. Based on the on-axis effective areas at 1 keV and 6 keV and on the layer thickness we find that the baseline (10 nm Ir, 8 nm B_4C) is the optimum choice.

2.2 Mid energy range

At radii beyond the seven innermost mirror module rows (0.59 m) the bi-layer reflectivity is inefficient at energies above 6 keV. To enhance the telescope effective area at the energy range from 5 to 10 keV, we suggest a multilayer coating approach for the 5 outermost mirror module rows.

Also here the material choice is defined by evaluating the on-axis effective area at 6 keV for this region (0.59 0.90 m). We consider a simple multilayer coating for the same materials listed above, a cap layer of the heaviest material and an 8 nm overcoat of B_4C to account for the energies below 1.5 keV. The surface roughness applied is 0.65 nm for Ir/B_4C and 0.45 nm for the remaining material combinations.

The parameters considered in the computation are: number of bi-layers, thickness of the bi-layers, ratio between heavy and light material thickness and thickness of the extra layer of the heavy material. The best parameters for each material choice return maximum on-axis effective area at 6 keV.

Applying a multilayer of W/Si results in the best performance considering the criterion above with the second best options being Pt/B_4C and Pt/C with equivalent performances. The material combinations Pt/B_4C and Pt/C return on-axis effective areas that differ from the computed for W/Si by only 2%. There are several reasons for choosing Pt over W, e.g. the absorption edges around 1-2 keV, and those aspects are under investigation. At this point we proceed with the optimization of the telescope outermost rows considering W/Si as the best material choice for multilayer coating.

2.3 Multilayer optimization

The actual ATHENA coating baseline presents optimal performance at energies below 5 keV but the use of multilayers in the outer mirror module rows can increase the telescope effective area at energy range 5 to 10 keV. The optimum coating design so far is a bi-layer of Ir/B_4C with thickness of 10 nm and 8 nm respectively, applied to the seven innermost mirror module rows. The remaining five outermost rows are optimized considering multilayers of W/Si with a W cap layer and an 8 nm B_4C overcoat.

To optimize the coating design at the telescope outermost region we considered five different coating recipes, one for each row. The motivation for this choice is the need of a smooth effective area curve at the scientifically interesting region around 6 keV.

A linear graded multilayer is chosen over a simple multilayer in order to optimize a wider energy range. The design for optimization is therefore a linear graded W/Si multilayer with a W cap layer on top of the multilayer and an 8 nm B_4C overcoat. The B_4C overcoat is optimized for best performance at 1 keV and is therefore set to 8 nm.

For each row in the region between 0.59 m and 0.90 m an optimal coating recipe is computed in order to maximize the effective area in the region around 6 keV without compromising the effective area at lower energies. This is achieved by evaluating the several possible parameter combinations that result in the maximum integrated effective area over energy for the energy range between 3 keV and 8 keV with the condition that the loss of effective area between 1.5 and 5 keV is minimal. To achieve that we look at how the gradient of the on-axis effective area changes over the energy range between 3 keV and 8 keV and look for solutions returning maximum effective area with minimum gradient, i.e. the curve should be as flat as possible. This approach is preliminary and alternative choices for the figure of merit are being investigated.

The parameters considered in this computation are: Number of W/Si bi-layers (n), thickness ratio between W and Si (Si-Γ), minimum bi-layer thickness (d_{min}), maximum bi layer thickness (d_{max}) and thickness of the W cap layer (d_W) (to accommodate the energies between 1.5 keV and 5 keV). The parameters were varied considering steps of 10 bilayers, 0.1 for Si-Γ, 0.5 nm for d_{min} and d_{max} and 1 nm for d_W.

The best parameters for each row are listed in table 1. The optimized effective area over energy is shown in figure 2. The comparison between the baseline performance at 1 keV and 6 keV is shown in table 2.

Row	n	Si-Γ	d_{min} [nm]	d_{max} [nm]	d_W [nm]
8	10	0.5	5.5	7.5	8.0
9	10	0.5	5.0	7.5	8.0
10	20	0.6	4.0	7.0	7.0
11	30	0.7	3.5	6.5	6.0
12	20	0.6	4.0	6.5	6.0

Table 1. Optimized coating design for the outermost mirror module rows of ATHENA assuming a linear graded multilayer

	Baseline	Optimized
A_{eff} at 1 keV [m^2]	1.146	1.152 (+0.4 %)
A_{eff} at 6 keV [m^2]	0.431	0.454 (+5.6 %)

Table 2. Effective area of ATHENA. Results listed for 2 telescopes with a 10% reduction applied to account for eventual losses due to e.g. alignment and particle contaminations.

3. SILICON PORE OPTIC SUBSTRATES

The optics of ATHENA will consist of >60,000 Silicon Pore Optic (SPO) mirror substrates.[1] Each substrate is cut from a wafer in sizes of 66 mm x 66 mm and have grooves cut into the bottom side so the substrate gets thin ribs, which gives the substrates the ability to be stacked directly on top of each other. The top surface of the substrate is treated with a SiO_2 wedge with a specific slope so each SPO substrate has the right angle to the focal plane.

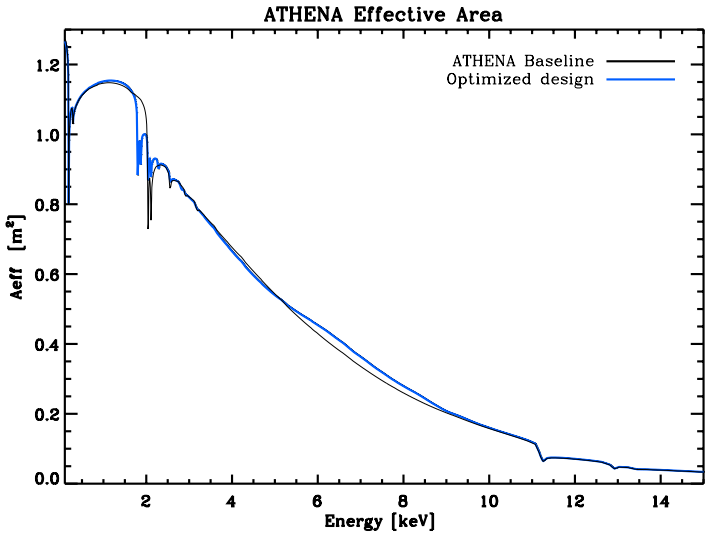

Figure 2. ATHENA optimized design and baseline. Results listed for 2 telescopes with a 10% reduction applied to account for eventual losses due to e.g. alignment and particle contaminations.

The stacked plates are bonded using direct Si-Si contact, which requires part of the surface of every substrate to be free of coating so the ribs can have direct contact to the Si wafer surface. During DC Magnetron sputtering the entire surface is coated, unless a mask is used during coating to shield part of the substrate from incoming sputtered atoms. This has previously been investigated, but the alignment of a mask for every substrate is a very cumbersome task, especially for more than 60,000 substrates.

Another solution is to use a striped resist layer, which can be removed along with any film deposited on top after coating. An example of that can be seen in figure 3, where a Ir/B_4C bilayer is deposited on a SPO substrate with a resist layer. The resist along with film is removed after coating using acetone and results in a substrate with bare Si-substrate stripes so another SPO substrate can be stacked on top.

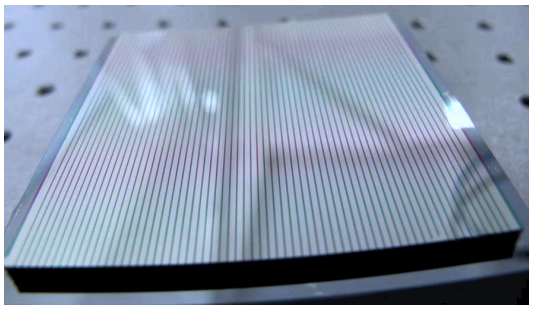

Figure 3. A coated Silicon Pore optic substrate with coating removed in a striped pattern using a resist layer.

To achieve a clean separation of coated film from the substrate in the specified striped pattern, the sputter deposited thin film needs a good adhesion to the areas of the substrate without resist layer. One factor that can be connected to bad adhesion is stress in the thin film, and the Ir/B_4C bilayer films have a compressive stress of >4 GPa during preliminary coating tests at DTU Space.

4. REDUCING STRESS IN IRIDIUM / BORON CARBIDE BILAYERS

To reduce the stress in Ir films, we use of Cr as an underlayer between substrate and Ir. It can decrease and even remove the film stress completely. The addition of a B_4C toplayer complicates the interaction, as sputtered

B_4C films are stressed.

Investigations into the stress reducing ability of Cr on Ir/B_4C bilayers are done, with a further emphasis on the possible change in surface roughness when a Cr underlayer is introduced.

5. EXPERIMENTAL

Sample substrates were coated at DTU Space using a DC Magnetron sputtering chamber.[2] The substrates were mounted in the chamber between two 50 mm deep separator plates with a distance of 100 mm (see figure 4). The separator plates reduce roughness by collimating incoming sputtered atoms, so the amount of sputter atoms coming at a low angle to the substrate surface is decreased.

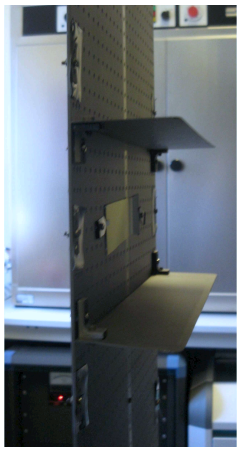

Figure 4. Side view of a mounting plate in the sputtering chamber. A Si wafer substrate is mounted in the middle between two seperator plates.

Each specific film is coated on both a 20x80 mm Si wafer piece with a surface roughness of $\sigma_{\mathsf{rms}} = 0.25$ nm for X-ray reflectometry measurements and a 5x70 mm Si wafer piece for stress measurements. All large Si wafer pieces are measured with a 8 keV Cu-K_α rotating anode at DTU Space and the data is fitted using IMD[3] to determine the geometry of the coated film. The smaller Si wafer pieces were measured before and after coating using a Dektak 150 stylus measurement device, that measures the deflection of a sample and calculates the stress of a coating based on film thickness and difference in deflection before and after coating.

Two sample sets were created, each with eight different coatings as seen in table 3.

Sample	1	2	3	4	5	6	7	8	9	10	11	12	13	14	15	16
d_{Ir} [nm]	∼7	∼7	∼7	∼7	∼7	∼7	∼7	∼7	∼7	∼7	∼7	∼7	∼7	∼7	∼7	∼7
d_{B_4C} [nm]	∼7	∼7	∼7	∼7	∼7	∼7	∼7	∼7	∼3.5	∼3.5	∼3.5	∼3.5	∼3.5	∼3.5	∼3.5	∼3.5

Table 3. Overview of samples coated with Ir and B_4C.

6. DEVELOPMENT RESULTS

Figure 5 presents results from stylus point deflection measurements, with the left plot showing the change in stress with changing Cr thickness for $d_{Ir} \approx d_{B_4C} \approx 7$ nm. The right plot shows the change in stress with changing Cr thickness for bilayer films with $d_{Ir} \approx 7$ nm and $d_{B_4C} \approx 3.5$ nm. Each sample are represented as two dots, as both a compressive and tensile stress can be present in the film at the same time.

In both plots a clear change in stress from compressive to tensile is seen as the Cr underlayer thickness is increased.

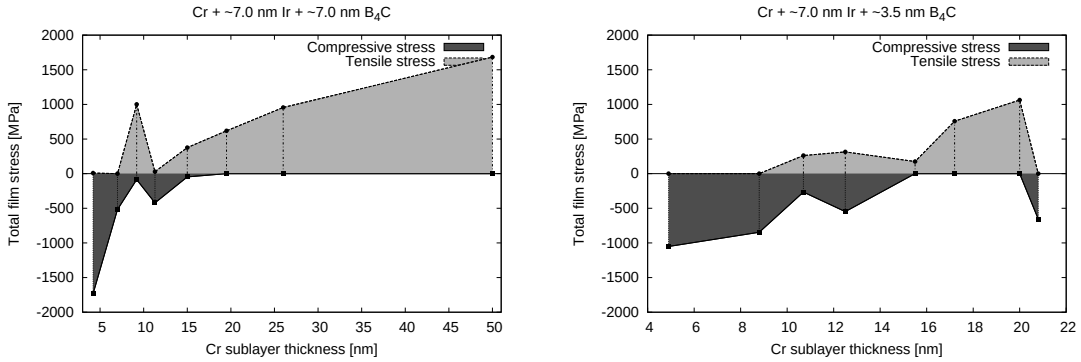

Figure 5. Plots comparing Cr thickness in a trilayer coating with the resulting total film stress. Left side compares Cr/Ir/B_4C coatings with $d_{Ir} \approx d_{B_4C} \approx 7$ nm. Right side compares Cr/Ir/B_4C coatings with $d_{Ir} \approx 7$ nm and $d_{B_4C} \approx 3.5$ nm.

The change in stress correlates with earlier investigations of Ir coatings with Cr underlayer. The stress decreases with increasing Cr thickness and the film eventually comes close to zero stress. Adding even thicker layers of Cr underneath will yield a tensile stress in the film. For Ir/B_4C bilayers of these dimensions, the film stress can be reduced to ~ 0 using a Cr underlayer with a thickness of $\sim$7 nm to $\sim$11 nm.

The data points for the left plot in figure 5 show a consistent curve going from compressive to tensile stress, except around the intersection point with 0 stress. Two samples show values outside the expected and outside standard error deviation. Further investigation in the low stress region is planned.

The right side plot in figure 5 shows several deviations from the expected values, but still a correlation can be seen. The intersection point with 0 stress is with Cr thickness of 12 to 14 nm. The decreased thickness of the B_4C layer has shown a considerable alteration of the structural properties of the film and thus requires a thicker Cr underlayer to minimize the total film stress.

Figure 6 shows X-ray reflectometry data from two different large Si wafer samples and the data is fitted using IMD. The left plot shows data from a trilayer of Cr/Ir/B_4C with relative thicknesses of 11 nm/7 nm/7 nm, the right plot shows data from a Cr/Ir/B_4C trilayer with relative thicknesses 4 nm/7 nm/3.5 nm.

The fit shows a surface roughness of Ir in the left plot of $\sigma_{\mathsf{rms}} = 0.5$ nm and for Cr $\sigma_{\mathsf{rms}} = 0.7$ nm. The surface roughness of B_4C does not affect 8 keV photons significantly in IMD simulations, so a precise value of the roughness can not be given using this measurement method. In these fits, the B_4C roughness is set to $\sigma_{\mathsf{rms}} = 0.4$ nm. In the right plot, Ir surface roughness is significantly smaller ($\sigma_{\mathsf{rms}} = 0.2$ nm) and so is the Cr surface roughness ($\sigma_{\mathsf{rms}} = 0.5$ nm).

The change in Ir roughness was expected when changing the Cr thickness. Sputtered Cr films generally have a rough surface, and the roughness increases with thicker layers. That the Ir surfaces are smoother than the Cr surfaces were not expected, as the expected lower bound for film surface roughness is the surface roughness on which the film is coated. So e.g. an Ir layer coated onto a Cr surface with roughness of 0.7 nm would also give an Ir surface roughness of at least 0.7 nm. Since this is not the case in either of the two samples, the Ir and Cr combination can be suspected to give a smoothening effect on above surfaces.

For the right side plot in figure 6, the Ir surface roughness is even lower than the Si wafer substrate surface roughness (0.25 nm). This smoothening effect could be present in Cr + Ir coatings on rougher substrates, which begs for further investigation.

As the coatings done here are deposited onto normal Si wafer substrates and not wedged SPO substrates, XRR measurements of the bare substrates were done. The measurement data can be seen in figure 7 along with fits modelled using IMD.

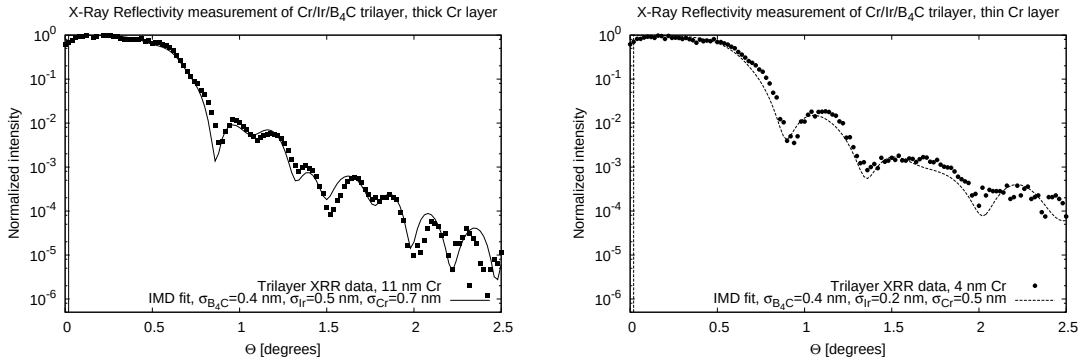

Figure 6. Plots showing X-ray reflectometry data for two different trilayer coated samples. Each data set is fitted a model from IMD to get film dimensions and surface/interface roughness values. The left side shows data from a trilayer of $Cr/Ir/B_4C$ with relative thicknesses of 11 nm/7 nm/7 nm, the right side shows data from a $Cr/Ir/B_4C$ trilayer with relative thicknesses 4 nm/7 nm/3.5 nm.

In the left plot is shown measurement data of a bare Si wafer substrate, and the IMD model fits to the data with a substrate surface roughness of $\sigma_{\mathsf{rms}} = 0.25$ nm. The plot on the right shows the measurement data for a wedged SPO substrate. The IMD model fits to the data with a substrate roughness of $\sigma_{\mathsf{rms}} = 0.45$ nm.

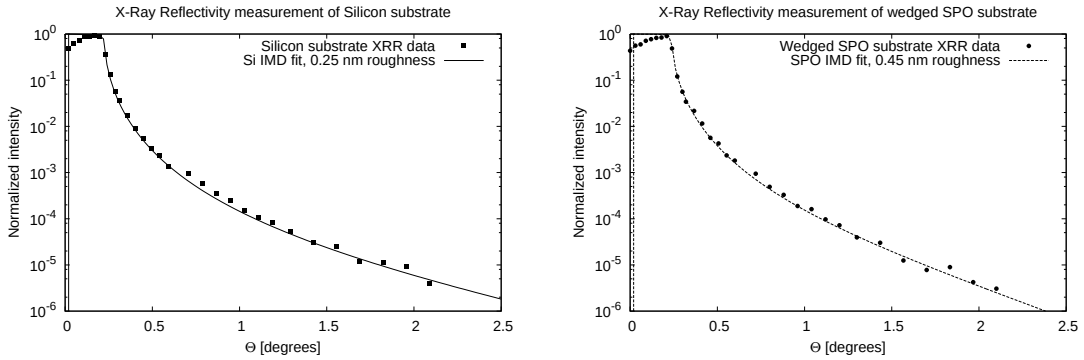

Figure 7. Plots showing X-ray reflectometry data for a bare Si wafer substrate (left side) and a wedged SPO substrate (right side). Each data set is fitted using an IMD model to get surface roughness values.

The increased roughness of wedged SPO substrates compared to bare Si wafer substrates were taken into account during the optimization procedure in section 2.1 where all surface roughness values were expected to be at least 0.45 nm.

The SiO_2 material of the wedge on the SPO substrate might yield different sputtered film properties due to different interatomic spacing in the amorphous surface. All possible coating candidates will be tested on proper wedged substrates in the next months.

7. CONCLUSION

A preliminary coating design optimization of the ATHENA optic has been shown, using an analytical approach to achieve optimum coating recipes for the outer five mirror module rows. The optimized coating uses linearly graded multilayers to increase the effective area around 6 keV by ~ 5 %.

Additionally, trilayer coatings of $Cr/Ir/B_4C$ were deposited onto Si wafer substrates to investigate film stress and surface roughness properties. A correlation between Cr thickness and film stress has been found, where a Cr

underlayer can remove most of the stress in a Ir/B_4C film. A thicker Cr underlayer to reduce stress is necessary when decreasing the B_4C layer thickness in a Ir/B_4C bilayer. Finally, XRR measurements have shown that although Cr surface is relatively high, the surface roughness of Ir layers deposited on top of Cr were consistently lower.

8. FUTURE INVESTIGATIONS

Results on coating design for ATHENA presented here are preliminary. Several aspects of the coating design optimization are undergoing further investigation and improvement. Other material combinations will be investigated as well as the possibility of changing the amount of mirror modules coated with trilayer vs. multilayers.

Work to be done in coating development includes the introduction of reactive sputtering using N_2 gas[4,5] to reduce film stress and surface/interface roughness as well as using honeycomb collimation[6] during sputtering. Film stress in multilayers and the removal of stress using Cr underlayers will also be investigated. X-ray reflectometry and X-ray scattering will be performed at BESSY. Additional measurement techniques will be used, such as cross-sectional TEM, Atomic Force Microscopy and X-ray fluorescence.

REFERENCES

[1] Wallace, K., Bavdaz, M., and Gondoin, P., "Silicon pore optics development," *Proceedings of SPIE* **7437**.

[2] Jensen, C., Christensen, F., Chen, H., Smitt, E., and et al, "Multilayer coating facility for the HEFT hard x-ray telescope," *Proceedings of SPIE* **4496**, 104–108 (Jan. 2002).

[3] Windt, D., "IMD—Software for modeling the optical properties of multilayer films," *Computers in Physics* **12**, 360–370 (Jan. 1998).

[4] Windt, D., "Reduction of stress and roughness by reactive sputtering in W/B4C X-ray multilayer films," *Proceedings of SPIE* **6688** (Jan. 2007).

[5] Bellotti, J. and Windt, D., "Depth-graded Co/C multilayers prepared by reactive sputtering," *Proceedings of SPIE* **7437** (Jan. 2009).

[6] Anette, V. and Carsten, P., "Collimated Magnetron Sputter Deposition for Mirror Coatings," *X-Ray Optics and Instrumentation* **2008** (Jan. 2008).

Appendix B

Development and characterization of coatings on silicon pore optics substrates for the Athena Mission

---

Preprint

For this paper I produced the coated substrates as well as performed XRR measurements at DTU Space and the BESSY II synchrotron in Berlin.

Development and characterization of coatings on Silicon Pore Optics substrates for the ATHENA mission

Desiree Della Monica Ferreira[a], Anders C. Jakobsen[a], Finn E. Christensen[a], Brian Shortt[b], Michael Krumrey[c], Jørgen Garnæs[d], Ronni B. Simonsen[a]

[a]DTU Space, Technical University of Denmark, Elektrovej, bygn. 327, 2800, Denmark
[b]European Space Agency (ESTEC), Keplerlann 1, PO Box 299, 2200 AG, Noordwijk, Netherlands
[c]Physikalisch-Technische Bundesanstalt (PTB), Abbestraße 2-12, 10587 Berlin, Germany
[d]Danish Fundamental Metrology Ltd., Matematiktorvet 307, 2800, Denmark

ABSTRACT

We present description and results of the test campaign performed on Silicon Pore Optics (SPO) samples to be used on the ATHENA mission. We perform a pre-coating characterization of the substrates using Atomic Force Microscopy (AFM), X-ray Reflectometry (XRR) and scatter measurements. X-ray tests at DTU Space and correlation between measured roughness and pre-coating characterization are reported. For coating development, a layer of Cr was applied underneath the Ir/B_4C bi-layer with the goal of reducing stress, and the use of N_2 during the coating process was tested in order to reduce the surface roughness in the coatings. Both processes show promising results. Measurements of the coatings were carried out at the 8 keV X-ray facility at DTU Space and with synchrotron radiation in the laboratory of PTB at BESSY II to determine reflectivity at the grazing incidence angles and energies of ATHENA. Coating development also included a W/Si multilayer coating. We present preliminary results on X-ray Reflectometry and Cross-sectional Transmission Electron Microscopy (TEM) of the W/Si multilayer.

1. INTRODUCTION

The ATHENA (Advanced Telescope for High Energy Astrophysics) mission is an X-ray observatory under study by ESA. The ATHENA mission concept consists of two X-ray telescopes, with a focal length of 11.5 m, and is based on Silicon Pore Optics (SPO)[1] mirror modules to focus incoming X-ray photons at low grazing incidence angles. In short, a SPO substrates is a ribbed and angular wedged Si wafer plate that stacks directly on top of another plate by means of covalent Si-Si bonding. Photoresist stripes are applied to the substrates as part of the masking process. Each mirror module consists of 2×68 reflecting SPO substrates, set to allow for double reflection of X-rays.

According to the current design, each X-ray telescopes onboard ATHENA consist of 33320 SPO plates. High throughput in the energy range between 0.1 and 10 keV depends critically on the performance of the mirror coatings.[2] The coating recipe adopted as baseline for ATHENA is a Ir/B_4C bi-layer and the same coating is adopted for all mirror modules at all radii.

It is important that both the SPO substrates and coatings perform optimally. The pre-coating characterization allows for assessment of the performance of the SPO substrates. A coating development campaign provides the insight on the possible process improvements to produce coatings with optimal performances.

Further author information:
Send correspondence to:
Desiree Della Monica Ferreira, e-mail: desiree@space.dtu.dk
Anders C. Jakobsen, e-mail: jakobsen@space.dtu.dk

2. PRE-COATING CHARACTERIZATION

2.1 Atomic Force Microscopy (AFM)

An atomic force microscope gives a direct image of the surface topology by raster scanning a sharp tip over the surface with a non-destructive force. The AFM measurements were carried out by Danish Fundamental Metrology Ltd. The microscope used is a metrology atomic force microscope, where the tip is scanned over the surface using piezoelectric flexures equipped with capacitive distance sensors.

The sensitivity of the capacitive distance sensors along the XY-plane is traceable to an international standard, in terms of a two dimensional grating calibrated by laser diffraction measurements. The sensitivity at the Z-direction is also traceable to a international standard in terms of a step height calibrated by an atomic force microscope equipped with laser interferometers.[3]

All AFM measurements were carried out in dynamic resonant tapping mode, using single crystal silicon cantilevers. The measurement uncertainty is estimated to be 0.1 nm for the recorded profile height. This estimate contains contributions from the calibration method, the reference standards used, the environmental conditions, and from the object being measured (e.g. deformation). The AFM measurements considered in this study are first order line wise corrected along the X-axis and are suitable for 1D PSD analysis.

2.1.1 AFM of SPO samples

The two SPO samples, with and without resist stripes, considered in this study are standard, wedged and ribbed SPO plates, measuring 65.7×65.7mm. For the sample containing resist stripes, the AFM measurement was carefully set to measure the region in between the resist stripes.

Figures 1, 2 and 3 show the AFM images of the SPO sample without resist stripes. The measurements at three different positions (spot 1, 2 and 3) are shown for image sizes of 0.1×0.1μm, 1×1μm and 10×10μm, respectively.

Figures 4, 5 and 6 show the AFM images of the SPO sample with resist stripes. The measurements at three different positions (spot 1, 2 and 3) are shown for image sizes of 0.1×0.1μm, 1×1μm and 10×10μm, respectively.

2.1.2 1 Dimensional power-spectral-density analysis (1D PSD)

The average 1D PSD function along the X-axis is computed from the surface AFM data using the TOPO software.[4] TOPO computes the 1D PSD function along every line in the X direction of the surface data, and then computes the averages in X of the 1D PSD functions.[4]

Figures 7 and 8 show the average 1D PSD functions combining the data from the three different scan scales for each of the spots measured on the SPO samples without and with resist stripes, respectively.

To assess the surface roughness of the SPO samples, we compute the root-mean-square (rms) surface roughness using the TOPO software functions.[4]

The rms surface roughness σ, is define as

$$\sigma = \sqrt{2 \int_{f_1}^{f_2} S(f) df} \ , \tag{1}$$

and it is computed from the average 1D PSD function S(f).

The frequency range considered for the computation of the rms surface roughness via equation 1 is between 0.01nm^{-1} and 1nm^{-1} for all PSD functions. We note that noise from capacitive sensors and from surroundings can contribute to the 1D PSDs for some height frequencies, and may contribute to the rms surface roughness values computed. A methodology for removing those noise peaks is under investigation and will be applied to further analysis.

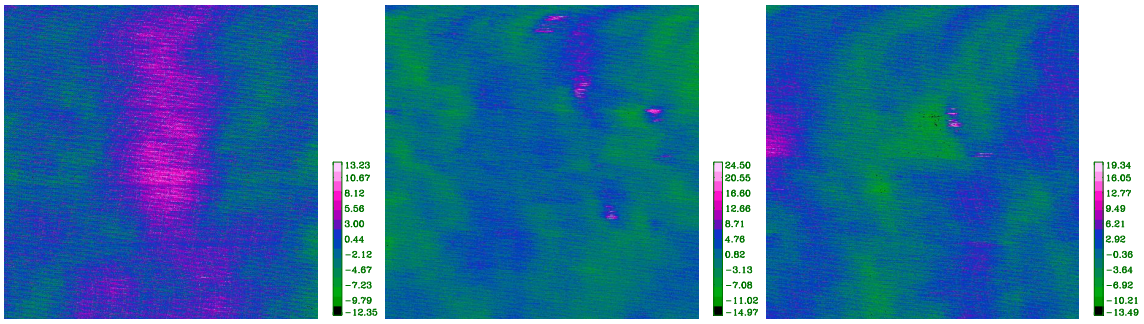

Figure 1. Uncoated SPO sample WITHOUT resist: AFM image, 0.1×0.1μm scan size, measurements on three different spots. Values listed in Å.

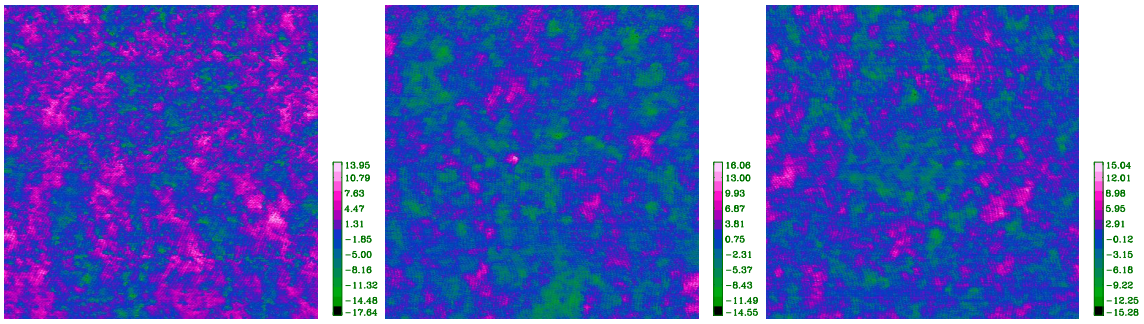

Figure 2. Uncoated SPO sample WITHOUT resist: AFM image, 1×1μm scan size, measurements on three different spots. Values listed in Å.

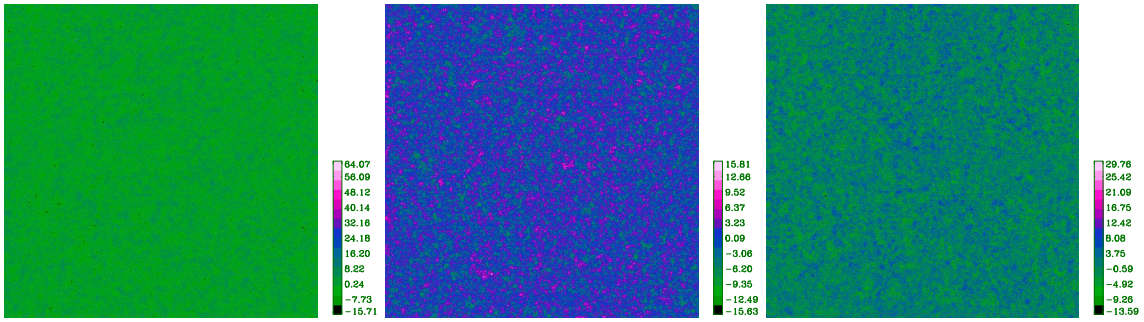

Figure 3. Uncoated SPO sample WITHOUT resist: AFM image, 10×10μm scan size, measurements on three different spots. Values listed in Å.

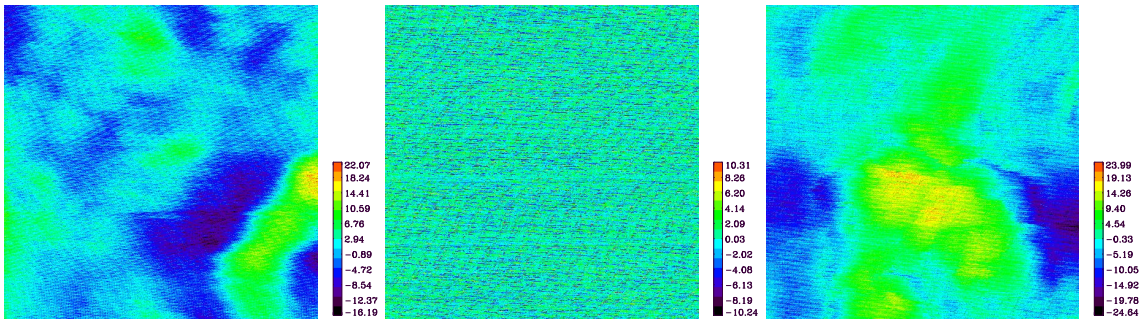

Figure 4. Uncoated SPO sample WITH resist: AFM image, 0.1×0.1μm scan size, measurements on three different spots. Values listed in Å.

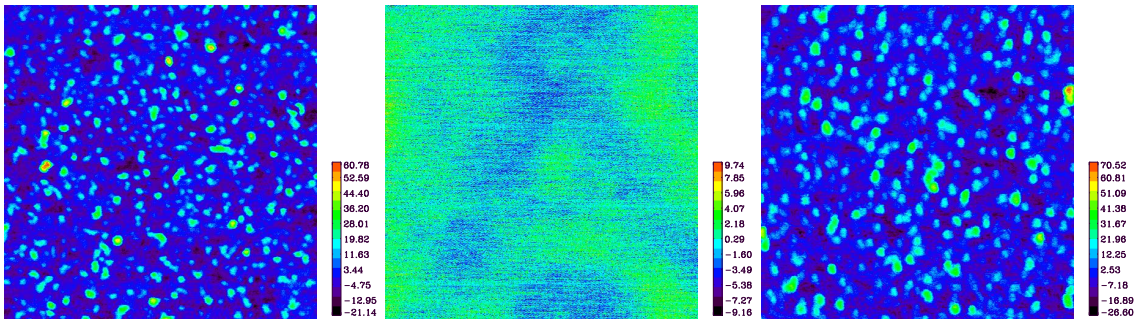

Figure 5. Uncoated SPO sample WITH resist: AFM image, 1×1μm scan size, measurements on three different spots. Values listed in Å.

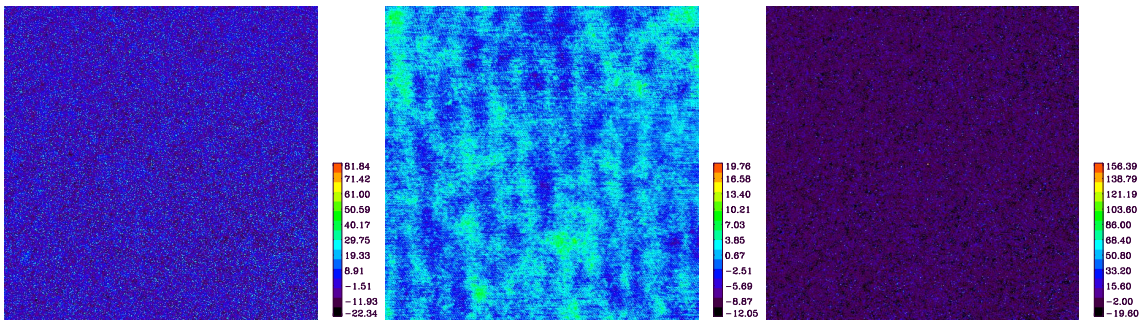

Figure 6. Uncoated SPO sample WITH resist: AFM image, 10×10μm scan size, measurements on three different spots. Values listed in Å.

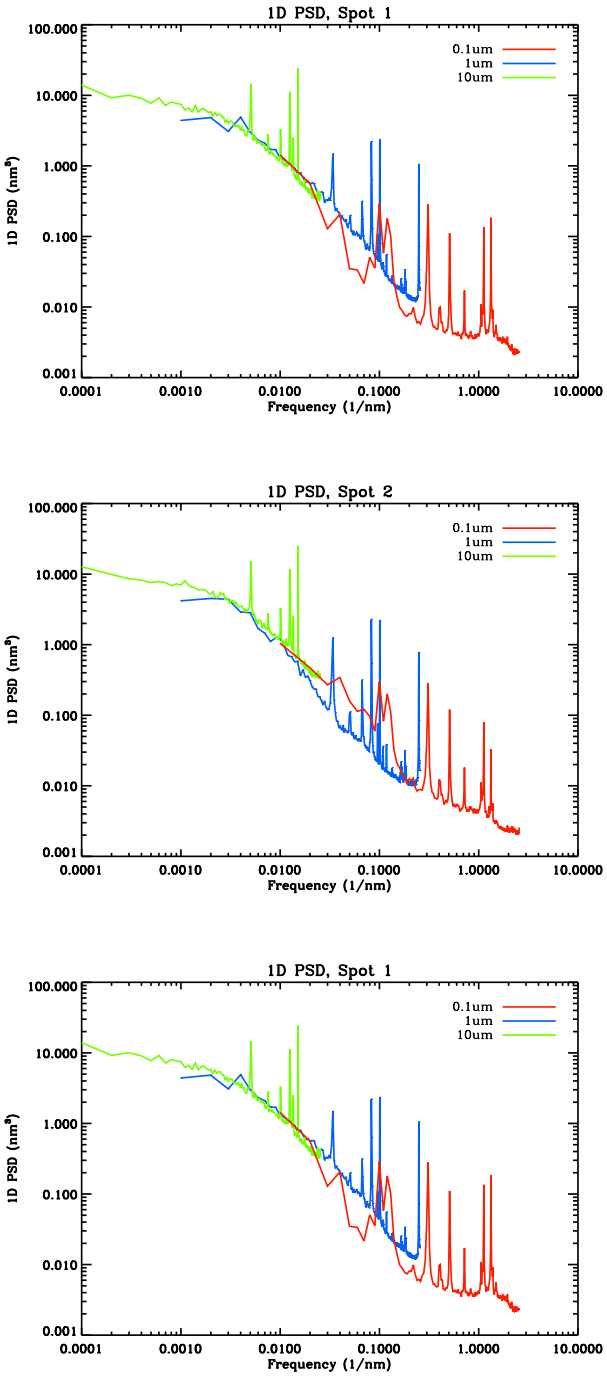

Figure 7. Uncoated SPO sample WITHOUT resist: 1D PSD, data from the three different scan sizes combined.

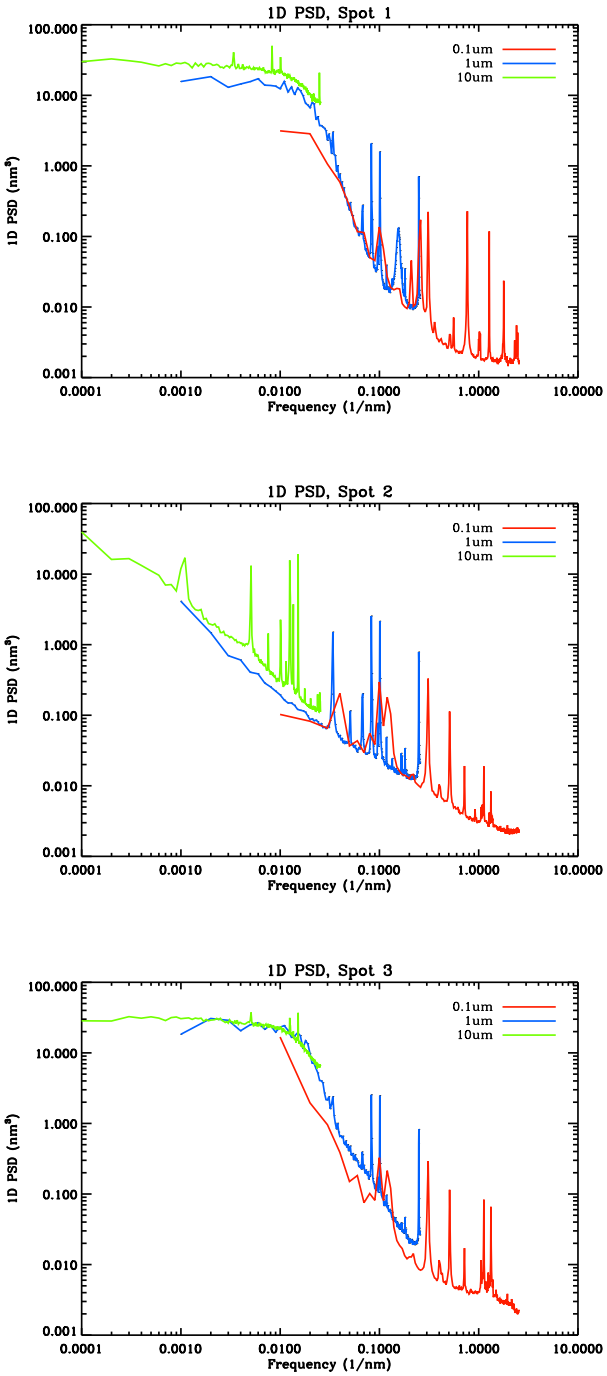

Figure 8. Uncoated SPO sample WITH resist: 1D PSD, data from the three different scan sizes combined.

Sample	Position	Scan size [μm]	σ [Å]
SPO without resist	spot 1	0.10×0.10	2.29
SPO without resist	spot 2	0.10×0.10	2.61
SPO without resist	spot 3	0.10×0.10	2.53
SPO with resist	spot 1	0.10×0.10	3.61
SPO with resist	spot 2	0.10×0.10	2.15
SPO with resist	spot 3	0.10×0.10	3.37
SPO without resist	spot 1	1.00×1.00	1.73
SPO without resist	spot 2	1.00×1.00	2.06
SPO without resist	spot 3	1.00×1.00	2.10
SPO with resist	spot 1	1.00×1.00	6.07
SPO with resist	spot 2	1.00×1.00	1.82
SPO with resist	spot 3	1.00×1.00	7.11
SPO without resist	spot 1	10.0×10.0	1.73
SPO without resist	spot 2	10.0×10.0	1.74
SPO without resist	spot 3	10.0×10.0	1.72
SPO with resist	spot 1	10.0×10.0	6.44
SPO with resist	spot 2	10.0×10.0	1.30
SPO with resist	spot 3	10.0×10.0	6.27

Table 1. Rms roughness computed from AFM of the two SPO samples.

2.1.3 Preliminary AFM results

The values of rms surface roughness derived in this study are listed in table 1. The AFM images, 1D PSD functions and rms surface roughness for the SPO sample without resist stripes at different measurements positions, are similar and consistent with each other, while this is not the case observed for the SPO sample with resist stripes.

The discrepancies observed in the analysis of the SPO sample with resist stripes indicates a non-homogeneous surface and present structures consistent with particulate contamination. Further AFM measurements of uncoated and coated SPO substrates are ongoing in other to clarify the discrepancies observed here.

2.2 Reflectivity and scatter measurements

Three different substrates were tested at DTU Space using X-ray Reflectometry (XRR) at 8 keV, these are: one pure Si wafer piece, one SPO with wedge and with resist stripes and one SPO with wedge and without resist stripes. Additional measurements were performed with synchrotron radiation at the four-crystal monochromator beamline of PTB at BESSY II in Berlin. The beamline provides monochromatic radiation from 1.75 keV to 10 keV with high spectral purity.[5] The samples were mounted in a UHV X-ray reflectometer that enables all 6 degrees of freedom for sample alignment. For one SPO sample without resist, detector scan at fixed energy and incidence angle as well as energy scans at fixed angles were performed.

The results from XRR measurements at DTU Space and the difference in surface roughness for the three substrates are shown in figure 9. Results on the surface roughness obtained by fitting the XRR data are listed in table 2.

The substrate without resist is a raw Si wafer piece with a SiO_x wedge layer. The angular wedging and the subsequent damage etching are responsible for the increased roughness from 0.25 nm to 0.45 nm. The addition of resist stripes further increases the roughness by 0.05 nm in between the stripes.

The energy scan at fixed angle of a SPO substrate without resist is shown in figure 10. The IMD model is comparable to the data with a slight offset. This might be caused by a figure error, the incident beam has a divergence of 43 arc seconds and this will lead to the broadening of edge observed, furthermore, the stochiometry of the wedge material deposited (SiO_x) may not be well described by the SiO model considered. In the IMD model, the wedge material is assumed to be SiO and the roughness $\sigma = 0.45$ nm.

Substrate type	Surface roughness
Raw silicon	0.25 nm
SPO substrate, no resist	0.45 nm
SPO substrate, with resist	0.5 nm

Table 2. Surface roughness obtained by fitting the data using the IMD software.

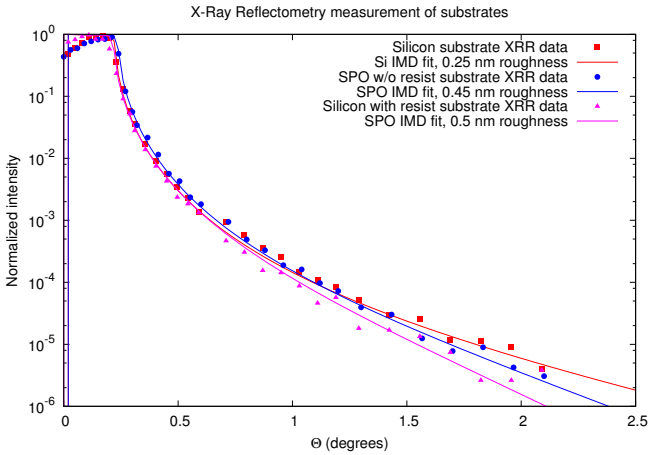

Figure 9. Comparison between XRR of SPO substrate with resist (triangles), SPO substrate without resist (circles) and raw Si wafer (squares) using a Cu K_α 8 keV rotating anode. The data is compared to IMD models (solid lines).

Scatter measurement was carried out on the SPO substrate without resist stripes at fixed angle of $\theta = 0.4^o$ and energy E = 8 keV, and it is shown in figure 11. The uncoated substrate shows little scattering, with 5.5 orders of magnitude needed to see the scatter part. Scatter measurements were also performed at DTU Space on SPO substrates within 4 orders of magnitude and no scatter could be observed.

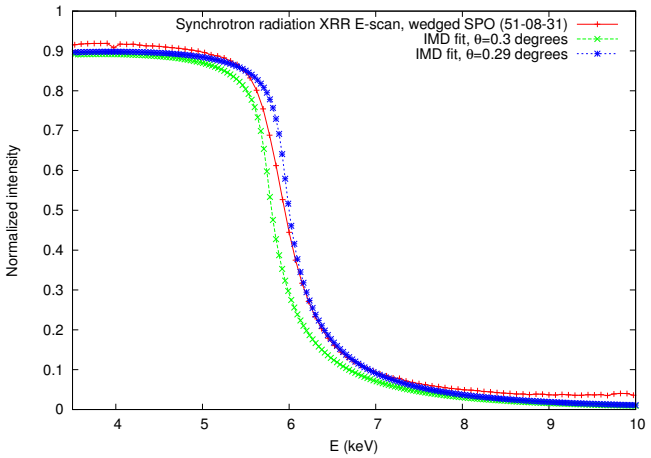

Figure 10. X-ray energy scan of SPO substrate w/o resist at $\theta = 0.3^o$. Two IMD models are compared to the X-ray data.

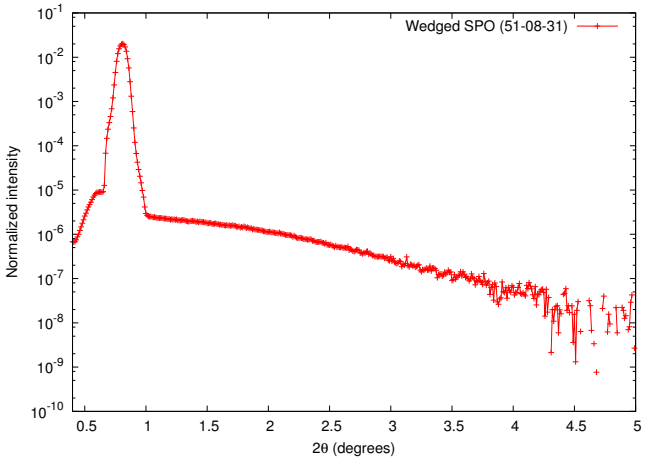

Figure 11. X-ray scatter measurement (background subtracted) of uncoated wedged SPO substrate without resist. Incident angle $\theta = 0.4^o$, energy E = 8 keV. Yoneda shoulder[6] is visible on the left side of the specular peak. Synchrotron radiation measurements taken at the four-crystal monochromator beamline of PTB at BESSY II.

3. COATING CHARACTERIZATION

3.1 Coated samples

Considering the ATHENA current coating baseline design, one SPO plates with resist stripes was coated along with two raw Si wafer pieces and a stress sample. The SPO plate was coated for XRR measurements both with synchrotron radiation in the laboratory of PTB at BESSY II and using a Cu K_α 8 keV rotating anode at the DTU Space. The Si wafer pieces were produced for XRR measurements and adhesion tests.

Initial environmental tests were performed and we observe no degradation on the tri-layer baseline coating. A thorough test campaign will be performed as part of the characterization of the optimized coating design.[2]

A considerable downside of using Ir/B_4C bi-layers in the ATHENA optics is the high stress in sputtered Ir thin films. The stress has shown to cause the film to disintegrate during resist removal after coating using acetone.

To reduce stress we produced test coatings of Ir/B_4C with a Cr undercoat. The required Cr layer thickness is dependent on the Ir thickness. For ATHENA baseline of 10 nm Ir, the optimum Cr thickness applied was of 10 nm. The surface roughness of the Cr layer is considerable ($\approx$ 1 nm), but X-ray Reflectometry results suggest that Ir/B4C bi-layer deposited on top of the Cr shows a roughness of 0.65 nm. This is a degradation in smoothness from 0.45 nm roughness for Ir/B4C without a Cr under layer.

To reduce stress and roughness in the coatings, a possible solution could be the introduction of N_2 gas during sputter deposition. Earlier results[7] have shown that small amounts of nitrogen gas can reduce the interface roughness of some materials.

Preliminary test coatings at DTU Space using N_2 gas during deposition of a Ir/B4C bilayer shown a moderate reduction of stress and surface roughness. The parameters for improvement are limited in the case of reactive gas sputter deposition in DC magnetron sputtering chambers as only the N_2 concentration can be changed and only between 0% and 30%. At higher concentrations, the N_2 molecules will adsorb to the target surface and create insulating regions, so-called target poisoning, which induces arcing that can cause the cathodes to shorten.

Coatings using N_2 presented here have been deposited using a mixture of 10% N_2 and 90% Ar at a total pressure of 2.8 mTorr.

The use of a Pt/B4C bi-layer as an alternative material combination to the Ir/B_4C baseline is under investigation.

Sample	SR XRR spot 1	SR XRR spot 2	SR XRR spot 3	DTU Space 8 keV	SR XRR Nitrogen
Cr/Ir/B_4C tri-layer	6.60	6.95	7.47	8.52	1.45

Table 3. Ir/B_4C interface roughness derived from X-ray data. Values listed in Å.

3.2 Adhesion qualification tests

Adhesion of the coatings was tested according to ISO9211-4 standard. The ATHENA baseline coating design was tested using scotch tape. By firmly attaching the tape to the surface and quickly ripping the tape off, a consistent test of the coating adhesion was completed. The Ir/B_4C bilayer proved able to withstand the removal of the tape.

3.3 Coating stress

The stress of the coating on the substrate was tested. A Dektak 150 Stylus profiler was used to twice measure the profile along the sample before a coating. After the coating the sample was measured again to see any change in the deflection of the sample due to the coating. By factoring in the thickness of the coating, a calculation of the compressive and tensile stress of the film was obtained. The sample used were 5 x 80 mm Si wafer pieces.

The baseline Ir/B_4C shows ≈ -4000 MPa of compressive stress and using N_2 can lower that value to ≈ -1600 MPa. Using a Cr undercoat on the baseline Ir/B_4C will decrease the stress significantly,[8,9] although there is some variation in the results. Latest results for a Cr/Ir/B_4C coating, with at 10 nm Cr undercoat, vary between 100 MPa and -1000 MPa in total stress.

As mentioned in section 3.2, the coating showed good adhesion to the substrate even when stress is high. The main problem of stress in optical coatings are the tendency of low adhesion and the possibility of bending the substrate, which for X-ray optics would decrease the efficiency of the optic. Since the coating shows good adhesion and since a stack of SPO substrates have little or no tendency to bend, the stress of the baseline coating is not likely be an issue.

3.4 X-ray reflectivity

Coating characterization using XRR was performed on the tri-layer Cr/Ir/B_4C. The XRR data collected at the laboratory of PTB at BESSY II and at the 8 keV X-ray facility at DTU Space are fit in order to check how well the coating recipes were produced, to evaluate the interface roughnesses and to compare the theoretical predictions to the actual performance of the produced coatings.

At the laboratory of PTB at BESSY II, the measurements were taken at three different spots for each coated sample and at one spot for the sample coated using Nitrogen. The XRR data is shown in figure 12. The grazing incident angle for XRR data is 0.619°.

The theoretical models for each coating were fit to the XRR data using the IMD software.[10] For the tri-layer coating, the model parameters allowed to vary are: layer thickness for each individual layer and roughness for each layer interface. The XRR data along with the best fit curves is presented in figure 13.

The roughness values for the Ir/B_4C interface obtained from fitting XXR data are listed in table 3 where we observe a significant reduction on roughness for the sample coated using N_2.

Introducing N_2 gas while coating will change coating rates for all materials. When introducing 10% N_2 while coating, low-Z materials will increase the coating rate by up to a factor of three and high-Z materials will have a 10-30% lower coating rate. At other reactive gas concentrations, the change in sputter rate will differ. For that reason, coating exact d-spacings for every material type requires thorough recalibration compared to non-reactive sputtering. Further investigation is necessary to understand the impact of nitrogen use on the coating performance.

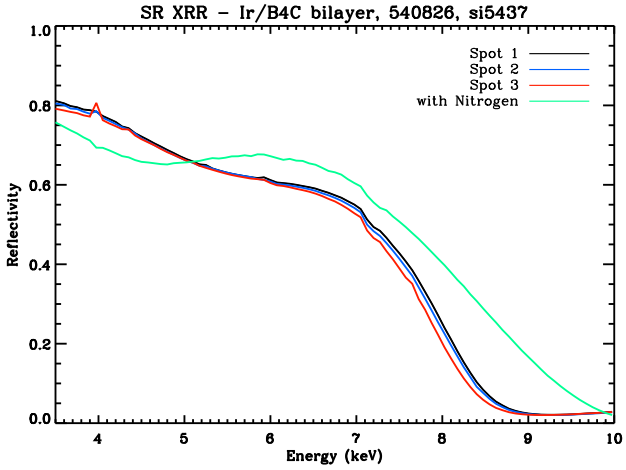

Figure 12. Synchrotron Radiation XRR data, tri-layer Cr/Ir/B_4C.

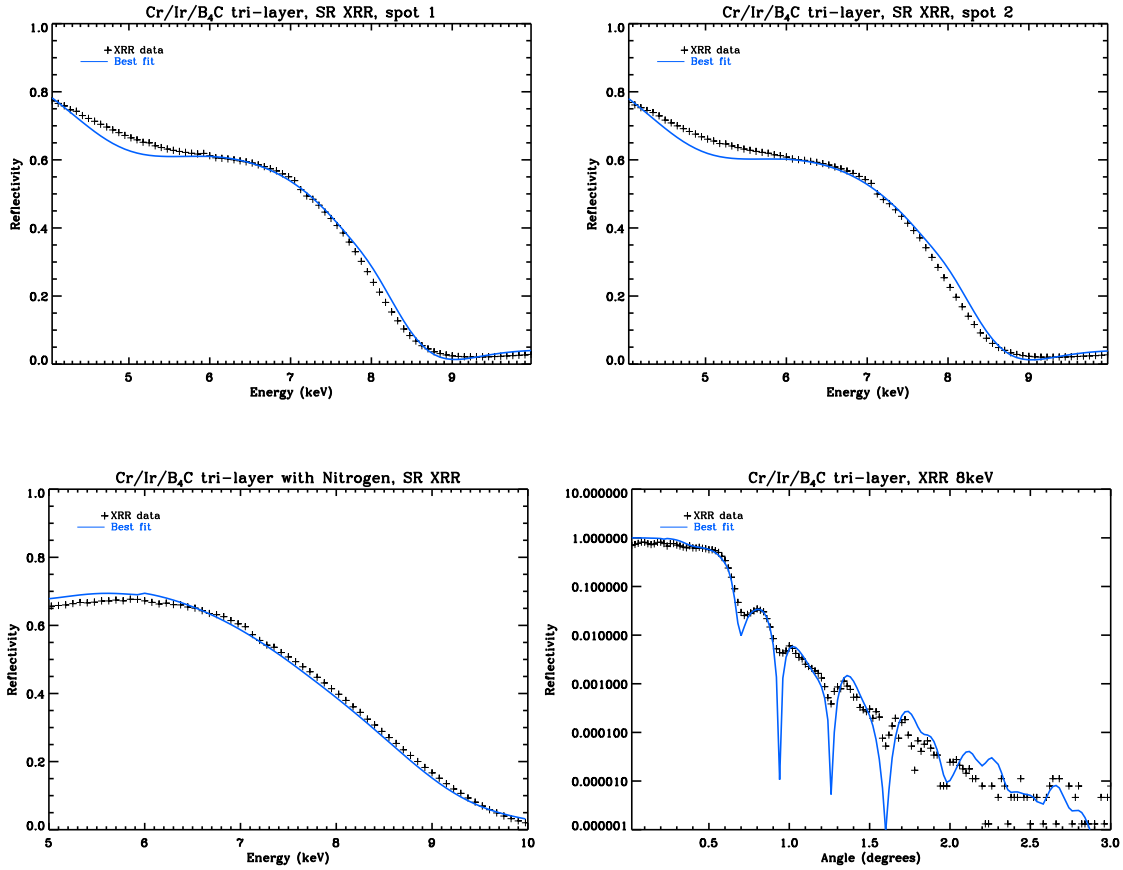

Figure 13. XRR data and best-fit model, tri-layer Cr/Ir/B_4C.

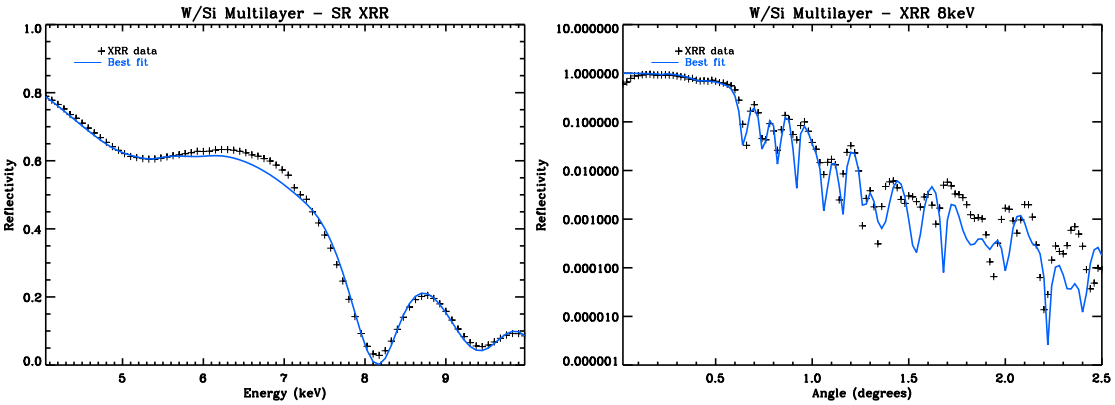

Figure 14. XRR data and best-fit model, multilayer W/Si.

	n	Γ	d_{min} (nm)	d_{max} (nm)	d_W (nm)	d_{B_4C} (nm)
Coating recipe[2]	5	0.60	5.0	11.0	11.0	8.0
Best-fit values	5	0.62	4.5	11.2	10.4	10.4
Offset	-	3.23%	10.00%	1.82%	5.40%	30.00%

Table 4. Linear graded W/Si multilayer. Listing model and best-fit values for number of bi-layers (n), thickness ratio between heavy and light material (Γ), minimum bi-layer thickness (d_{min}), maximum bi layer thickness (d_{max}), thickness of the W cap layer (d_W), and thickness of the B_4C overcoat d_{B_4C}

3.5 Multilayer coating development and tests

In addition to the baseline, an multilayer coating of W/Si[2] was also produced and submitted to the coating characterization processes described above. The multilayer coating consists of five W/Si bi-layers with a cap layer of W on top of the bi-layers and a overcoat of B_4C. The W/Si multilayer coating had a successful adhesion test, and presented low stress, ≈ -400 MPa.

Coating characterization using XRR was performed on the W/Si multilayer. As described in 3.1, the XRR data collected at the laboratory of PTB at BESSY II and at the 8 keV X-ray facility at DTU Space. The XRR data was fit in order to the optimized coating model using IMD. The model parameters allowed to vary are: layer thickness for each individual layer, thickness ratio between heavy and light material (Γ) and roughness for each layer interface.

The XRR data along with the best fit curves is presented in figure 14. The coating model, best-fit values and the offset between model and best-fit values are listed in table 4. The discrepancies between the coating recipe and best-fit values are due to the calibration procedure. An average roughness of 0.525 nm was obtained by fitting a model to the W/Si XRR data.

To image the layer structure, cross-sectional Transmission Electron Microscopy (TEM) was performed on the coated SPO sample containing the W/Si multilayer. A small section of the coated plate is cleaved and thinned by a focused ion beam milling.[11,12] The samples must be thin enough in order to be transparent to electrons, the sample thickness for this analysis is less than 100 nm.

The TEM image of the W/Si multilayer coating is shown in figure 15. Further coating characterization includes a complete TEM study where we expect to evaluate the individual coated layers and their interface roughnesses. The TEM study is ongoing and will be reported in the near future.

4. SUMMARY

The performance of the mirror coatings plays a critical role for the ATHENA mission. In this study, we have presented the initial results on the testing for development and characterization of coatings on SPO substrates.

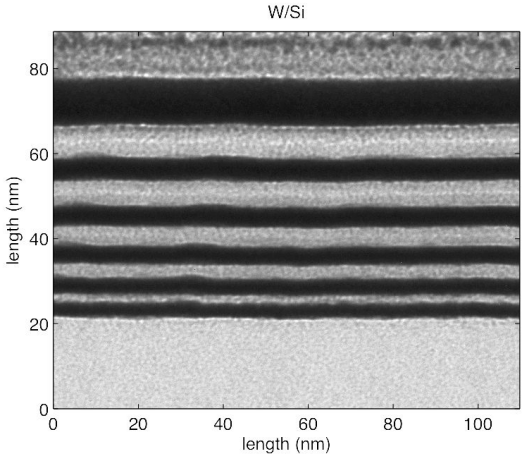

Figure 15. TEM image of the W/Si multilayer coating.

We performed pre-coating characterization on the SPO substrates making use of both AFM and XRR measurements. The AFM measurements of SPO substrates with resist stripes present structures consistent with particulate contamination. A complete AFM study is being performed in order to, among other things, verify this results. XRR measurements indicate that the wedge deposition increases the substrate surface roughness by $\approx 80\%$. The resist stripes further increases the roughness by $\approx 11\%$. Initial scatter measurements indicate little or no scattering on uncoated SPO substrates.

We performed coating characterization on both the baseline Ir/B_4C bi-layer and on a optimized W/Si multilayer coating. We tested the use of Cr as an undercoat to reduce the high stress on the Ir/B_4C bi-layer. We find that introducing a bottom layer of Cr does indeed reduce the coating stress, but increases the surface roughness by 30%, with derived values for the surface roughness of Cr/Ir/B4C tri-layer reaching 0.65 nm.

We investigated the introduction of N_2 gas during sputter deposition to reduce stress and roughness. We observe significant reduction in the Ir/B_4C interface roughness while the coating stress showed no improvement. Further studies are necessary to assess the impact of N_2 gas on the coating performance.

The W/Si multilayer coating tested seems to perform well and shows low stress. The coating is well fit by the optimized IMD model,[2] with average roughness of 0.525 nm.

The development and characterization of coatings on SPO substrates is rapidily progressing and new results on both preliminary characterization and further investigation of other material combinations will be reported in the near future.

REFERENCES

[1] Wallace, K., Bavdaz, M., and Gondoin, P., "Silicon pore optics development," *Proceedings of SPIE* **7437** (2009).

[2] Ferreira, D. D. M., Christensen, F. E., Jakobsen, A. C., Westergaard, N. J. S., and Shortt, B., "ATHENA coating optimization," *Proceedings of SPIE* (2012).

[3] Kofod, N., Garnaes, J., and Joergensen, J. F., "Methods for lateral calibration of Scanning Probe Microscopes based on two dimensional transfer standards in Proceedings of the 4th seminar on Quantitative Microscopy QM 2000 Dimensional measurements in the micro- and nanometre range," *K. Hasche, W. Mirande, G. Wilkening ed. (PTB, Braunschweig, Germany)* , 36–43 (2000).

[4] Windt, D. L., "TOPO - Surface topography analysis, version 2.05," (Sept. 2000).

[5] Krumrey, M. and Ulm, G., "High accuracy detector calibration at the PTB four-crystal monochromator beamline," *Nucl. Instr. and Meth. A* **1175 - 1178**, 467 – 468 (2001).

[6] Yoneda, Y., "Anomalous surface reflection of x-rays," *Physical Review* **131**, 2010 (1963).

[7] Windt, D., "Reduction of stress and roughness by reactive sputtering in W/B4C X-ray multilayer films," *Proceedings of SPIE* **6688** (2007).

[8] Hill, M., Blake, P., Carter, R., Wing-Chan, K., and Deere, K., "International X-Ray Observatory (IXO) Segmented Glass Mirror Technology Development Status And Roadmap," tech. rep. (Sept. 2010).

[9] Jakobsen, A. C., Ferreira, D. D. M., Christensen, F. E., Shortt, B., Collon, M., and Ackermann, M. D., "Preliminary coating design and coating developments for ATHENA," in [*Optics for EUV, X-Ray, and Gamma-Ray Astronomy V*], SPIE (Sept. 2011).

[10] Windt, D. L., "IMD - Software for modeling the optical properties of multilayer films," *Computers in Physics* **12**, 360–370 (Jan. 1998).

[11] Williams, D. B. and Carter C. B., [*Transmission electron microscopy : a textbook for materials science.*], Springer, New York London (2009).

[12] Brejnholt, N. F., [*NuSTAR calibration facility and multilayer reference database*], The Technical University of Denmark (2012). Ph. D. Thesis.

Appendix C

X-ray optics for axion helioscopes

Preprint

X-ray optics for axion helioscopes

Anders C. Jakobsen[a], Michael J. Pivovaroff[b] and Finn E. Christensen[a]

[a]Danish Technical University (DTU) Space, Elektrovej 327, DK-2800 Kgs. Lyngby, Denmark
[b]Lawrence Livermore National Laboratory, 7000 East Avenue, Livermore, CA 94550, USA

ABSTRACT

A method of optimizing grazing incidence x-ray coatings in ground based axion helioscopes is presented. Software has been been developed to find the optimum coating when taking both axion spectrum and Micromegas detector quantum efficiency into account. A comparison of the relative effective area in the telescope using different multilayer material combinations is produced. Similar methods are used for IAXO, a planned axion helioscope. Additionally, the optimal focal length is modelled while taking into account the least possible background contribution from the detector.

Keywords: X-ray optics, axion, multilayer coatings

1. INTRODUCTION

Axions are theoretical particles created by the Primakoff effect[1] from photons interacting with strong electric and magnetic fields. An obvious place to look for axions would then be our own sun. The particles are weakly interacting, so detection becomes a challenge. A solution is to use the Primakoff effect again to reconvert the axion into a photon using a strong magnetic field and subsequently detecting the photon in an x-ray detector as seen in figure 1.

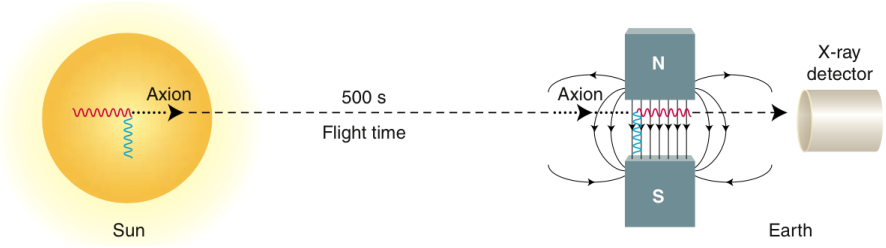

Figure 1. Diagram of axions created by the Primakoff effect in the sun, travelling to Earth and getting detected using a strong magnetic field and a detector.

In the past 30 years the hunt for axions as a solution to CP violation in particle physics and a possible candidate for dark matter, have required larger and more sensitive instruments. The third and latest generation of helioscopes for axion detection is the CERN Axion Solar Telescope (CAST),[2–5] consisting of a LHC prototype magnet and low background MicroMegas detectors.[6]

The main problem is to distinguish a small signal amidst the background, which largely comes from the detector. The magnetic bores on CAST are 50 mm wide, so a detector to cover a bore consequently becomes large. The detector area is proportional to the background squared. A solution is to reflect the x-ray photons coming from the bore in an x-ray optic and onto a much smaller detector. In the next section, the design of such an optic is explained.

Further author information:
A.C.J.: E-mail: jakobsen@space.dtu.dk, Telephone: +45 4525 9735

2. CAST TELESCOPE GEOMETRY

The x-ray optic for CAST is of a relatively small size, as only photons coming out of a 50 mm bore will be reflected and the focal length is limited to 1.5 m due to one of the side walls in the CAST building.

An already proven technology for building Wolter I type optics for space based applications is used in the NuSTAR telescope.[7,8] Slumped glass pieces, each 0.2 mm thick are placed on a SiC mandrel and graphite spacers are used to hold each piece in place at the correct angle. Two stacks of slumped glass substrates with graphite spacers are required for the double reflection geometry of the Wolter I optic. The optic for CAST will be made from spare NuSTAR glass, but only using 1/6th of the full circle and with an adjusted mandrel.

The angle of each glass substrate depends on the focal length, l, and radius, r, and is described as $\tan 4\alpha = r/l$. Every layer put on the mandrel has to have a width wide enough to cover the bore opening which sets a lower limit on the radius of the innermost glass layer. Each subsequent glass substrate is mounted on top of the earlier so there is no overlap. The resulting diagram for an optic optimized for a 50 mm bore opening and 1.5 m focal length is shown in figure 2.

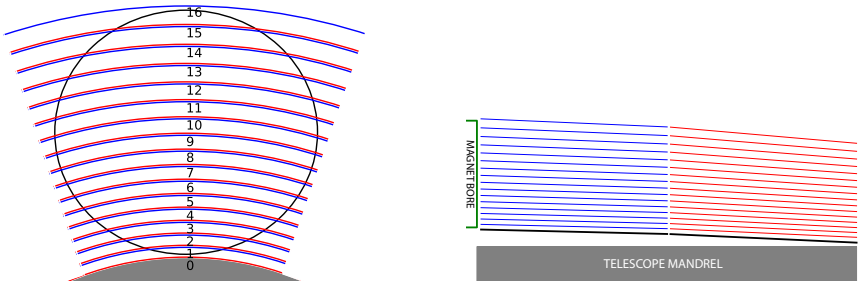

Figure 2. Diagrams of glass layering in Wolter I optic for the CAST axion helioscope. **Left:** Optic as seen from front. The circle shows the magnet bore opening compared to the optic. **Right:** Optic seen from side. Horizontal axis is compressed to show the tilt of each glass layer.

3. CAST COATINGS

Optimal coatings were calculated by taking into consideration detector efficiency, axion spectrum at each optical glass angle in the telescope. Axion spectrum is given by theory as a curve reminiscent of black body radiation between 0.1 and 10 keV as seen in figure 3.

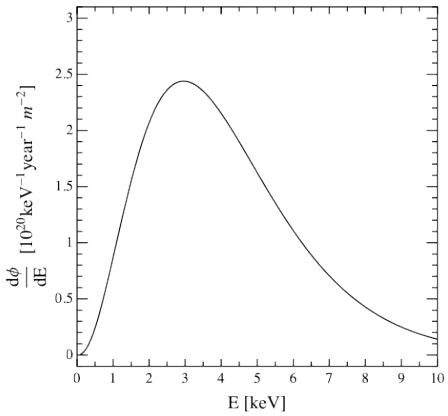

Figure 3. Solar axion flux spectrum at Earth, originating from the Primakoff process.

Material types investigated were multilayers of W/B_4C, W/Si, Pt/B_4C, Ni/B_4C as well as single layers of W, Pt, Ir and Ni. W/B4C and W/Si are well understood coatings for x-ray reflectivity and considerably less expensive to use W than Pt or Ir. Using B4C instead of Si as the light material will give increase reflectivity at 1 - 4 keV, but also gives slightly higher stress in the coating.[9] Ni/B4C coatings are not well understood and can give a high interfacial roughness between light and heavy material, but performs similar to W/B4C and Ir/B4C at 1-10 keV.

At a given glass substrate angle, α, the coating geometry was optimized by trying every combination in a parameter space of n (number of bilayers), d_{min} (minimum bilayer thickness), d_{max} (maximum bilayer thickness) and Γ (ratio between heavy and light material in a bilayer.) For every combination, the x-ray reflectivity was calculated using IMD[10] , multiplied with axion spectrum and detector effeciency and integrated to give a figure of merit (eqn. 1). The F.O.M. found in the parameter space is chosen as the optimal coating recipe for the given angle and focal length.

$$F.O.M. = \int_{0.1}^{10} R^2(\alpha, E)\ QE_{det}(E)\ S_{axion}\ dE \tag{1}$$

Output for optimized coating recipes for a w/B_4C material combination can be seen on the left side of figure 4. Each glass substrate layer should have between 2 and 6 bilayers with d-spacings between 50 and 260 Å.

A comparison of material combinations is seen on the right side og figure 4. The effective areas are calculated using eqn 2. Multilayers are seen to easily outperform the single layer coatings. Best performing are W/B_4C and Ni/B_4C multilayers.

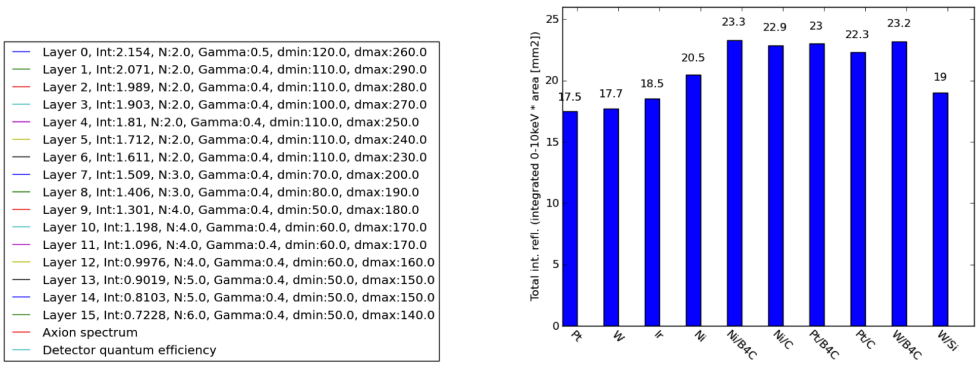

Figure 4. Results of multilayer coating optimization for the CAST Wolter I optic. **Left:** Optimized recipe for each layer in the optic. **Right:** Effective area comparison between each optimized material combination recipe.

$$A_{effective} = \sum_{i=1}^{N} \int_{0.1}^{10} R_i^2(\alpha, E)\ QE_{det}(E)\ S_{axion}\ A_i\ dE \tag{2}$$

4. TELESCOPES FOR THE IAXO HELIOSCOPE

A next generation axion helioscope currently in the proposal stage is the International AXion Observatory, IAXO.[11–13] It is a direct successor to CAST, with much larger magnet bores, bigger super conducting magnet and possibility of higher inclination, meaning it can measure axions coming from the sun 12 hours a day. An illustration can be seen in figure 5

Optimal coatings were calculated by taking into consideration detector efficiency, axion spectrum at each optical glass angle in the telescope. The telescope geometry, glass substrate angles and positions were first computed for focal lengths 4, 5, 6, 7, 8, 9 and 10 m. For each focal length, the x-ray reflectivity at 1-10 keV

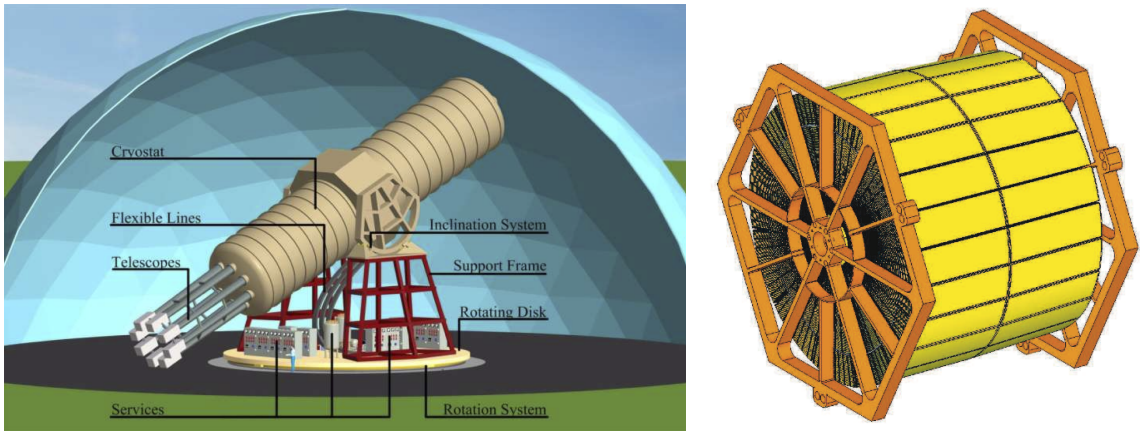

Figure 5. IAXO, a next generation axion helioscope. **Left:** Model of proposed IAXO setup. Superconducting magnet (cryostat) with 8 bores each 600 mm in diameter placed on a rotating platform to track the sun. **Right:** Model of a single Wolter I type optic for IAXO. One optic will be placed on the end of each bore.

for each coating material combination and thin film geometry were compared. Axion spectrum and detector efficiency were included in the comparison.

For a focal length of 4 m and bore diameter of 0.6 m, 110 glass substrate layers are needed to focus incoming x-rays to the same spot. At increasing focal length, even more glass layers and for 10 m focal length, required glass layers reach 235. To simplify the optimization and eventual coating deposition, the number of coating 'recipes' are fixed at 10, so only 10 different coatings will be required for a telescope.

5. IAXO TELESCOPE FOCAL LENGTH

To calculate the total telescope efficiency at a given focal length, the following equation was used.

$$\text{Throughput}_i \quad = \quad \frac{R_i^2 * A_{cs} * 0.8}{A_{bore}} \tag{3}$$

The fraction of photons reflected by layer i could be found using the cross sectional area of a layer opening and the total area of the bore opening. The factor 0.8 was used to include obscurations in the form of substrate spacers.

To find the optimal focal length, a non traditional approach was used. For a generic x-ray optic, the longer focal length gives a higher effective area, which was also the case here. But at increasing focal lengths, the focused spot also becomes bigger as a result of optic HPD (Half Power Diameter). Since the goal was to find a signal in the background, it was desirable to use a detector as small as possible, considering that the area of the detector is proportional to the background. In order to minimize detector area, it was therefore required to minimize the focused spot size, while also maximizing the effective area of the telescope. Spot area was determined using the enclosed energy diameter (EED) of the telescope at focal length f using a telescope HPD of 2 arc seconds for the worst case scenario and 1 arc second for the best case. EED of the sun (EED_{sun}) was also included using an HPD of 3.61 arc minutes. A combined EED of $(\text{EED}^2 + \text{EED}_{\text{sun}}^2)^{\frac{1}{2}}$ was used to calculate the area of the spot.

A new figure of merit, which also includes the square root of the spot arean was used for optic optimization:

$$F.O.M. = \frac{\int_{0.1}^{10} R^2(\alpha, E)\ QE_{det}(E)\ S_{axion}\ dE}{\sqrt{a}} \tag{4}$$

The parameter space used for optimization was identical to that used for the CAST optic, but with a variety of focal lengths from 4 m to 10 m and with only one material combination (W/B_4C). The result can be seen in figure 6. A notable difference in F.O.M. can be seen as focal length increases, resulting in larger focused spot. The optimal focal length is seen to be 5 m.

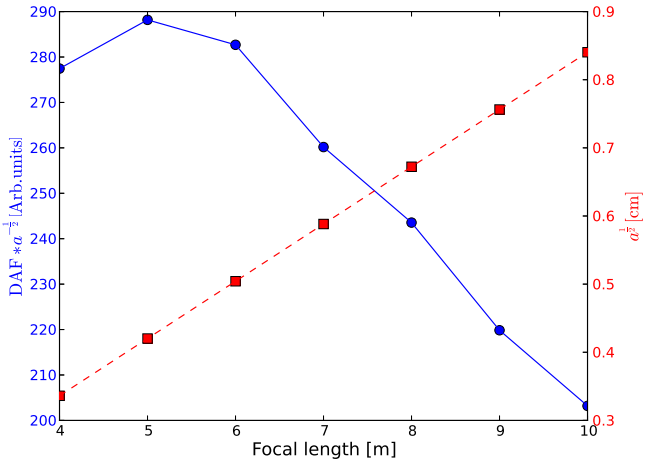

Figure 6. Result of focal length optimization. Circles show the throughput divided by the square root of the focused spot area. Squares show the square root of the focused spot area.

6. CONCLUSION

Software was developed to optimize geometry and multilayer coatings for the CAST axion helioscope. By including both detector quantum efficiency and axion spectrum in the optimizxation procedure, a true value of coating efficiency can be found. Maximum throughput can be achieved using either Ni/B_4C or W/B_4C multilayer coatings with 2-6 bilayers and d-spacings of 5-26 nm.

An extension of same software was used to find the optimal focal length of optics for the next generation IAXO axion helioscope. Using W/B_4C multilayer coatings and including the size of the focused spot in the calculations, a optimal focal length of 5 m was found.

REFERENCES

[1] Primakoff, H., "Photo-Production of Neutral Mesons in Nuclear Electric Fields and the Mean Life of the Neutral Meson," *Physical Review* **81**, 899–899 (Mar. 1951).

[2] Iguaz, F. J., "The CAST experiment: status and perspectives," *arXiv.org* (Oct. 2011).

[3] Ferrer-Ribas, E., Arik, M., Aune, S., Barth, K., Belov, A., Borghi, S., Bräuninger, H., Cantatore, G., Carmona, J. M., Cetin, S. A., Collar, J. I., Dafni, T., Davenport, M., Eleftheriadis, C., Elias, N., Ezer, C., Fanourakis, G., Friedrich, P., Galan, J., Garcia, J. A., Gardikiotis, A., Gazis, E. N., Geralis, T., Giomataris, I., Gninenko, S., Gomez, H., Gruber, E., Guthörl, T., Hartmann, R., Haug, F., Hasinoff, M. D., Hoffmann, D. H. H., Iguaz, F. J., Irastorza, I. G., Jacoby, J., Jakov vcić, K., Karuza, M., Königsmann, K., Kotthaus, R., Krcmar, M., Kuster, M., Lakic, B., Laurent, J. M., Liolios, A., Ljubičić, A., Lozza, V., Lutz, G., Luzon, G., Morales, J., Niinikoski, T., Nordt, A., Papaevangelou, T., Pivovaroff, M. J., Raffelt, G., Rashba, T., Riege, H., Rodriguez, A., Rosu, M., Ruz, J., Savvidis, I., Silva, P. S., Solanki, S. K., Stewart, L., Tomas, A., Tsagri, M., van Bibber, K., Vafeiadis, T., Villar, J., Vogel, J. K., Yildiz, S. C., and Zioutas, K., "Results and perspectives of the solar axion search with the CAST experiment," *arXiv.org* (Sept. 2012).

[4] Papaevangelou, T., "Status report of the CAST Experiment & Running in 2013-2014," Tech. Rep. CERN-SPSC-2012-028. SPSC-SR-106, Geneva (Oct. 2012).

[5] Barth, K., Belov, A., Beltran, B., Bräuninger, H., Carmona, J. M., Collar, J. I., Dafni, T., Davenport, M., Di Lella, L., Eleftheriadis, C., Englhauser, J., Fanourakis, G., Ribas, E. F., Fischer, H., Franz, J., Friedrich, P., Galan, J., Garcia, J. A., Geralis, T., Giomataris, I., Gninenko, S., Gomez, H., Hassinoff, M. D., Heinsius, F. H., Hoffmann, D. H. H., Irastorza, I. G., Jacoby, J., Jakovcic, K., Kang, D., Königsmann, K., Kotthaus, R., Kousouris, K., Krcmar, M., Kuster, M., Lakic, B., Liolios, A., Ljubičić, A., Lutz, G., Luzon, G., Miller, D. W., Papaevangelou, T., Pivovaroff, M. J., Raffelt, G., Redondo, J., Riege, H., Rodriguez, A., Ruz, J., Savvidis, I., Semertzidis, Y., Stewart, L., van Bibber, K., Vieira, J. D., Villar, J. A., Vogel, J. K., Walckiers, L., and Zioutas, K., "CAST constraints on the axion-electron coupling," *arXiv.org* (Feb. 2013).

[6] Tomas, A., Ferrer-Ribas, E., Luzon, G., Gomez, H., Ruz, J., Dafni, T., Segui, L., Fanourakis, G., Yildiz, S. C., Galan, J., Giomataris, I., Aune, S., Geralis, T., Gardikiotis, A., Morales, J., Iguaz, F. J., Garcia, J. A., Rodriguez, A., Papaevangelou, T., Irastorza, I. G., and Vafeiadis, T., "The new micromegas X-ray detectors in CAST," *X-Ray Spectrom.* **40**(4), 240–246 (2011).

[7] Harrison, F. A., Craig, W. W., Christensen, F. E., Hailey, C. J., Zhang, W. W., Boggs, S. E., Stern, D., Cook, W. R., Forster, K., Giommi, P., Grefenstette, B. W., Kim, Y., Kitaguchi, T., Koglin, J. E., Madsen, K. K., Mao, P. H., Miyasaka, H., Mori, K., Perri, M., Pivovaroff, M. J., Puccetti, S., Rana, V. R., Westergaard, N. J., Willis, J., Zoglauer, A., An, H., Bachetti, M., Barrière, N. M., Bellm, E. C., Bhalerao, V., Brejnholt, N. F., Fuerst, F., Liebe, C. C., Markwardt, C. B., Nynka, M., Vogel, J. K., Walton, D. J., Wik, D. R., Alexander, D. M., Cominsky, L. R., Hornschemeier, A. E., Hornstrup, A., Kaspi, V. M., Madejski, G. M., Matt, G., Molendi, S., Smith, D. M., Tomsick, J. A., Ajello, M., Ballantyne, D. R., Baloković, M., Barret, D., Bauer, F. E., Blandford, R. D., Brandt, W. N., Brenneman, L. W., Chiang, J., Chakrabarty, D., Chenevez, J., Comastri, A., Dufour, F., Elvis, M., Fabian, A. C., Farrah, D., Fryer, C. L., Gotthelf, E. V., Grindlay, J. E., Helfand, D. J., Krivonos, R., Meier, D. L., Miller, J. M., Natalucci, L., Ogle, P., Ofek, E. O., Ptak, A., Reynolds, S. P., Rigby, J. R., Tagliaferri, G., Thorsett, S. E., Treister, E., and Urry, C. M., "THE NUCLEAR SPECTROSCOPIC TELESCOPE ARRAY(NuSTAR) HIGH-ENERGY X-RAY MISSION," *The Astrophysical Journal* **770**, 103 (May 2013).

[8] Christensen, F. E., Jakobsen, A. C., Brejnholt, N. F., Madsen, K. K., Hornstrup, A., Westergaard, N. J., Momberg, J., Koglin, J., Fabricant, A. M., Stern, M., Craig, W. W., Pivovaroff, M. J., and Windt, D., "Coatings for the NuSTAR mission," in [*SPIE Optical Engineering + Applications*], O'Dell, S. L. and Pareschi, G., eds., 81470U–81470U–19, SPIE (Sept. 2011).

[9] Jakobsen, A. C., Ferreira, D. D. M., Christensen, F. E., Shortt, B., Collon, M., and Ackermann, M. D., "Preliminary coating design and coating developments for ATHENA," in [*Optics for EUV, X-Ray, and Gamma-Ray Astronomy V*], 81470T–8, SPIE (Sept. 2011).

[10] Windt, D. L., "IMD—Software for modeling the optical properties of multilayer films," *Computers in Physics* **12**, 360 (1998).

[11] Irastorza, I. G., Avignone, F. T., Caspi, S., Carmona, J. M., Dafni, T., Davenport, M., Dudarev, A., Fanourakis, G., Ferrer-Ribas, E., Galan, J., Garcia, J. A., Geralis, T., Giomataris, I., Gomez, H., Hoffmann, D. H. H., Iguaz, F. J., Jakovcic, K., Krcmar, M., Lakic, B., Luzon, G., Pivovaroff, M., Papaevangelou, T., Raffelt, G., Redondo, J., Rodriguez, A., Russenschuck, S., Ruz, J., Shilon, I., Ten Kate, H., Tomas, A., Troitsky, S., van Bibber, K., Villar, J. A., Vogel, J., Walckiers, L., and Zioutas, K., "Towards a new generation axion helioscope," *arXiv.org* (Mar. 2011).

[12] Irastorza, I. G., Avignone, F. T., Cantatore, G., Caspi, S., Carmona, J. M., Dafni, T., Davenport, M., Dudarev, A., Fanourakis, G., Ferrer-Ribas, E., Galan, J., Garcia, J. A., Geralis, T., Giomataris, I., Gninenko, S., Gomez, H., Hoffmann, D. H. H., Iguaz, F. J., Jakovcic, K., Krcmar, M., Lakic, B., Luzon, G., Lindner, A., Pivovaroff, M., Papaevangelou, T., Raffelt, G., Redondo, J., Russenschuck, S., Ruz, J., Shilon, I., Ten Kate, H., Tomas, A., Troitsky, S., van Bibber, K., Villar, J. A., Vogel, J., Walckiers, L., and Zioutas, K., "The International Axion Observatory (IAXO)," *arXiv.org* (Jan. 2012).

[13] Vogel, J. K., Avignone, F. T., Cantatore, G., Carmona, J. M., Caspi, S., Cetin, S. A., Christensen, F. E., Dael, A., Dafni, T., Davenport, M., Derbin, A. V., Desch, K., Diago, A., Dudarev, A., Eleftheriadis, C., Fanourakis, G., Ferrer-Ribas, E., Galan, J., Garcia, J. A., Garza, J. G., Geralis, T., Gimeno, B., Giomataris, I., Gninenko, S., Gomez, H., Hailey, C. J., Hiramatsu, T., Hoffmann, D. H. H., Iguaz, F. J., Irastorza, I. G.,

Isern, J., Jaeckel, J., Jakovcic, K., Kaminski, J., Kawasaki, M., Krcmar, M., Krieger, C., Lakic, B., Lindner, A., Liolios, A., Luzon, G., Ortega, I., Papaevangelou, T., Pivovaroff, M. J., Raffelt, G., Redondo, J., Ringwald, A., Russenschuck, S., Ruz, J., Saikawa, K., Savvidis, I., Sekiguchi, T., Shilon, I., Silva, H., ten Kate, H. H. J., Tomas, A., Troitsky, S., van Bibber, K., Vedrine, P., Villar, J. A., Walckiers, L., Wester, W., Yildiz, S. C., and Zioutas, K., "IAXO - The International Axion Observatory," *arXiv.org* (Feb. 2013).

Appendix D

Conceptual design of the International Axion Observatory (IAXO)

Publication printed in *Journal of Instrumentation*. It is a retooled version of the Letter of Intent that was submitted to the CERN SPSC in summer 2013.

Presented in this thesis is a shorter version of the paper, only representing the work that I did. The full paper is 46 pages and a large part is outside the field of X-ray optics. First half page is part of an earlier section and cut out here.

mandrel, and two unique mandrels are required for each individual layer (one for the parabolic-shaped primary, another for the hyperbolic-shaped secondary). Missions that have utilized replicated x-ray telescopes include: *XMM* [50], launched in 1999; *Beppo-SAX* [51], launched in 1996; *ABRIXAS* [52], launched in 1999; the balloon-borne HERO mission [53], first flown in 2002; and the sounding rocket mission FOXSI, currently under development. It is important to mention that CAST currently employs a flight-spare telescope from *ABRIXAS*.

3.2.5 Integral shell optics: monolithic glass

For completeness, we mention telescopes formed from monolithic pieces of glass. Although these telescopes have excellent focusing quality and have produced some of the best images of the x-ray sky, because of the cost and weight, no future mission is expected to use this approach. Missions that have utilized monolithic optics include *Einstein* [54], launched in (1978); *RoSAT*, [55] launched in 1980; and the *Chandra X-ray Observatory* [56], launched in 1998.

3.3 The baseline technology for IAXO

For IAXO, we have adopted segmented, slumped glass optics as the baseline fabrication approach for several reasons. First, the technology is mature and has been developed by members of the IAXO collaboration, most recently for the NuSTAR satellite mission. Second, this approach easily facilitates the deposition of single-layer or multi-layer reflective coatings. Third, it is the least expensive of the fabrication techniques. Fourth, the imaging requirement for solar observations for IAXO is very modest-focusing the central 3 arcminute core of the Sun. Although other optics technologies may have better resolution than slumped glass, they would not produce a significantly smaller focused spot of the solar core.

3.4 The IAXO x-ray telescopes

3.4.1 Design and optimization of the IAXO x-ray telescopes

The optical prescription and reflective coatings were identified by a systematic search of a multi-dimensional parameter space that accounted for the detector efficiency, axion spectrum, optics properties and recipe of the reflective coatings. The total optics and detector figure of merit, $f_{\rm DO}$ was then computed. The optical prescription and multilayer recipes presented below produced the highest $f_{\rm DO}$. It is important to note that the telescope optimization *must* account for the axion spectrum and detector efficiency and cannot be performed independently. If this process does not include these energy dependent terms, $f_{\rm DO}$ will not achieve the highest possible value.

Telescope prescriptions were generated for designs that had a fixed maximum radius of 300 mm and a minimum radius of 50 mm, with the focal length varied between 4 and 10 m, in increments of 1 m. As the focal length is increased and the graze angle, α, decreases and the number of nested layers increases. For example, the $f = 4$ m design has 110 nested layers, while the $f = 10$ m design has more than 230 layers.

Traditionally, x-ray telescopes have relied on single layer coatings of metals like Au or Ir to achieve high throughput in the 1–10 keV band. More recently, missions designed for hard x-ray observations, like NuSTAR and ASTRO-H, have employed multilayer coatings to achieve high reflectivity up to $\sim$80 keV. We explored combinations of both for IAXO. Although it is theoretically

2014 JINST 9 T05002

possible to optimize the coating for each layer of the telescope, this would impose a high penalty in resources when depositing multilayers on the substrates. Instead, we divided the layers into ten sub-groups, with each sub-group of layers receiving the same multilayer coating. A similar strategy was successfully implemented for NuSTAR [57], and this approach allowed the multilayer deposition tools to be used efficiently.

Material types investigated were single layers of W and W/B_4C multilayers. Other types/combinations to consider are W/Si, Pt/B_4C, Ir/B_4C and Ni/B_4C. W/B_4C and W/Si are well understood coatings for x-ray reflectivity and considerably less expensive to use W than Pt or Ir. Using B_4C instead of Si as the light material will give increasedF reflectivity at 1–4 keV, but also gives slightly higher stress in the coating. Ni/B_4C coatings are not well understood and can give a high interfacial roughness between light and heavy material, but performs similar to W/B_4C and Ir/B_4C at 1–10 keV.

At a given substrate incident angle, α, the coating geometry was optimized by trying every combination in a parameter space of n (number of bilayers), $d_{\rm min}$ (minimum bilayer thickness), $d_{\rm max}$ (maximum bilayer thickness) and Γ , the ratio between the thickness of the heavy material with respect to the total thickness of the bilayer. For every combination, the x-ray reflectivity was calculated using IMD [58]. One of the basic properties of any x-ray telescope is the effective area, EA, the energy-dependent effective aperture of the telescope that accounts for finite reflectivity of individual mirror elements and physical obscuration present in the telescope (e.g., from the support structures used to fabricate the optics and the finite thickness of the substrate which absorbs incoming photons). The effective area of an individual layer i is given by:

$$\mathrm{EA}(E)_i = \mathrm{GA}_i \times R_i(E,\alpha)^2 \times 0.8, \tag{3.1}$$

where GA_i is the projected geometric area of the individual layer i, $R_i(E,\alpha)$ is the reflectivity of the coatings on layer i and the constant factor of 0.8 accounts for obscuration. The total area is given by:

$$\mathrm{EA}(E) = \sum_{i=1}^{N} \mathrm{EA}_i(E), \tag{3.2}$$

where N is the total number of layers. Figure 9 shows the expected behavior of the effective area increasing as the focal length grows. Again, this behavior arises from the fact that longer focal lengths results in shallower incident angles, and reflectivity increases with decreasing graze angles.

The energy-dependent optics throughput or efficiency, $\epsilon_o(E)$, is simply the $\mathrm{EA}(E)$ divided by the geometric area of the entrance pupil:

$$\epsilon_o(E) = \frac{\mathrm{EA}(E)[\mathrm{m}^2]}{\pi(0.3^2 - 0.05^2)[\mathrm{m}^2]}. \tag{3.3}$$

The plot of figure 9 displays this quantity for different focal lengths.

In order to build a meaningful figure or merit we multiply the optics throughput by the energy-dependent axion flux $\frac{d\phi}{dE}$(E) expected from Primakoff production at the Sun [32] and the detector efficiency $\epsilon_d(E)$. The resulting quantity, that we call "detected axion flux" (DAF(E)),

$$\mathrm{DAF}(E) = \sum_{i=1}^{N} \mathrm{EA}_i(E) \times \epsilon_d(E) \times \frac{d\phi}{dE}(E) \tag{3.4}$$

is actually proportional to a hypothetical axion signal in IAXO, and is plotted in figure 10.

2014 JINST 9 T05002

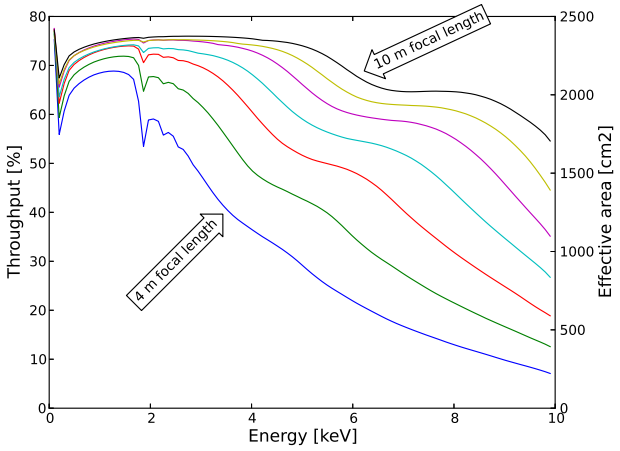

Figure 9. Effective area (right axis) and throughput/efficiency (left axis) versus photon energy for a single telescope for different focal lengths considered, from $f = 4\,\mathrm{m}$ (lowest curve) up to $f = 10\,\mathrm{m}$ (highest curve). Effective area grows as the focal length is increased.

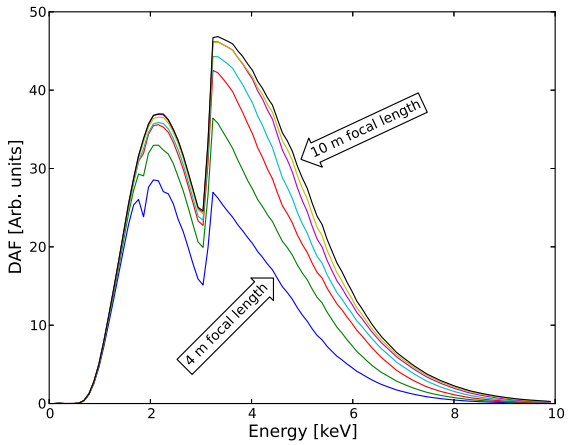

Figure 10. DAF versus photon energy E for a single telescope, and for the different focal lengths considered, from $f = 4\,\mathrm{m}$ (lowest curve) up to $f = 10\,\mathrm{m}$ (highest curve). The significant structure now present is due to absorption edges in detector and coating materials and the shape of the solar axion spectrum.

To find the optimal focal length, we need to maximize the integral of the DAF from 1–10 keV divided by the square root of the spot size (one could see this as the contribution from the optics to the figure of merit f_{DO} as defined in [32]):

$$f_O \equiv \int_{E=1\,\mathrm{keV}}^{10,\mathrm{keV}} \left(\frac{\mathrm{DAF}(E)}{\sqrt{a}} \right) dE. \tag{3.5}$$

2014 JINST 9 T05002

The only quantity left to compute is the spot-size, a. The point-spread-function (PSF) of any x-ray telescope has a complex shape, and the spot-size is computed by first taking the integral of the PSF to compute the encircled energy function (EEF), a measure of how much focused x-ray light is contained within the diameter of a particular size. For example, a common measure of the focusing quality of an x-ray telescope is to determine the 50% value of the EEF, that is to determine the smallest diameter extraction region that contains 50% of the power. This is often referred to as the half-power diameter or HPD.

The spot-size will depend on both the physical size of the object imaged, in this case the 3 arcminute (0.87 mrad) central core of the Sun, and the intrinsic imaging capability of the x-ray optic, i.e. the size of the resultant spot when the telescope images a point-like source. To first order, then, the overall spot size s_{total}, measured in angular extent, will be the root mean square of the object size s_{obj} and the optic quality s_{opt}:

$$s_{\text{total}} = \sqrt{s_{\text{obj}}^2 + s_{\text{opt}}^2}\,. \tag{3.6}$$

Based on the performance of the NuSTAR x-ray telescopes [46], we assume for the nominal design of the telescopes a HPD of 1 arcmin (0.29 mrad) and an 80% EEF of 2 arcmin (0.58 mrad). The angular spot size then becomes:

$$s_{\text{total}} = \sqrt{s_{\text{obj}}^2 + s_{\text{opt}}^2} = \sqrt{0.87^2 + 0.58^2} = 1.0\,\text{mrad}\,. \tag{3.7}$$

As discussed above, the spatial diameter of the spot is simply $f \times s_{\text{total}}$ and the spot area becomes:

$$a = \frac{\pi}{4}\left(s_{\text{total}} \times f\right)^2\,. \tag{3.8}$$

3.4.2 Properties of the IAXO x-ray telescopes

Figure 11 shows $\sqrt{a}$ as well as f_O, as calculated in eq. (3.5), as function of the focal length. The optimal focal length is found to be $f = 5\,\text{m}$. This parameter and the considerations exposed in previous sections fix the design proposed of the IAXO optics. Different engineering drawings of the optics are shown in figure 12 and 13, where the 123 nested layers can be seen. Finally, its main design parameters are listed in table 2.

3.5 Final considerations

Our preliminary scoping study has made simplifying assumptions that will be revisited for the final design study.

- We have assumed the axion spectrum and intensity is uniformly emitted from a region 3 arcmin in extent. We must include the actual distributions in a full Monte Carlo model of the system performance.
- We have computed effective area for an on-axis point source. When the solar extent is included in ray-tracing, the area will decrease by a small amount.
- We have not accounted for non-specular scattering.

2014 JINST 9 T05002

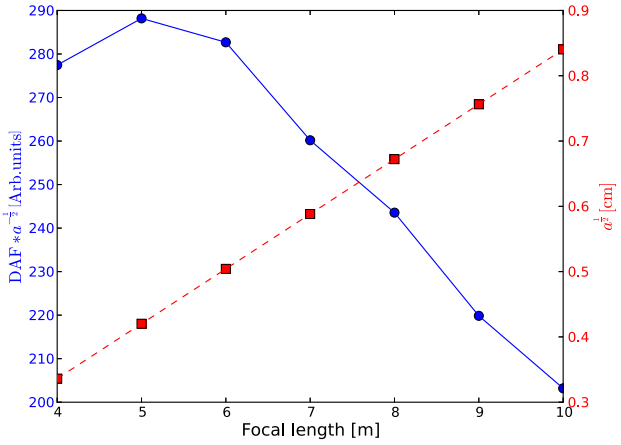

Figure 11. Value of the focal spot size $\sqrt{a}$ (red squares and dashed line, right axis) and the figure of merit f_O (blue circles and solid line, left axis) versus focal length f. The optimal figure of merit is found for $f = 5\,\mathrm{m}$.

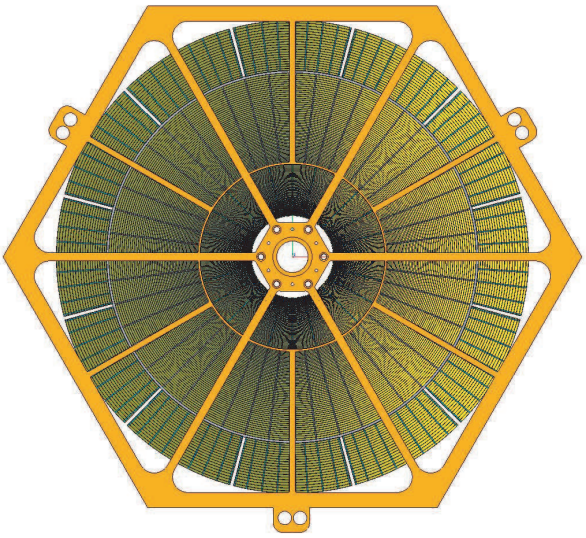

Figure 12. An edge-on view of one IAXO optic, including the hexagonal "spider" structure that will be used to mount the optic into the magnet bores. The thousands of individual mirror segments are visible.

- We have assumed the encircled energy function (EEF) evaluated at 50% (i.e., the half-power-diameter) is 1 arcminute and the EEF evaluated at 80% is 2 arcminute.

- We have only coarsely studied how the focal length f influences the FOM in increments of 1 m.

2014 JINST 9 T05002

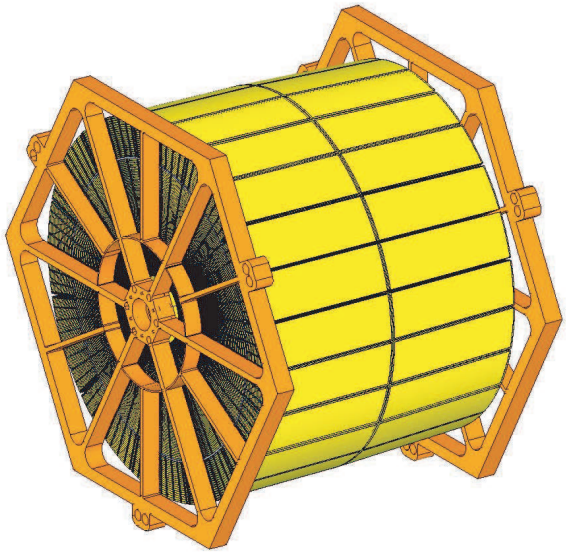

Figure 13. An isomorphic side-view of the telescopes and the spider mounting structures.

Table 2. Main design parameters of the IAXO x-ray telescopes.

Telescopes	8
N, Layers (or shells) per telescope	123
Segments per telescope	2172
Geometric area of glass per telescope	0.38 m^2
Focal length	5.0 m
Inner radius	50 mm
Outer Radius	300 mm
Minimum graze angle	2.63 mrad
Maximum graze angle	15.0 mrad
Coatings	W/B_4C multilayers
Pass band	1–10 keV
IAXO Nominal, 50% EEF (HPD)	0.29 mrad
IAXO Enhanced, 50% EEF (HPD)	0.23 mrad
IAXO Nominal, 80% EEF	0.58 mrad
IAXO Enhanced, 90% EEF	0.58 mrad
FOV	2.9 mrad

2014 JINST 9 T05002

Appendix E

X-ray principles

The development of multilayer mirrors for X-ray focusing requires the ability to measure the properties of the deposited films. A number of techniques can be used, but by far the most practical is X-Ray Reflectometry (XRR) that allows for relatively fast ($\sim$ 20 mins. in our setup) non-destructive measurements and gives information about thicknesses, densities and interlayer imperfections.

E.1 Reflection from a surface

An X-ray photon propagating through one medium and hitting the surface of another medium will interact with the surface by changing direction, either as reflection or refraction. The principle of refraction is explained by *Snell's Law*

$$n_1 \cos\theta_1 = n_2 \cos\theta_2 \tag{E.1}$$

where n_1 and n_2 are the refractive indexes of the first and second medium respectively. θ_1 and θ_2 are the grazing angle of the incident photon and grazing angle of refracted photon respectively.

For an incident plane harmonic wave propagating in the direction $\mathbf{K}$, the electric field can be described as

$$\mathbf{E} = E_0 \mathrm{e}^{i(\mathbf{K}\cdot\mathbf{r}-\omega t)} \tag{E.2}$$

with amplitude E_0. The magnetic field in the plane harmonic wave, $\mathbf{B}$, is perpendicular to the electric field.

There are two polarization modes when considering a plane harmonic wave incident on a surface, either the polarization is Transverse Electric (TE) or Transverse Magnetic (TM).

In the TE mode, the electric field is perpendicular to the plane of incidence, and in the TM mode the magnetic field is perpendicular to the plane of incidence. Any combination of polarization of the two modes can be considered a superposition of the two, so it is enough to look at only the TE and TM modes. And since for small angle grazing incidence X-ray cases the two are nearly identical[80], only the TE mode will be considered from here on.

As the incident wave hits the surface it can either reflect or refract and the electric field of the reflected, E_r, and refracted, E_t, waves are

$$\mathbf{E_r} = E_r e^{i(\mathbf{K}\cdot\mathbf{r}-\omega t)}, \tag{E.3}$$
$$\mathbf{E_t} = E_t e^{i(\mathbf{K}\cdot\mathbf{r}-\omega t)}. \tag{E.4}$$

The relation between reflection, refraction and incident wave is described by the reflectivity amplitude, r, and transmittivity amplitude, t. They are calculated from the electric field amplitudes and their projection parallel to the surface

$$E\sin\theta - E_r\sin\theta = nE_t\sin\theta_t. \tag{E.5}$$

and provide the Fresnel equations

$$r \equiv \frac{E_r}{E} = \frac{\sin\theta - n\sin\theta_t}{\sin\theta + n\sin\theta_t}, \tag{E.6}$$
$$t \equiv \frac{E_t}{E} = \frac{2\sin\theta}{\sin\theta + n\sin\theta_t} \tag{E.7}$$

that describes the reflectivity and transmittivity from an interface between a medium with refractive index of unity (vacuum/air) and another medium with refractive index n.

E.2 Reflection from a thin film

Further evolving the Fresnel equation to describe r and t from an interface between two mediums with refractive indexes n_i and n_j yields

$$r_{ij} \equiv \frac{E_i'}{E_i} = \frac{n_i\sin\theta_i - n_j\sin\theta_j}{n_i\sin\theta_i + n_j\sin\theta_j}, \tag{E.8}$$
$$t_{ij} \equiv \frac{E_t}{E_i} = \frac{2n_i\sin\theta_i}{n_i\sin\theta_i + n_j\sin\theta_j}. \tag{E.9}$$

Here E_i is the electric field amplitude incident on the interface in medium i and E_i' is the reflected electric field amplitude in medium i. E_j is the refracted electric field amplitude in

medium j.

For a thin film on a substrate, there are three mediums: First air (n_0), then film (n_1) and finally substrate (n_s). An incident X-ray photon acting on a thin film have an infinite number of ways to interact with the interfaces. Either the photon is reflected from the first layer, so $r_{01} = 1$, or it is transmitted through the first layer and reflected from the next, or transmitted, then reflected, then reflected and so on. All those possibilities are described by a geometric series

$$r_{\text{thinfilm}} = r_{01} + t_{01}t_{10}r_{1s}\mathrm{e}^{2i\beta_i}\sum_{m=0}^{\infty}(r_{10}r_{12}\mathrm{e}^{2i\beta_i})^m \tag{E.10}$$

where $\mathrm{e}^{2i\beta_i}$ is a phase factor to correct the phase of the waves before being added up and $\beta = 2\pi d_i n_i \sin\theta_i \lambda^{-1}$. Noting that $\sum_{m=0}^{N} k^n = \frac{1-k^n}{1-k}$ becomes $\sum_{m=0}^{\infty} k^n = \frac{1}{1-k}$ for $|k| < 1$, the series can be simplified to

$$r_{\text{thinfilm}} = r_{01} + t_{01}t_{10}r_{1s}\mathrm{e}^{2i\beta_i}\frac{1}{1 - r_{10}r_{12}\mathrm{e}^{2i\beta_i}} \tag{E.11}$$

and finally give

$$r_{\text{thinfilm}} = \frac{r_{01} + r_{12}\mathrm{e}^{2i\beta_i}}{1 - r_{10}r_{12}\mathrm{e}^{2i\beta_i}} \tag{E.12}$$

E.3 Reflection from multilayers

For calculating the reflectivity from a multilayer stack a method such as the Kinematical approximation can be used. But the approximation have the downside of only being able to calculate for multilayers where the bilayer thickness (d-spacing) is constant throughout the multilayer stack.
Since the development of X-ray optics involves making multilayers where the d-spacing change through the stack, it is more appropriate to compute an iterative model using the formula just derived in Eq. (E.12) . The software used in modeling specular reflectivity from a multilayer is IMD[22]. It takes the two formulas

$$r_i = \frac{r_{ij} + r_j\mathrm{e}^{2i\beta_i}}{1 + r_{ij}r_j\mathrm{e}^{2i\beta_i}}, \tag{E.13}$$

$$t_i = \frac{t_{ij}t_j\mathrm{e}^{2i\beta_i}}{1 + r_{ij}r_j\mathrm{e}^{2i\beta_i}} \tag{E.14}$$

$$\tag{E.15}$$

to calculate the i'th layer where r_{ij} is Eq. (E.8) and t_{ij} is Eq. (E.9). Since the j'th layer is the layer below i, the software calculation can start from the bottom layer, the substrate,

where there is no reflectivity from below. From the bottom layer, the software works it way up recursively through each layer, adding up the reflectivity and transmittivity. That is the Paratt recursive method[81].
The energy reflected from or transmitted through the film is denoted as the reflectance R and transmittance T

$$R = |r|^2, \tag{E.16}$$

$$T = \mathrm{Re}\left\{\frac{n_s \sin\theta_s}{n_a \sin\theta_a}\right\}|t|^2. \tag{E.17}$$

The IMD software approximates the absorptance, A, using R and T

$$A = 1 - R - T \tag{E.18}$$

where A is the energy absorbed by the entire film.

E.4 Reflectivity changes due to imperfections in the interface

In experimental cases, the interface between two mediums, or materials, is not completely smooth. The imperfections can be distinguished into two types. Either by atoms in the structure that have been deposited unevenly to create 'hills' and 'valleys' in the surface, which is called pure roughness, σ_p. The other type is diffuse roughness, σ_d, caused by diffusion of atoms from one material into another.
To describe the roughness, the interface can be seen as not an abrupt change of refractive index, but as a profile function, $p(z)$[16], that takes the normalized average value of the dielectric function, $\varepsilon(\mathbf{x})$, in the z direction, where

$$p(z) = \frac{\int\int \varepsilon(\mathbf{x}) dxdy}{(\varepsilon_i - \varepsilon_j)\int\int dxdy}, \tag{E.19}$$

$$\varepsilon(\mathbf{x}) = \begin{cases} \varepsilon_i, & z \to +\infty \\ \varepsilon_j, & z \to -\infty \end{cases}. \tag{E.20}$$

Taking the Fourier transform of $dp/dz = w(z)$ gives $\tilde{w}(s)$, where $s = 4\pi \sin\theta/\lambda$. As Stearn found out, multiplying the Fresnel coeffiecients from Eq. (E.13) with $\tilde{w}(s)$ gives the approximate reflectance including loss from imperfect interfaces. That gives the modified Fresnel coefficients used by IMD:

$$r'_{ij} = r_{ij}\tilde{w}(s). \tag{E.21}$$

The most commonly used interface profile, $p(z)$, is the error function

$$p(z) = \frac{1}{\sqrt{\pi}} \int_{-\infty}^{z} \mathrm{e}^{-t^2/(2\sigma_{rms}^2)} dt \tag{E.22}$$

which after taking the Fourier transform of dp/dz becomes

$$\tilde{w}(s) = \mathrm{e}^{-s^2\sigma_{rms}^2/2}. \tag{E.23}$$

The width of the interface function is denoted by σ_{rms} that is the root mean square of σ_p and σ_d, so

$$\sigma_{rms} = \sqrt{\frac{\sigma_p^2 + \sigma_d^2}{2}}. \tag{E.24}$$

Appendix F

Multilab control software

In the years before moving the DTU Space multilab to DTU campus, it became apparent that a completely new software solution was needed for the coating facility. The software controls all stepper motors (cathode shutters and sample ring), gas flow controllers, cathode power supplies as well as pressure gauge communication.

The original software was made in Visual Basic 6, which Microsoft stopped supporting in 2008. Features that were not build into the software from the start was bolted on at a later stage, resulting in some files with thousands of lines of uncommented code. VB6 also has the drawback that it is single threaded so only one command can be executed at a time, which means that none of the instruments could be read for the log file if e.g. the sample ring was moving. So checking whether there was a plasma dropout on a cathode was not possible while coating a layer, something that can take 30+ minutes.

Everything in the original software solution was controlled in a graphical user interface which made it easy to use, but would only allow for preprogrammed coating types to be made. When it came to make coating investigations for the Athena mission, the linearly graded coatings with top and bilayer required being in front of the computer during the process. For every layer, it was necessary to manually type in a new sample ring speed and start the movement. The coatings took on average 2-3 hours, so it became clear that a new solution was necessary.

F.1 Considerations on the new software solution

Considering the observations from above, a list of requirements for new software was made:

Software should run on Linux To remote control the coating facility in the old software solution, it was necessary to run a remote desktop to control the graphical user interface. The remote desktop requires a relatively large amount of internet bandwidth, something that is not always available. The new software should be controllable over a remote SSH connection using a Bash shell or similar.

Software should log continuously Output from cathode power supplies, pressure gauges and flow meters should be read every 5 seconds during a coating. Between coatings, the pressure gauges should be read every 5 seconds and written to a web server. That allows for checking chamber status on a smart phone or computer connected to the internet.

A coating run should be described in a script Instead of predefined coating types, the scripts make it possible to produce completely custom multilayer coatings.

Software should preferably be open source Open source software is often well documented and flexible. An open source programming language with plenty of extra packages could be Python.

The first attempts at creating new software was directed at Python, since that is just about the most well-documented programming language on the internet, and also where I have the most experience.

It became clear after a while that the real problem was satisfying the second requirement in the list above. All instruments controlled by computer in the multilab are communicated with using serial connections, which will block a line until a command is received by an instrument and a response is returned. In some instruments the response time is up to a second and for the stepper motors, a response is not returned until movement is complete. That is the reason why the old software was unable to read any outputs during the movement of the sample ring.

Python is a single threaded scripting language, so all commands are executed sequentially. There are however software packages for Python that can spawn subprocesses from a queue and read the output of those into another queue. A specific package for multithreading serial communication is Twisted for Python, but after moderately successful attempts it was clear that the solution would be too difficult. The software should be flexible and making a multithreaded python solution with queue systems was both too much work and a bit like reinventing the wheel.

The choice in the end fell on SPEC (by Certified Scientific Software), a software package for X-ray diffraction setups. SPEC is not open source, but requires a license. SPEC is widely used in synchrotron beamlines across the world, and also in the X-ray lab at DTU Space. It is an extremely flexible piece of software, specifically designed to talk to a wide range of instruments at X-ray beamlines. Many types of hardware can be controlled directly from SPEC without the need for drivers, since a direct hardware level communication protocol is build into the software. Commands are typed in on a command line, but can also written into text files (scripts) and the commands can then be executed sequentially by SPEC.

F.2 Software architecture of new Multilab control program

SPEC is, like Python, single threaded. There are however build-in procedures for communicating through the serial protocol and a range of other protocols. SPEC also has the ability to run as a server so commands can be issued to the software using sockets on the system level. By running three separate instances of SPEC at the same time, it became possible to constantly communicate with instruments, write to a logfile, and control the chamber from a main program. The software is set up like the following:

SPEC (main program) The main program, where user-level commands can be typed in. Coating macros are executed from this program. The program has direct control with stepper motors using text-based serial communication[1].

ControlServer The control program. It has direct access to cathode power supplies, gas flow controllers and pressure gauges. SPEC and LogClient will get status and control the instruments through ControlServer by socket commands.

LogClient The logging program. It gets data from the ControlServer every five seconds and writes the data to a file. If a coating is starting, it will make a new folder in the `~/logs` directory named by time and date. In that directory it will make a log file (`logfile.txt`) for the coating and also a log of the commands typed in by a coating macro (`coatinglog.txt`).

These three programs run continuously side-by-side, and will make sure that there are no interruptions in the logging during a coating run. Each command to control any part of the instruments are described in the `site.mac` macro files of each program and auxiliary macro files for e.g. power supplies and pressure gauges. All commands are divided into system-level and user-level commands. System-level commands are called like this:

```
SPEC> output = getpoweroutput(#)
```

This command will get the output of cathode `#` and put the result in the variable `output`. The system-level commands *can* be used by the user, but *should not*. Instead they are used inside user-level command macros, so a user-level command looks like this:

[1] To use SPEC most efficiently, a direct hardware-level communication should be initiated between SPEC and motor controller. However, the motor controller would have to be supported on the hardware-level by SPEC, which is not the case for the current hardware in the Multilab. If a new motor controller is procured, it should be on the list of hardware supported by SPEC. (*http://www.certif.com/hdwdevices.php?family=motor*)

```
SPEC> getpoweroutput 1
Current power output of cathode 1: 450 W
```

This makes it easier to type commands into SPEC, as commands can be autocompleted by using the tabulator key. If a command needs one or several parameters following it and not enough/too many are given, it will respond with an error and a description of the parameters needed.

Log files produced continuously by the LogClient program are fetched by a web server at DTU Space that will make a plot of pressure and cathode power output every 30 seconds. A plot from Sept. 14th 2014 can be seen in figure F.1. The logfile holds up to 50,000 lines of data, which corresponds to ∼3 days of data collected every five seconds. In the plot can be seen both the curve corresponding to the cold cathode pressure gauge (red line) and the baratron pressure gauge (green line). The cold cathode works well at both low and high pressure, but some of the functional parts can be coated over during a coating, so a valve closes off to that gauge during coating. The baratron only works between 10^{-1} Torr and $2 \cdot 10^{-4}$ Torr, but is more precise and also works during a coating.

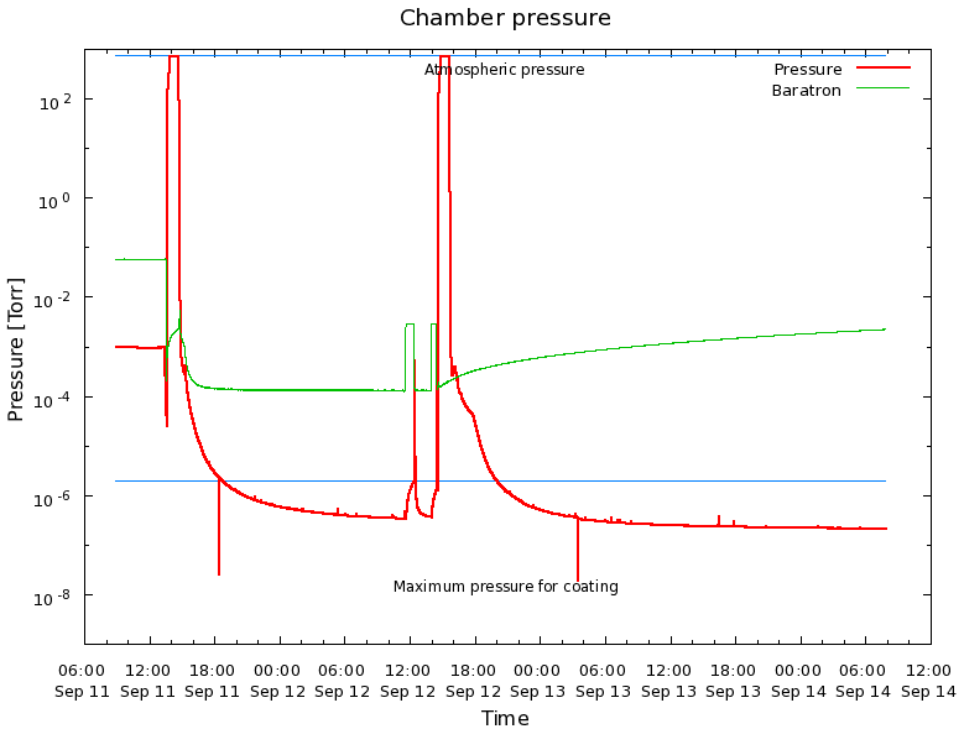

Figure F.1: Plot representing the output from the continuous logging of chamber pressure. Red line is the pressure measured by a combined cold-cathode/penning gauge, that works well under both atmospheric pressure and low pressure. It will not function well during a coating. Green line is the MKS Baratron pressure gauge, that is precise in the $2 \cdot 10^{-4}$ – $5 \cdot 10^{-2}$ Torr range.

The web server that continuously fetches the log file from the coating computer also gets information from the X-ray measurement computer in the basement. Information about measurement status and progress is posted to the same web site. This makes it possible to get the status about all the labs by a quick glance to the web site. The script running on the web server also has the option to send out a mail to pre-defined recipients if the pressure

in the chamber is low enough to start a coating. This proved handy during the NuSTAR coatings, where coatings had to be started in the middle of the night. The web site and script running on the web server were produced during the NuSTAR coating campaign to make the production process easier.

The cathode shutters and ring are all controlled by the same motor controller, and is communicated to over the same serial cable. That is however opaque to the user. In order to open or close a specific shutter, the command `osh #` or `csh #` should be given for opening and closing shutter `#`, respectively. Alternatively, all shutters can be opened or closed using `openallshutters` and `closeallshutters`. The ring can be controlled using the commands `mra speed angle` or `mr speed steps`, the first of which moves the ring at the speed given in steps/sec. at an angle given in degrees. The second does the same thing, except for changing the angle for steps. The motor controller has 668,000 steps in a complete rotation of the ring in the chamber and the speed of the ring should be between 0 and 15,000 steps/sec, otherwise the movement precision decreases. In a coating macro, the command `mra speed angle` is used extensively as the main method to move the samples past the cathodes.

F.2.1 Interfacing with cathode power supplies

The power supplies used to run the cathodes in the multilab consist of two Advanced Energy Pinnacle 5/5 DC power supplies and one Advanced Energy Pinnacle Plus+ 5/5 pulsed-DC power supply. Each power supply has two channels, so can run two cathodes at same time. In order to communicate with power supplies, a special protocol running over serial has to be used. All other instruments in the multilab are communicated with by ControlServer and SPEC using basic text commands send over a serial connection.

The protocol is made for connecting all power supplies to the same serial connection, but in the multilab they are connected separately. The protocol requires each command to be packaged in a binary packet that includes power supply hardware address, length of packet, command, data and finally an XOR of the entire packet so the receiver can verify that the whole packet is there. The design of the packet can be seen in figure F.2. In the header, which is 8 bits long, the first 5 are the address of the power supply (set with a DIP switch on the back) and the remaining 3 bits describe the length of the packet. If the length in the header is set to 7 (111 in binary), the 'optional' byte is used to describe the actual length of the packet. The 'command' byte is a number between 0 and 255 (0 and FFh) in hexadecimal numbers. The 'checksum' byte is an XOR of the entire packet up until the 'chekcksum' byte. When the receiver gets a packet, it will do an XOR of the entire packet including the 'checksum' byte and if the result is 0, the packet is approved and processed.

This packet architecture is used to communicate back and forth between the ControlServer program and the power supplies. If a packet is approved, an ACK is send back in the form of the hex code 06h. The commands for the power supplies can either be to retrieve current status of some parameter, to set a parameter on the power supply, or to execute a command on the power supply. The entire communication protocol is transparent to the user and all

user-level control of the power supplies can be achieved by user-level commands only.

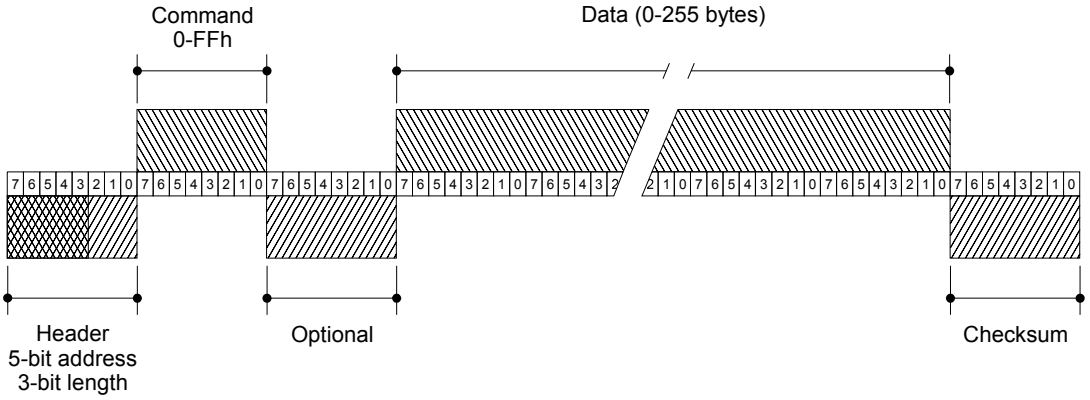

Figure F.2: Schematic of the principle of transmission data packets in the Advanced Energy communication protocol. Each number on the white line corresponds to one bit in the data packet, eight bits equals one byte. From [82]

F.2.2 Coating macro

To produce a coating in the multilab chamber, a coating macro can be typed up and started in the main SPEC program as soon as the pressure is low enough ($\leq 2 \cdot 10^{-6}$ Torr). An example of a simple coating macro, `coat_singlelayer`, can be seen here:

```
def coat_singlelayer '
      if ($# != 1) {
              eprint "Start coating of singlelayer.\n"
              eprint "Usage: coat_singlelayer v(cath3)"
              exit
      }
      coating_start_log
      closevalve
      setflow 1 88
      openflow 1
      openmainflow
      print("Waiting for Ar flow to settle.\n")
      print("(60 seconds).\n")
      sleep(60)
      setpower 3 450
      print("Starting coating.\n")
      mra 90 10000
      sleep(2)
      pson 3
      sleep(5)
      osh 1
      print("Coating material 1, all plates.\n")
      mra -360 $1
      sleep(2)
      csh 1
      sleep(1)
      psoff 3
      mra -90 10000
      sleep(2)
      print("Coating over. Closing flow valve.\n")
      closemainflow
      closeflow 1
      openvalve
      coating_stop_log
      '
```

Each step in the macro is described here:

Error check The macro starts out with an `if` statement to make sure that there is one parameter after the user has called the macro.

coating_start_log Sets the variable `coating_starting=1` in the LogClient program and lets it know that it is time to start a log for a new coating.

closevalve Closes valve to the cold cathode pressure gauge.

setflow 1 88 Sets flow output on flow controller 1 to 88 SCCM.

openflow 1 Opens flow controller 1.

openmainflow Opens flow controllers to chamber.

Text output to user Feedback should be given to user throughout the coating.

sleep(60) Macro will wait for 60 seconds to let the pressure settle at $\sim$2.8 mTorr.

setpower 3 450 Power output is set to 450 W on power supply output 3, the first output on the second power supply.

mra 90 10000 Ring is moved 90º at a speed of 10,000 steps/sec. so the first sample is right before cathode 1.

pson 3 Power supply 3 is turned on.

osh 1 Shutter 1 to cathode 1 is opened.

mra -360 $1 Ring is moved 360º at the speed given by the parameter which is set by the user when calling the macro.

csh 1 Shutter 1 is closed after ring is done moving.

psoff 3 Power supply 3 is turned off.

mra -90 10000 Ring is moved back to start position.

closemainflow Main flow to flow controllers is turned off.

closeflow 1 Flow controller 1 flow is turned off.

openvalve Valve to cold cathode pressure gauge is opened.

coating_stop_log Sets the parameter `coating_starting=0` in the LogClient program, which stops logging for that coating.

The macro will coat all samples in the ring with one layer of the material on cathode 1 at the speed given by the parameter after the macro call. Macros in SPEC are given in a C-type language and many types of loops and statements are implemented. The comprehensive manual for SPEC gives a good overview.

If the user wants to make more complicated multilayers, adjusting the macro example above into a graded-d type coating can of course seem daunting. For that reason, subfunctions are implemented that will coat e.g. 90º of the ring with cathode 3. The principle of the subfunction is as follows:

1. From the start position of the ring where sample 1 is placed, the ring will move sample 1 between cathode 2 and 3.
2. Turn on cathode 3 and open shutter.
3. Move ring 90º given by input parameter.
4. Close shutter 3 and turn off cathode.
5. Move ring back to start position.

The sample can then be coated by another cathode afterwards. If a larger batch requires coating at the same time, there are similar subfunctions for moving 180° and 360°.

The software also makes it possible to coat four different samples with four different coatings in the same coating run. By placing the samples at four different corners of the ring, each sample can have a coating applied separately. Flexible macros for that purpose are not yet implemented, but a template that can be changed into a specific purpose is the macro

```
SPEC> coat_n_bilayers_4plates
```

along with subfunction e.g.

```
SPEC> abilayer_4_plates_c2c4($2,$3,$4,$5,$6,$7,$8,$9)
```

that will coat four different constant-d coatings using cathode 2 and 4. It is possible to change any parameter for the power supplies or flow meters between each sample, so testing out a parameter space becomes significantly faster with this system.

For linearly graded-d coatings, an example is given below that shows the flexibility of the SPEC macro language.

```
for (j=0;j<nlayers;j++){
  printf("\nStarting layer %g.\n",j+1)
  dlayer = dmin+(j)*(dmax-dmin)/(nlayers-1)
  dlayer1 = dlayer*gamma
  dlayer2 = dlayer*(1-gamma)
  speed1 = int(1/((dlayer1-sicorr)/sifact))
  speed2 = int(1/((dlayer2-wcorr)/wfact))
  coat_cath2_180 speed2
  coat_cath4_180 speed1
  }
```

By defining `nlayers` as the number of layers, `dmin`, `dmax` and `gamma` of the coating along with calibration factors, the macro will for every layer calculate the speed for both materials and coat the correct thickness. Calibration factors are calculated as seen in section 2.3 where a for W is `wfact` and b is `wcorr`. The same principle can be used in other types of graded-d coatings, e.g. power-law gradings with a, b and c defined in $d_i = a/(b+i)^c$, where d_i is the d-spacing of the i'th layer.

Bibliography

[1] H. Wolter, *Annalen der Physik* **445**, 94 (1952).

[2] H. Wolter, *Annalen der Physik* **445**, 286 (1952).

[3] N. Lund, *Experimental Astronomy* **2**, 259 (1992).

[4] N. M. Barrière, J. A. Tomsick, S. E. Boggs, *et al.*, *Nuclear Instruments & Methods In Physics Research Section A-Accelerators Spectrometers Detectors And Associated Equipment* **741**, 47 (2014).

[5] N. Barriere, J. Rousselle, P. von Ballmoos, *et al.*, *Journal of Applied Crystallography* **42**, 834 (2009).

[6] J. Koglin, C. Chen, J. Chonko, F. Christensen, et al, *Proceedings of SPIE* (2004).

[7] K. Madsen, F. Christensen, C. Jensen, *Proc. SPIE* (2003).

[8] C. P. Jensen, F. E. Christensen, H. C. Chen, E. B. W. Smitt, E. Ziegler, *International Symposium on Optical Science and Technology* **4496**, 104 (2002).

[9] F. A. Harrison, W. W. Craig, F. E. Christensen, *et al.*, *The Astrophysical Journal* **770**, 103 (2013).

[10] F. A. Harrison, S. Boggs, F. Christensen, *et al.*, *SPIE Astronomical Telescopes and Instrumentation: Observational Frontiers of Astronomy for the New Decade* **7732**, 77320S (2010).

[11] F. A. Harrison, F. E. Christensen, W. Craig, *et al.*, *Experimental Astronomy* **20**, 131 (2005).

[12] F. E. Christensen, A. C. Jakobsen, N. F. Brejnholt, *et al.*, *SPIE Optical Engineering+ Applications* (2011), pp. 81470U–81470U–19.

[13] Brejnholt, N. F., *NuSTAR calibration facility and multilayer reference database* (The Technical University of Denmark, 2012).

[14] J. Als-Nielsen, D. McMorrow, *Elements of modern X-ray physics* (John Wiley & Sons, Ltd, 2001).

[15] K. D. Joensen, P. Voutov, A. Szentgyorgyi, *et al.*, *Applied Optics* **34**, 7935 (1995).

[16] D. G. Stearns, *J. Appl. Phys.; (United States)* **65:2**, 491 (1989).

[17] W. Craig, C. Hailey, M. Jimenez-Garate, *et al.*, *Optics Express* **7**, 178 (2000).

[18] C. J. Hailey, S. Abdali, F. E. Christensen, *et al.*, *Optical Science, Engineering and Instrumentation '97*, O. H. W. Siegmund, M. A. Gummin, eds. (SPIE, 1997), pp. 535–543.

[19] F. Christensen, A. Hornstrup, N. Westergaard, *SPIE Optics & Photonics* (1992).

[20] F. E. Christensen, B. Madsen, A. Hornstrup, *et al.*, *Optical Science, Engineering and Instrumentation '97* **3113**, 294 (1997).

[21] H. W. Schnopper, *SPIE's 1994 International Symposium on Optics, Imaging, and Instrumentation* **2279**, 412 (1994).

[22] D. L. Windt, *Computers in Physics* **12**, 360 (1998).

[23] A. C. Jakobsen, D. D. M. Ferreira, F. E. Christensen, *et al.*, *SPIE Optical Engineering+ Applications* (2011), pp. 81470T–8.

[24] X. Barcons, D. Barret, A. Decourchelle, *et al.*, Athena (Advanced Telescope for High ENergy Astrophysics) Assessment Study Report for ESA Cosmic Vision 2015-2025, *Tech. rep.*, ESA (2012).

[25] R. Willingale, G. Pareschi, F. Christensen, J.-W. d. Herder, *arXiv.org* (2013).

[26] D. Lumb, F. Christensen, C. Jensen, *Optics Communications* (2007).

[27] G. Pareschi, V. Cotroneo, D. Spiga, *et al.*, *Astronomical ...* pp. 481–491 (2004).

[28] X. Barcons, K. Nandra, D. Barret, *et al.*, *Journal of Physics: Conference Series* **610**, 012008 (2015).

[29] D. D. Ferreira, F. E. Christensen, A. C. Jakobsen, N. J. Westergaard, B. Shortt, *SPIE Astronomical Telescopes+ Instrumentation* (International Society for Optics and Photonics, 2012), pp. 84435L–84435L.

[30] M. J. Collon, R. Günther, M. Ackermann, *et al.*, *SPIE Astronomical Telescopes and Instrumentation: Observational Frontiers of Astronomy for the New Decade* **7732**, 77321F (2010).

[31] M. J. Collon, S. Kraft, R. Günther, *et al.*, *Astronomical Telescopes and Instrumentation* **6266**, 626618 (2006).

[32] M. Beijersbergen, S. Kraft, R. Günther, *et al.*, *Astronomical ...* pp. 868–874 (2004).

[33] M. Bjoerck, *Journal of Applied Crystallography* **44**, 1198 (2011).

[34] J. Venables, G. Spiller, M. Hanbucken, *Reports On Progress In Physics* **47**, 399 (1984).

[35] C. V. Thompson, *Annual Review of Materials Science* **30**, 159 (2000).

[36] A. L. Barabasi, H. E. Stanley, Scaling Concepts in Surface Growth (1995).

[37] A. Dirks, H. Leamy, *Thin Solid Films* **47**, 219 (1977).

[38] Y. T. Pei, K. P. Shaha, C. Q. Chen, *et al.*, *Acta Materialia* **57**, 5156 (2009).

[39] K. P. Shaha, Y. T. Pei, C. Q. Chen, J. T. M. De Hosson, *Materials Technology* **26**, 15 (2011).

[40] A. A. Turkin, Y. T. Pei, K. P. Shaha, *et al.*, *Journal of Applied Physics* **108**, (2010).

[41] J. W. Bradley, H. Bäcker, Y. Aranda-Gonzalvo, P. J. Kelly, R. D. Arnell, *Plasma Sources Science & Technology* **11**, 165 (2002).

[42] Y. T. Pei, C. Q. Chen, K. P. Shaha, *et al.*, *Acta Materialia* **56**, 696 (2008).

[43] H. Kiessig, *Annalen der Physik* (1931).

[44] D. L. Windt, *Optical Engineering + Applications* **6688**, 66880R (2007).

[45] A. C. Jakobsen, Developing Supermirror Optics for Hard X-rays: Characterization and Optimizatioon of Thin Film Sputter Deposition, Master's thesis, Københavns Universitet. Niels Bohr Institutet (2010).

[46] G. F. Cardinale, P. B. Mirkarimi, K. F. McCarty, *et al.*, *Thin Solid Films* **253**, 130 (1994).

[47] A. J. Jacobs, , *Published online: 28 December 1963; — doi:10.1038/2001310a0* **200**, 1310 (1963).

[48] A. F. Jankowski, D. M. Makowiecki, *Optical Engineering* **30**, 2003 (1991).

[49] C. Morawe, C. Borel, J. C. Peffen, *Proc of SPIE* (2007).

[50] A. F. Jankowski, L. R. Schrawyer, M. A. Wall, *Journal of Applied Physics* **68**, 5162 (1990).

[51] P. N. Rao, S. K. Rai, M. Nayak, G. S. Lodha, *Applied Optics* **52**, 6126 (2013).

[52] N. Elias, T. Niinikoski, P. Bordalo, Conversion and Operation of CAST as a massive axion detector, Ph.D. thesis, Lisbon, Universidade Técnica de Lisboa, Lisbon (2010).

[53] F. J. Iguaz, *arXiv.org* (2011).

[54] S. Weinberg, *Physical Review Letters* **40**, 223 (1978).

[55] F. Wilczek, *Physical Review Letters* **40**, 279 (1978).

[56] R. D. Peccei, H. R. Quinn, *Physical Review D* **16**, 1791 (1977).

[57] R. D. Peccei, H. R. Quinn, *Physical Review Letters* **38**, 1440 (1977).

[58] H.-Y. Cheng, *Physics Reports* **158**, 1 (1988).

[59] L. Visinelli, Axions in Cold Dark Matter and Inflation Models, Ph.D. thesis, University of Utah, Utah (2011).

[60] K. J. Bae, J.-H. Huh, J. E. Kim, *Journal of Cosmology and Astroparticle Physics* **2008**, 005 (2008).

[61] J. E. Koglin, F. E. Christensen, W. W. Craig, *et al.*, *SPIE Optics & Photonics* **5900** (2005).

[62] W. W. Zhang, *SPIE Optical Engineering + Applications* **7437**, 74370N (2009).

[63] J. Redondo, *arXiv.org* (2013).

[64] E. Armengaud, F. T. Avignone, M. Betz, *et al.*, *Journal of Instrumentation* **9**, T05002 (2014).

[65] K. Zioutas, S. Andriamonje, V. Arsov, *et al.*, *Physical Review Letters* **94**, 121301 (2005).

[66] S. Andriamonje, S. Aune, D. Autiero, *et al.*, *Journal of Cosmology and Astroparticle Physics* **2007**, 010 (2007).

[67] Y. Giomataris, P. Rebourgeard, J. P. Robert, G. Charpak, *Nuclear Instruments & Methods In Physics Research Section A-Accelerators Spectrometers Detectors And Associated Equipment* **376**, 29 (1996).

[68] I. Giomataris, R. De Oliveira, S. Andriamonje, *et al.*, *Nuclear Instruments & Methods In Physics Research Section A-Accelerators Spectrometers Detectors And Associated Equipment* **560**, 405 (2006).

[69] S. Andriamonje, D. Attie, E. Berthoumieux, *et al.*, *Journal of Instrumentation* **5**, P02001 (2010).

[70] P. Sikivie, *Physical Review Letters* **51**, 1415 (1983).

[71] I. G. Irastorza, F. T. Avignone, S. Caspi, *et al.*, *Eur.Phys.J.* p. 013. 37 p (2011).

[72] A. Collaboration, *ATLAS End-Cap Toroids Technical Design Report* (Technical Design Report ATLAS. CERN, 1997).

[73] I. G. Irastorza, The International Axion Observatory IAXO. Letter of Intent to the CERN SPS committee, *Tech. rep.*, CERN (2013).

[74] J. K. Vogel, F. T. Avignone, G. Cantatore, *et al.*, *arXiv.org* (2013).

[75] I. Shilon, A. Dudarev, H. Silva, H. H. J. t. Kate, *arXiv.org* (2012).

[76] I. G. Irastorza, F. T. Avignone, G. Cantatore, *et al.*, *arXiv.org* (2012).

[77] S. Asztalos, E. Daw, H. Peng, *et al.*, *Physical Review D* **64**, 092003 (2001).

[78] M. Fernandez-Perea, M. J. Pivovaroff, R. Soufli, *et al.*, *Nuclear Instruments & Methods In Physics Research Section A-Accelerators Spectrometers Detectors And Associated Equipment* (2012).

[79] M. Fernandez-Perea, M.-A. Descalle, R. Soufli, *et al.*, *Physical Review Letters* **111**, 027404 (2013).

[80] F. L. Pedrotti, L. S. Pedrotti, *Introduction to Optics* (Prentice Hall, 1993).

[81] L. Parratt, C. Hempstead, *Physical Review* **94**, 1593 (1954).

[82] Advanced Energy, *Pinnacle Plus+ 5 kW x 5 kW Power Supply Manual*, 57000095th edn.